

NUMERICAL SIMULATIONS OF WIND TURBINE WAKE INTERACTIONS
USING ACTUATOR LINE AND LES MODELS

A THESIS SUBMITTED TO
THE GRADUATE SCHOOL OF NATURAL AND APPLIED SCIENCES
OF
MIDDLE EAST TECHNICAL UNIVERSITY

BY

HÜSEYİN CAN ÖNEL

IN PARTIAL FULFILLMENT OF THE REQUIREMENTS
FOR
THE DEGREE OF MASTER OF SCIENCE
IN
AEROSPACE ENGINEERING

SEPTEMBER 2019

Approval of the thesis:

**NUMERICAL SIMULATIONS OF WIND TURBINE WAKE
INTERACTIONS USING ACTUATOR LINE AND LES MODELS**

submitted by **HÜSEYİN CAN ÖNEL** in partial fulfillment of the requirements for
the degree of **Master of Science in Aerospace Engineering Department, Middle
East Technical University** by,

Prof. Dr. Halil Kalıpçılar
Dean, Graduate School of **Natural and Applied Sciences**

Prof. Dr. İsmail Hakkı Tuncer
Head of Department, **Aerospace Engineering**

Prof. Dr. İsmail Hakkı Tuncer
Supervisor, **Aerospace Engineering, METU**

Examining Committee Members:

Prof. Dr. Yusuf Özyörük
Aerospace Engineering, METU

Prof. Dr. İsmail Hakkı Tuncer
Aerospace Engineering, METU

Assoc. Prof. Dr. Nilay Sezer Uzol
Aerospace Engineering, METU

Prof. Dr. Hasan Umur Akay
Mechanical Engineering, Atılım University

Assist. Prof. Dr. Özcan Yırtıcı
Computer Engineering, Osmaniye Korkut Ata University

Date: 10.09.2019

I hereby declare that all information in this document has been obtained and presented in accordance with academic rules and ethical conduct. I also declare that, as required by these rules and conduct, I have fully cited and referenced all material and results that are not original to this work.

Name, Surname: Hüseyin Can Önel

Signature :

ABSTRACT

NUMERICAL SIMULATIONS OF WIND TURBINE WAKE INTERACTIONS USING ACTUATOR LINE AND LES MODELS

Önel, Hüseyin Can

M.S., Department of Aerospace Engineering

Supervisor: Prof. Dr. İsmail Hakkı Tuncer

September 2019, 111 pages

Wind is one of the most promising renewable energy resources of the future. After years of optimization studies, Horizontal Axis Wind Turbines shine out as the most efficient type and have been the only model used in large scale commercial wind farms. Layout planning plays an important role in getting the most power out of a wind farm as much as turbine blade design. Most important parameter in this planning phase is the inevitable wake generated by rotors and its impact on other wind turbines which results in power loss. Wake is a highly complex structure whose effects are immensely sensitive to boundary conditions. This situation raises a problem that is difficult to model, especially in wind farms where dozens of turbines are in operation simultaneously. Various analytical and empirical data based simplified wake models have been developed, but they all have a limited use in practical applications. With rapid advancements in computer technologies, Computational Fluid Dynamics offers high fidelity methods for wind turbine and wake simulations. One of these methods is the Actuator Line Model, where turbine blades are represented as distributed volumetric forces without the need of boundary

layer resolution, hence saving some significant computational resource. In this study, accuracy and feasibility of Actuator Line Model in wind energy applications is evaluated. Model's sensitivity to several simulation parameters are assessed and two in-line turbines are simulated using best performing values. OpenFOAM software is used for Actuator Line Model implementation and Navier-Stokes solutions. Results are validated with Blade Element Momentum theory solutions and the model performed well in estimating turbine power production. Turbulent and vortical structures in the wake are best captured with LES turbulence model, velocity deficit curves and field variable plots are presented. Also, the model is capable of handling non-homogeneous conditions under atmospheric boundary layer flow.

Keywords: wind energy, wind farm, wind turbine, wake interactions, actuator line model, incompressible fluid, Navier-Stokes solutions, large eddy simulation, OpenFOAM

ÖZ

RÜZGAR TÜRBİNİ İZBÖLGESİ ETKİLEŞİMLERİNİN AKTÜATÖR ÇİZGİ VE LES MODELLERİ İLE NÜMERİK SİMÜLASYONU

Önel, Hüseyin Can

Yüksek Lisans, Havacılık ve Uzay Mühendisliği Bölümü

Tez Yöneticisi: Prof. Dr. İsmail Hakkı Tuncer

Eylül 2019 , 111 sayfa

Rüzgar, geleceğin en yüksek potansiyele sahip yenilenebilir enerji kaynaklarından biridir. Yıllar içindeki optimizasyon çalışmaları ile Yatay Eksenli Rüzgar Türbinleri en verimli tip olarak öne çıkmıştır ve büyük ölçekli ticari rüzgar tarlalarında kullanılan tek model haline gelmiştir. Rüzgar tarlalarından yüksek verim alınmasında kanat tasarımı kadar türbinlerin yerleşim planlaması da büyük rol oynamaktadır. Bu planlama aşamasında en önemli parametre, türbinlerin kaçınılmaz bir şekilde oluşturduğu izbölgesinin diğer türbinler üzerinde neden olduğu güç kaybıdır. İzbölgesi, oldukça karmaşık ve etkisi sınır şartlarına bağlı olarak büyük farklılıklar gösteren bir yapıdır. Bu durum özellikle onlarca türbin bulunan rüzgar tarlalarında modellenmesi zor bir problem haline gelmektedir. Çeşitli analitik veya deneysel verilere dayalı geliştirilen basitleştirilmiş izbölgesi modelleri mevcuttur ancak isabet oranları kısıtlı kalmıştır. Yakın zamanda bilgisayar teknolojisi ile birlikte gelişen Hesaplamalı Akışkanlar Dinamiği, türbin ve izbölgesi modellemesi için yüksek doğruluklu yöntemler sunmaktadır. Bu yöntemlerden biri, sınır tabakanın çözülmesine gerek kalmadan türbin kanatlarının hacimsel kuvvetler

olarak temsil edildiđi ve hesaplama g¼c¼nden y¼ksek oranda kar sađlayan Akt¼at¼r izgi Modeli'dir. Bu alıřmada, Akt¼at¼r izgi Modeli'nin r¼zgar enerjisi uygulamalarındaki dođruluk oranının ve elveriřliliđinin deđerlendirilmesi amalanmıřtır. Bu dođrultuda modelin eřitli sim¼lasyon parametrelerine olan hassasiyeti incelenmiř ve bulunan en iyi deđerler ile sıralı iki r¼zgar t¼rbininin sim¼lasyonu yapılmıřtır. Akt¼at¼r izgi Modeli aık kaynak kodlu OpenFOAM yazılımına entegre edilmiř ve Navier-Stokes denklemleri burada öz¼lm¼řt¼r. Kanat Elemanı Momentum y¼ntemi ile karřılařtırıldıđında modelin t¼rbın g¼¼retim deđerlerini bařarılı bir řekilde hesapladıđı g¼r¼lm¼řt¼r. İzb¼lgesindeki t¼rb¼lans ve girdap yapıları en iyi LES modeli ile yakalanmıř, hızdaki eksilme eđrileri ve alan deđerifenlerinin grafikleri sunulmuřtur. Ayrıca modelin atmosferik sınır tabaka etkisindeki homojen olmayan akıř řartlarını da yakalayabildiđi g¼sterilmiřtir.

Anahtar Kelimeler: r¼zgar enerjisi, r¼zgar tarlası, r¼zgar t¼rbini, izb¼lgesi etkileřimleri, akt¼at¼r izgi modeli, sıkıřtırılmaz akıřkan, Navier-Stokes öz¼mleri, b¼y¼k evrinti sim¼lasyonu, OpenFOAM

*“The good thing about science is that it’s true
whether or not you believe in it.”*

- Neil deGrasse Tyson

ACKNOWLEDGMENTS

I would first like to thank my thesis advisor Dr. Tuncer for his guidance and support throughout my studies. His expertise and insight have often revealed the things I am doing wrong instantly, which would otherwise take days for me to figure out.

I am grateful to Dr. Pete Bachant and his colleagues for sharing their Actuator Line Model code with the world open-source, and Dr. Bachant personally for answering my novice questions tirelessly.

I would also like to acknowledge Ali Ahmed for his contribution to proofreading and text corrections.

I am so happy for being a part of METU and I would like to thank all my friends and professors in the Aerospace Engineering department. Gathering around a table and having a chat with even the most veteran professors in all their humbleness is not something one can get in most of the universities.

I couldn't be where I am now if it was not for my dear mother and my family's support and faith in me, even in the most difficult times of my life. Thanks for everything.

Finally, I would like to express my deepest gratitude to my lovely girlfriend. Your compassion and sympathy were invaluable to keep me going. Your little notes that made me smile are still commented out and hidden in my codes and even in this document. I appreciate everything you've done for me, with me.

TABLE OF CONTENTS

ABSTRACT	v
ÖZ	vii
ACKNOWLEDGMENTS	x
TABLE OF CONTENTS	xi
LIST OF TABLES	xiv
LIST OF FIGURES	xv
LIST OF ABBREVIATIONS	xxii
LIST OF SYMBOLS	xxiii
CHAPTERS	
1 INTRODUCTION	1
1.1 Typical Wind Farm Design Process	2
1.2 Wake Modeling in Wind Farms	4
1.3 Review of Numerical Techniques used for Rotor and Wake Modeling	6
1.3.1 Actuator Disk Model (ADM)	8
1.3.2 Actuator Line Model (ALM)	12
1.4 Objectives	26
2 METHODOLOGY	29

2.1	Basics of Wind Power	29
2.1.1	Generalized Momentum Theory	31
2.2	Blade Element-Momentum Theory (BEM)	33
2.3	2D Airfoil Calculations: XFOIL	35
2.4	Tip Loss Correction	36
2.5	Flow Solutions with OpenFOAM	37
2.5.1	Large Eddy Simulation (LES) Equations	39
2.5.2	Flow Solver: pimpleFoam	41
2.6	Actuator Line Model (ALM)	42
2.6.1	Velocity Sampling	44
2.6.2	Force Projection	46
2.6.3	ALM Implementation in OpenFOAM: turbinesFoam	48
2.7	Computational Grid	49
3	RESULTS AND DISCUSSION	53
3.1	Assessment of Simulation Parameters on a Single Isolated Turbine	54
3.1.1	Iterative Solution for Force-Velocity Coupling	55
3.1.2	Temporal Discretization	57
3.1.3	Spatial Discretization	60
3.1.4	Force Projection Width and Gaussian ϵ	63
3.1.5	Number of Actuator Points	71
3.1.6	Results with Various Rotational Speeds	71
3.1.7	Summary	73
3.2	Wake Interaction Simulations of Two Wind Turbines in Tandem	76

3.2.1	Uniform Inflow Acting on Two Isolated In-line Wind Turbines	76
3.2.2	Sheared Inflow Acting on Two In-line Wind Turbines on Flat Terrain	81
3.2.3	Sheared Inflow Acting on Two In-line Wind Turbines on Flat Terrain with Upstream Turbine Yawed	87
3.2.4	Assesment of ABL and Yaw Effects	91
3.3	Computational Cost and Parallelization	97
4	CONCLUSIONS	101
	REFERENCES	103

LIST OF TABLES

TABLES

Table 1.1	Order of length and time scales in numerical solutions of a typical wind farm	8
Table 2.1	Boundary conditions in the isolated turbine case (ZG: zero gradient, Calc.: calculated, ABL: atmospheric boundary layer)	51
Table 2.2	Boundary conditions in the sheared flow case	51
Table 3.1	Individual and total power output of various dual rotor configurations.	93
Table 3.2	Solution time of simulations with different $CF L_{tip}$ values.	97
Table 3.3	Solution time of simulations with different grid sizes.	98

LIST OF FIGURES

FIGURES

Figure 1.1	Wake interactions in Horns Rev Offshore Wind Farm, Denmark. (Photo by Christian Steiness / Vattenfall)	4
Figure 1.2	Thrust force distributions along the actuator disc tested by Simisiroglou et al. [1].	12
Figure 1.3	Division of blades into actuator points in ALM and ADM (Source: [2]).	13
Figure 1.4	Troldborg's wake results with (top) and without (bottom) atmospheric turbulence shows its impact on the ALM solutions [3]. . . .	23
Figure 2.1	Flow through a porous disk in 1D momentum theory. (Source: [4]).	30
Figure 2.2	Relation of C_p with axial induction factor in no rotation case (a) and with TSR in case with wake rotation (b).	32
Figure 2.3	Differential annular element used in BEM calculations (Source: [5]).	33
Figure 2.4	Solution loop of BEM as a combination of Momentum and Blade Element Theories (Source: [6])	34
Figure 2.5	A sample XFOIL solution of NACA64-618 airfoil at $Re=5M$. . .	35
Figure 2.6	Tip loss factor in accordance with empirical data (Source: [7]) . .	37
Figure 2.7	An example of calculated tip loss factor distribution in simulations.	38

Figure 2.8	Flow chart showing the PIMPLE loop within a single time step	42
Figure 2.9	Relative velocity, angle definitions and forces acting on a blade section in BEM and ALM approaches. (Original image: [8])	43
Figure 2.10	Various velocity sampling techniques: upstream monitoring (+), line averaging (x) and monitoring on the actuator point (o)	45
Figure 2.11	Projection of computed force to cells in vicinity, as a function of distance. (Source: [9])	46
Figure 2.12	Resemblance of pressure field past an airfoil via distributed point force (Source: [10])	47
Figure 2.13	Comparison of various ϵ parameters in Gaussian function.	48
Figure 2.14	Discretized solution domain for an isolated rotor simulation. Resolution at rotor plane is $\Delta_g/R = 1/32$	50
Figure 2.15	Mid-y-plane sliced view of the mesh used in ABL flow simulations.	50
Figure 3.1	Sections of the NREL 5MW wind turbine.	54
Figure 3.2	Convergence of angle of attack distribution along blade span with PIMPLE iterations (FRM: [11])	55
Figure 3.3	Convergence of relative velocity magnitude distribution along blade span with PIMPLE iterations	56
Figure 3.4	Visualization of an Actuator Line that is divided into 19 actuator points on a $\Delta_g/R = 1/32$ solution grid.	57
Figure 3.5	Change of predicted C_P with CFL_{tip} for different Gaussian ϵ values ($\Delta_g/R = 1/32$)	58
Figure 3.6	Computed Angle of Attack and Tangential Force distributions for different CFL_{tip} values ($\epsilon = 2\Delta_g$) (FRM: [11])	59

Figure 3.7	U_x profile along z-axis passing through rotation axis at $3D$ downstream for different CFL_{tip} values.	60
Figure 3.8	Convergence of computed Power Coefficient with various grid resolutions for different grid size independent constant ϵ values	61
Figure 3.9	Computed Angle of Attack distribution for different constant ϵ values	61
Figure 3.10	Computed Tangential Force distribution for different constant ϵ values	62
Figure 3.11	Convergence of computed C_P with various grid resolutions for different chord size based ϵ values	62
Figure 3.12	Convergence of computed C_P with various grid resolutions for different cell size based ϵ values	63
Figure 3.13	Force vector field with different magnitudes of chord and cell size based ϵ (at $\Delta_g/R = 1/64$).	64
Figure 3.14	Computed α for different chord based ϵ values (at $\Delta_g/R = 1/16$) (FRM: [11])	65
Figure 3.15	Computed F_t for different chord based ϵ values (at $\Delta_g/R = 1/16$) (FRM: [11])	65
Figure 3.16	Computed α for different chord based ϵ values (at $\Delta_g/R = 1/32$) (FRM: [11])	66
Figure 3.17	Computed F_t for different chord based ϵ values (at $\Delta_g/R = 1/32$) (FRM: [11])	66
Figure 3.18	Computed α for different chord based ϵ values (at $\Delta_g/R = 1/64$) (FRM: [11])	67
Figure 3.19	Computed α for different chord based ϵ values (at $\Delta_g/R = 1/64$) (FRM: [11])	67

Figure 3.20	Computed α for different cell size based ϵ values (at $\Delta_g/R = 1/16$) (FRM: [11])	68
Figure 3.21	Computed α and F_t for different cell size based ϵ values (at $\Delta_g/R = 1/16$) (FRM: [11])	68
Figure 3.22	Computed α for different cell size based ϵ values (at $\Delta_g/R = 1/32$) (FRM: [11])	68
Figure 3.23	Computed α and F_t for different cell size based ϵ values (at $\Delta_g/R = 1/32$) (FRM: [11])	69
Figure 3.24	Computed α for different cell size based ϵ values (at $\Delta_g/R = 1/64$) (FRM: [11])	69
Figure 3.25	Computed α and F_t for different cell size based ϵ values (at $\Delta_g/R = 1/64$) (FRM: [11])	69
Figure 3.26	Convergence of computed C_P with chord based ϵ values for different grid resolutions	70
Figure 3.27	Convergence of computed C_P with cell size based ϵ values for different grid resolutions	70
Figure 3.28	Computed α for different number of actuator points (FRM: [11])	71
Figure 3.29	Computed F_t for different number of actuator points (FRM: [11])	71
Figure 3.30	Computed power and thrust coefficients for different tip speed ratios at $U_{ref} = 11.4m/s$ (RANS-BEM: [12])	72
Figure 3.31	Computed α and F_t distributions for different TSR values (at $U_{ref} = 11.4m/s$, $\Delta_g/R = 1/32$). Horizontal axes represents radial position on the blade in meters.	74
Figure 3.32	C_P error history of simulations with different TSR (smoothened out via moving average)	75
Figure 3.33	C_P convergence history of simulations for different TSR	75

Figure 3.34	Velocity and vorticity magnitude contours during wake development (uniform inflow, mid-z-plane section)	77
Figure 3.35	Vorticity $\zeta = 0.38$ iso-surfaces (uniform inflow case, $\Delta_g/R = 1/32$)	78
Figure 3.36	Q-criterion $Q = 0.005$ iso-surfaces (uniform inflow case, $\Delta_g/R = 1/32$)	78
Figure 3.37	Instantaneous velocity magnitude contours on different grid resolutions (uniform flow, mid-z-plane section)	79
Figure 3.38	Instantaneous vorticity magnitude contours on different grid resolutions (uniform flow, mid-z-plane section)	79
Figure 3.39	Mean axial velocity deficit $(1 - U_x/U_{ref})$ profiles along y (horizontal) axis at different x stations (isolated rotors case). (— $\Delta_g/R = 1/16$) (— $\Delta_g/R = 1/32$).	80
Figure 3.40	Computed α and F_t for different grid resolutions (isolated dual turbines case, averaged over last 5 revolutions).	81
Figure 3.41	Velocity and vorticity magnitude contours during wake development (ABL inflow, mid-z-plane section)	83
Figure 3.42	Mean axial velocity deficit $(1 - U_x/U_{ref})$ profiles along y (horizontal) axis at different x stations (ABL flow case).	84
Figure 3.43	Velocity and vorticity magnitude contours during wake development (ABL inflow, mid-y-plane section)	85
Figure 3.44	Mean axial velocity deficit $(1 - U_x/U_{ref})$ profiles along z (vertical) axis at different x stations (ABL flow case).	85
Figure 3.45	Vorticity $\zeta = 0.38$ iso-surfaces (ABL inflow case)	86
Figure 3.46	Q-criterion $Q = 0.005$ iso-surfaces (ABL inflow case)	86

Figure 3.47	Velocity and vorticity magnitude contours during wake development (ABL inflow, mid-z-plane section)	88
Figure 3.48	Mean axial velocity deficit $(1 - U_x/U_{ref})$ profiles along y (horizontal) axis at different x stations (ABL flow case with WT1 yawed).	89
Figure 3.49	Velocity and vorticity magnitude contours during wake development (ABL inflow, mid-y-plane section)	89
Figure 3.50	Mean axial velocity deficit $(1 - U_x/U_{ref})$ profiles along z (vertical) axis at different x stations (ABL flow case with WT1 yawed).	90
Figure 3.51	Vorticity $\zeta = 0.38$ iso-surfaces (ABL inflow case with WT1 yawed)	90
Figure 3.52	Q-criterion $Q = 0.005$ iso-surfaces (ABL inflow case with WT1 yawed)	90
Figure 3.53	C_P convergence in different dual turbine conditions.	91
Figure 3.54	C_P convergence history of dual wind turbine simulations (smoothened out via moving average).	92
Figure 3.55	Vorticity contours at various x-stations in different dual turbine cases.	93
Figure 3.56	Cyclic histogram of Blade 1's power contribution to WT1 (data is collected over last 5 revolutions).	94
Figure 3.57	Cyclic histogram of Blade 1's power contribution to WT2 (data is collected over last 5 revolutions).	94
Figure 3.58	Cyclic histogram of WT1's power production (data is collected over last 5 revolutions).	95
Figure 3.59	Cyclic histogram of WT2's power production (data is collected over last 5 revolutions).	95

Figure 3.60	Computed α distribution for different dual turbine cases (averaged over last 5 revolutions).	96
Figure 3.61	Computed F_t distribution for different dual turbine cases (averaged over last 5 revolutions).	97
Figure 3.62	5 of the cell blocks assigned to their respective processor cores in the decomposed domain. Numbers denote the cell count per block. . .	98
Figure 3.63	Parallelization speed-up vs. number of cores for single and dual wind turbine simulations. (Single WT: 821K cells, Dual WT: 4.7M cells)	99

LIST OF ABBREVIATIONS

ABL	Atmospheric Boundary Layer
ADM	Actuator Disk Model
ALM	Actuator Line Model
FRM	Fully Resolved Mesh
HAWT	Horizontal Axis Wind Turbine
LES	Large Eddy Simulation
NREL	National Renewable Energy Laboratory
RANS	Reynolds-Averaged Navier-Stokes
TSR	Tip Speed Ratio
VAWT	Vertical Axis Wind Turbine
WRF	The Weather Research and Forecasting Model

LIST OF SYMBOLS

a	Axial induction factor
a', a_t	Tangential induction factor
α	Angle of attack
c	Chord length
C_a	2D (sectional) axial force coefficient
C_d	2D (sectional) drag coefficient
C_D	3D drag coefficient
C_l	2D (sectional) lift coefficient
C_L	3D lift coefficient
C_P	Turbine power coefficient
C_T	Turbine thrust coefficient
C_t	2D (sectional) tangential force coefficient
D	3D drag
D'	2D (sectional) drag (force per length)
Δ_g	Grid cell size
Δ_{AP}	Actuator point spacing
ϵ	Gaussian kernel (projection width control parameter)
ε	Rate of dissipation of turbulent kinetic energy
F'_a	2D (sectional) axial force (force per length)
F'_t	2D (sectional) tangential force (force per length)
k	Turbulent kinetic energy
L	3D lift
L'	2D (sectional) lift (force per length)

λ	Tip speed ratio
λ_r	Local speed ratio
N_B	Number of blades
N_{AP}	Number of actuator points
Ω	Rotor angular velocity
ω	Angular velocity conveyed to wake
ϕ	Inflow angle (angle between rotor plane and relative velocity)
P	Turbine power
Q	Turbine torque
r	Local radial position
R	Rotor radius
ρ	Free stream density
T	Turbine thrust
U	Velocity

CHAPTER 1

INTRODUCTION

Ever-growing human population and technological progress has resulted in a great demand for energy and efficient power production. A 48% increase in energy demand is predicted between 2012 and 2040 by the U.S. Energy Information Administration (EIA) [13]. Fossil fuels have dominated the energy industry as the main resource since the development of coal and beginning of industrialization in mid 19th century. Renewable energy was used to be referred as an "alternative resource" to fossil fuels since then, but recent data shows that this situation is likely to change soon. As of July 2018, it is reported that the share of installed capacity of renewable energy sources grew from 8.6% in 2010 to 18.2%, while wind power being in the forefront with 44.2% share of global renewable power capacity, followed by solar energy (32.4%) [14]. Other studies forecast that it will be cheaper to build renewable energy plants than fossil fuel facilities by 2020 [15], hence it is obvious that harvesting power from wind with maximum efficiency will be one of the main concerns of engineers and investors in the near future. Although wind farms has zero fuel and minimal operational costs compared to conventional power plants, installation costs are very high. Average life expectancy of a wind turbine is 20 years and a study by NREL in 2015 showed that average wind farm installation cost is \$1,690,000 per MW [16]. Such long lifetimes and high costs push designers to constantly improve their modeling techniques to make better design decisions and power production estimations.

Wind turbine is a device which extracts kinetic energy in the wind and converts it into mechanical and usable electrical energy, respectively. Although many types of wind turbines have been developed in history, they can be categorized into two types

in a broad sense: horizontal and vertical axis wind turbines (HAWT and VAWT, respectively). HAWTs are used primarily in almost all of the large scale wind farms today. They are lift-driven devices, i.e. resultant torque is acquired solely by the lift force generated over blades, in contrary to a drag-driven device (like a Savonius-type VAWT). Studies show that a turbine's efficiency increase with its tip speed and total surface area of wind flow it can enclose (stream tube section). Since HAWTs are suitable to be designed according to these needs with less structural concern and have higher efficiency more than any other type of wind turbine, they have become the most successful and commercialized in recent years. Hence, HAWT is the first choice of turbine type to study and it is therefore chosen as the model turbine in this thesis.

1.1 Typical Wind Farm Design Process

From an engineering standpoint, getting the most out of wind flow is a multi-objective optimization problem; mainly structural, electromechanics and aerodynamics. The turbine must respond quickly to changing wind speed and direction, stop or stall if necessary and endure ever-changing harsh atmospheric conditions. For instance, studies show that wake behind the wind turbine, which is in the scope of aerodynamics, has a very strong impact on fatigue of the wind turbine, which is in the scope of structural engineering [17]. Similarly, erosion over the leading edge of the blades due to dust and debris in the wind is found to cause a significant decrease in aerodynamic performance [18]. Variations in blades' aerodynamic characteristics due to loadings is yet another concern and it is in the unique area of aero-elasticity which is a multi-disciplinary area on its own [19]. Hence, handling these problems with complete independence means missing much of the big picture, yet it is the most practical way due to complexity of the whole system.

A wind farm's lifetime profitability is profoundly affected by its initial design. In most cases, a site is decided on to start with and makes up the first design constraint: i.e. site boundary. Key point here is to determine the location of installation site in a large geographical scale. Windrose plots and wind energy potential atlases obtained from field measurements are mainly used to get an idea of wind strength, consistency, dominant wind direction and overall energy potential. This stage is often called

macro-siting. Ultimate aim from this point on is to maximize the plant's power output while staying within the constraints with minimal initial investment and operating costs. Some additional key constraints on development to be defined are:

- Maximum installed capacity
- Environmental concerns (i.e. noise and visual)
- Minimum turbine spacing (defined by turbine manufacturer)

After a rough estimate of the installed capacity is made, a preliminary wind farm layout can be produced. Usually, a range of turbine size and hub height values are chosen and several layout scenarios are considered based on each specific turbine. This stage where each turbine's location is determined is called *micro-siting* and mainly driven by the concern of eliminating wake imposed on turbines, as much as possible. Tighter spacing between turbines increase wake losses whereas larger distances cause inefficient use of land. This optimization problem of turbine positioning for maximum energy output remains to be one of the most complex problems for the aerodynamics engineer along with turbine design. Although economics is usually the tighter constraint here, even a minimal gain in energy production is worthwhile since it is known that wake losses have a significant effect in wind farms up to 20% of total output [20]. Wake has such a strong influence on power loss, many researchers suggest methods where upstream wind turbines are curtailed on purpose with the aim of reducing wake losses suffered by downstream turbines and increasing overall power output. Wessel [21] tried curtailing the upwind turbines intentionally and obtained a 1.77% increase in annual production. Another approach to wake mitigation is positioning the rotor in yawed or tilted angles. Gebraad et al. [22] developed an algorithm to optimize a wind farm's production by yawing rotors and they obtained gains up to 13%. In his Master's thesis, Storm [23] optimized both yaw and tilt angles of wind turbines and achieved a 12.1% increase in production. Apart from the wake effects; blockage by structures, surface roughness, thermal effects and overall topography causes additional turbulence and its influence on turbine loadings should also be mitigated in this design process.

All in all, it can be seen that the design process of a complete wind farm, from rotor



Figure 1.1: Wake interactions in Horns Rev Offshore Wind Farm, Denmark.

(Photo by Christian Steiness / Vattenfall)

design to layout planning, starts with and influenced primarily by aerodynamics of the problem. In this study, aerodynamics of the wind farm design is approached with a focus on two main elements:

- *Rotor Modeling (for turbine design)*: Aerodynamic design of the wind turbine itself, optimization of blade geometry for maximum torque. Mostly, the rotor is developed for idealized operating conditions, i.e. non-sheared, uniform, steady, axial inflow and absence of wake caused by other turbines.
- *Wake Modeling (for layout design)*: Development of methods to simulate wake behind rotors to capture velocity deficit and turbulent structures which are necessary for layout optimization and plan the layout such that wake loss is minimized.

1.2 Wake Modeling in Wind Farms

Energy of air flow passing the rotor is partially extracted by the wind turbine and this causes a momentum loss due to deceleration in flow velocity and increase in turbulent energy behind the turbine. This region is called *wake* and it is one of the key parameters in wind farm design. Wake region expands due to diffusion of the

momentum loss as downstream flow moves away from the rotor and velocity deficit is recovered eventually. Primary parameters that affect the recovery distance other than turbine characteristics are atmospheric turbulence, terrain roughness, obstructions and wind shear. There are three main quantities which characterize the wake:

- *Non-dimensional velocity deficit*: Measures how much of the velocity is lost at a downstream point proportional to free stream. It is defined as $1 - (U/U_\infty)$.
- *Turbulence intensity*: Defined as ratio of velocity fluctuation to mean velocity. Defined as u'/U .
- *Expansion function*: Defines width of the wake at a point as a function of downstream distance. Mostly used in analytical models.

Wake is often examined in two regions where it has distinct characteristics; far and near wake [24]. Near wake is roughly defined as the region where effect of rotor is felt directly in the velocity profile. In most cases, maximum velocity deficit occurs within this region (after 1-2 rotor diameters according to Ainslie [25]) and high shear layer slope is observed. This length can be longer for low ambient turbulence. The point where shear layer reaches the rotor axis can be defined where near wake region ends. After this point, rotor shape has little to no impact on the wake structure and velocity profile has a self-similar distribution. This region is recognized as the far wake. Study of turbines which fall into the far wake of upstream rotors in wind farms is the most important aspect in layout optimization.

Experimental methods have been and still are used primarily for turbine design, as they have been for almost every aerodynamic problem historically. Countless numbers of experiments on single wind turbine performance has been done. Although downscaling is a manageable problem for a single or few number of wind turbines in a wind tunnel, when it comes to simulating a complete wind farm on a terrain for layout design and optimization studies, additional complications arise. Simulating the atmospheric boundary layer and resembling surface roughness and terrain shape induced turbulence can be counted as some of them. Using a scaled down wind turbine model with blades and other components has its own difficulties. Hence, using porous disks in substitution and producing wake similar to the actual

rotor is a common solution, despite the loss in accuracy. On this note, Cheng et al. [26] used a terrain model in an atmospheric boundary layer wind tunnel to survey local wind condition variations over a wind farm but no turbines were introduced on the model hence wake effect was absent. Bastankhah and Porte-Agel [27] have developed and fully characterized a 15cm diameter miniature HAWT for such purposes in their recent study. Numerical methods on the other hand, comes in as a favorable alternative since scale of the problem is only limited by the computational capacity.

1.3 Review of Numerical Techniques used for Rotor and Wake Modeling

Many methods with various levels of trade-off between accuracy and computational cost have been developed for both rotor and layout modeling. Complexity of these models range from simplified approximations available in analytical or linearized forms to solutions of full set of Navier-Stokes equations.

Even before the numerical solution of full 3D Navier-Stokes equations were conceivable, flow field inside a wake region was an area that researchers were studying on. Simplified solutions of mass and/or momentum conservation equations have underlied the models developed in this era, yet they still needed to be corrected by empirical data. Some renowned models are still used in wind farm modeling today, among which Jensen [28] [29], Ishihara [30] [31], and Frandsen [32] models are the few worth mentioning. In comparison of these models for their accuracy, Charhouni et al. [33] concluded that none of them was able to calculate velocity deficit approximately except Jensen's model, nevertheless they emphasized the discussion of uncertainty of all models.

In some related studies, centerline velocity deficit is determined by turbine's power curve, self-similar profiles are assumed in the far wake region and weighted formulas are developed for estimation of onset velocities at the rotors [34] [35]. Taylor [36] used linearized boundary layer approximations, experimented with surface roughness and wind speed and direction, compared his results to wind tunnel experiments and found useful estimates of power loss at downstream turbines. A similar methodology

was employed by Crespo et al. [37] in 1985 where they have presented parameters to describe wake evolution as functions of turbine and atmospheric characteristics. Sforza et al. [38] solved simplified axisymmetric Navier-Stokes equations to estimate the wake behind a porous disk to resemble the wind turbine effect.

The simplest approach to rotor modeling can be referred back to Froude's 1D momentum theory [39] applied to a homogeneous disc with zero thickness for inviscid, incompressible fluid in a steady, axial and irrotational flow. Using Froude's theory, German scientist Betz [40] has related axial induction factor to power coefficient and concluded in 1920 that a device can not extract more than $16/27$ th ($\approx 59.3\%$) of the energy available in continuous fluid flow. This theoretical model has been extended by many researchers in the following years and applied to wind turbines and other similar rotor devices (i.e. helicopters). Most notably, rotation was added to the wake and disk was divided into rotating differential annular elements for a better rotor resemblance (commonly known as the Rotor Disk Model or the Generalized Momentum Theory). This has introduced tangential induction factor and showed that maximum power coefficient C_P is not only a function of freestream velocity but also the angular velocity. Finally, this annularly constant disk was discretized into actual number of blades and blade geometry was taken into account via 2D calculations of local lift and drag. Details of this model was proposed by Glauert in 1935 [41] and remained one of the most extensively used models in rotor design to this day under the name of Blade Element-Momentum (BEM) theory.

Free-vortex wake models have also been used as a relatively low-cost approach in wake modeling of rotors. Yemenici et al. [42] have investigated the wake interactions between two helicopter rotors using free-vortex wake methodology and managed to capture force variations induced to the downstream rotor by generating the asymmetric wake region.

As CFD went mainstream with advancements in computational technologies during early 1960s, its use in numerical simulations of wind turbines and farms became growingly popular. Since wind turbines are rotary devices, CFD simulations are carried out with special treatments. Sliding Mesh Interface (SMI) and Multiple Reference Frame (MRF) are two popular methodologies used for simulating

rotating geometries. In MRF, rotation is reproduced by adding necessary terms into momentum equation to take centrifugal and Coriolis effects into account and it is suitable for steady-state simulations [43]. SMI on the other hand is more complex to implement but it can handle unsteady simulations by moving and deforming the grid, at the expense of computational cost [44] [45].

Table 1.1: *Order of length and time scales in numerical solutions of a typical wind farm*

	Length scale, m	Velocity scale, m/s	Time scale, s
Blade Boundary Layer	10^{-3}	10^2	10^{-5}
Rotor	10^2	10^1	10^1
Wind Farm Site	10^4	10^1	10^3

Length and time scales of the problem has a big effect on discretization and solution time of Navier-Stokes equations since grid and time step sizes are dictated by them. Both SMI and MRF methods require the blade geometry in solution grid and boundary layer fully resolved. This requires a large number of cells even for a single turbine, which poses a scalability problem for wind farms where numerous turbines exist. Numerical solution of a full scale wind farm involves a wide range of length and time scales (Table 1.1) and resolving all of them is a computationally demanding task. This situation originates the need for inexpensive yet high fidelity simplified models that are suitable for practical applications. Actuator models have been developed to serve this purpose among which Actuator Disk (ADM) and Actuator Line (ALM) Models became prominent in simulating wake in wind farms and are employed in many studies. Both methods provide considerable advantage by avoiding the necessity of resolving the blade boundary layer.

1.3.1 Actuator Disk Model (ADM)

Actuator Disk Model (ADM) is the simplest rotor modeling technique in CFD applications. The blade swept area forms a full disc, which represents the rotor. This method can be divided into two groups:

1. *Standard ADM*: In standard ADM, rotation of the rotor is not modeled and only forces in the axial direction are accounted for. Since no tangential forces that generate

the torque (and rotation) are present in this model, only the thrust force exists. This leads to the simple calculation of thrust force by means of the thrust coefficient, C_T .

The only parameter comes from the flow solution here is the reference velocity U_{ref} . The monitoring point for U_{ref} is often chosen as an upstream location of the rotor, where the flow can be considered as free stream. Averaging velocities throughout the disc is another approach in U_{ref} calculation. No blade details, such as airfoil profiles, twist etc. are required. The required thrust coefficient data are not calculated during the simulation but rather must be known and provided beforehand as a function of free stream velocity. This necessity can be considered as one of the drawbacks of the standard ADM. Since the resultant force is the integral force exerted by the whole rotor on the fluid, it is distributed throughout the cell centers which falls in the actuator disc area. This distribution is often fully homogeneous, i.e. not a function of radial or azimuthal position. One big advantage of the Standard ADM on the other hand is that the grid can be very coarse in rotor plane, only limited by the scales required by turbulence model.

2. *ADM with BEM*: As an additional feature to standard ADM, in ADM-BEM, aerodynamic properties of the blade are also taken into account for force calculations. Rotation of the rotor is modeled in this case, which results in the generation of wake rotation. In theory and practice, ADM-BEM resembles a wind turbine better than the standard BEM due to existence of additional energy lost to wake rotation. Instead of a homogeneous distribution in all directions, forces vary in the radial direction only and are considered to be constant in the azimuthal direction; i.e forces are distributed homogeneously in annular rings such as:

$$f_{2D} = 0.5\rho U_{ref}^2 c(c_l \mathbf{e}_l + c_d \mathbf{e}_d) N_B / (2\pi r) \quad (1.1)$$

where \mathbf{e}_l and \mathbf{e}_d are unit vector directions of lift and drag, respectively. Here, 2D lift and drag forces at a section are calculated, then multiplied by the number of blades and finally averaged over the annular ring circumference.

Lavaroni et al. [46] have studied both standard and BEM based ADM with two back-to-back turbines configuration, where the additional complexity for BEM based ADM was the necessity of tabulated airfoil data. Both unsteady RANS ($k-\omega-SST$) and LES turbulence models were employed. LES model was zonal, i.e. applied

only to the most refined regions. Atmospheric conditions were neutral, atmospheric turbulence was absent. Results were validated with wind tunnel measurements. Wake velocity profiles undoubtedly showed the superiority of BEM based ADM, where non-rotating ADM yielded almost linear and undisturbed velocity deficit profiles, which is non-realistic in a real wind turbine flow. LES models invariably captured the increase of turbulence at the top tip better than RANS models. Inclusion or exclusion of BEM for the same turbulence model had no impact on turbulence levels calculated at this point. Both models have under-predicted the velocity deficit overall. In RANS simulations, it was possible to reach steady state solutions, which was not the case with LES.

Jimenez et al. [47] applied the ADM technique with a simplified LES model. Anisotropically turbulent atmospheric flow was simulated using LES based on Smagorinsky's eddy viscosity SGS model. Turbine blade geometry was not detailed in the used ADM method. The grid was considerably coarse. Bottom boundary was considered as a flat ground, boundary conditions at this surface was derived from a wall function which is mostly used in meteorological applications. No grid refinement was applied to the ground vicinity. Despite the absence of a detailed definition of turbine blades, obtained turbulence characteristics are found to be in good agreement with analytical correlations and measurements. Calculated Reynolds stress tensors throughout the domain were very close to experimental data. The developed LES model was capable of yielding useful information on flow oscillations and eddies with length scales larger than grid size, as well as mean turbulence characteristics. An important detail in the study was that a constant thrust value was used as in many other ADM simulations in the literature.

It is a common practice to pre-bend wind turbine blades to tolerate bending due to aerodynamic loadings during operation, which is called coning. Mikkelsen et al. [48] used ADM to investigate the coning effect on a 2MW turbine with comparisons against pure BEM. To take the blade geometry into account, they have also coupled ADM with BEM methodology. BEM coupling has allowed variations of velocity triangles due to coning to be captured. Although the turbulence closure method was not stated explicitly, 3D RANS equations were solved. First, constant $C_T = 0.89$ case was studied. Rotor was defined based on the projected area of the coned rotor,

instead of using span radius and non-coned geometry directly. Under this condition, power coefficient was insensitive to the amount of coning. Reynolds number and grid resolution dependency study showed that a solution which is independent of both variables has predicted C_P slightly exceeding the Betz limit. They have concluded that ADM gives better results for large blade deflections and cone angles compared to BEM. In terms of BEM coupled ADM versus constant thrust ADM, BEM coupled ADM outperformed the method where blade geometry information was absent.

Porte-Agel et al. [49] have introduced an advanced LES approach for wind farm simulations where sub-grid scale momentum turbulent fluxes are modeled dynamically and scale dependence is captured locally. This approach yielded better results than static models, like classical Smagorinsky, and dependence on grid resolution was somewhat dealt with. Wind turbines were modeled using ALM and ADM with and without rotation. To obtain a fully developed atmospheric sheared layer at the inlet boundary, they used a buffer zone of $2D$ length. Results were compared to data obtained from hot-wire experiments. The proposed method was tuning-free and results were very close to the measured data. ADM with rotation and non-homogeneous force distribution yielded better force and wake predictions and results were very close to that of ALM. Non-rotating ADM has clearly over-predicted mean velocity in the near central wake region, showing that ignoring the rotational effects causes loss of crucial wake information. Turbulence intensity in the wake region reached the peak value approximately at $3D$ - $5D$ downstream distance, which was also in agreement with wind tunnel measurements.

Simisiroglou et al. [1] have tested the ADM in three cases: single wind turbine, two in-line wind turbines under low turbulent uniform inflow and same case with high turbulent sheared inflow with various separation distances. Four different RANS based turbulence models are tested: $k - \varepsilon$, $k - \varepsilon - RNG$, $k - \varepsilon - KL$ and $k - \omega$. Predefined thrust coefficient C_T vs inflow velocity U_∞ data are used to calculate the rotor thrust force, but different ways of distributing this force to cells enclosed by the rotor are investigated: uniform, polynomial, triangular and trapezoidal. Trapezoidal method was adjusted to resemble ALM-obtained thrust distribution. Type of thrust distribution had a distinctive effect in the near wake region and lost significance at farther downstream positions. Uniform thrust distribution turned out to be the best

method in predicting overall wake profiles, but authors emphasized that this might not be the case for the near wake zone of a full size rotor. Wake characteristics changed dramatically with turbulence model; standard $k - \varepsilon$ and $k - \varepsilon - KL$ gave the best agreement with measurements whereas $k - \omega$ was the worst performing. Turbulence intensity at the inlet also had a big impact on wake development and high turbulence yielded better results.

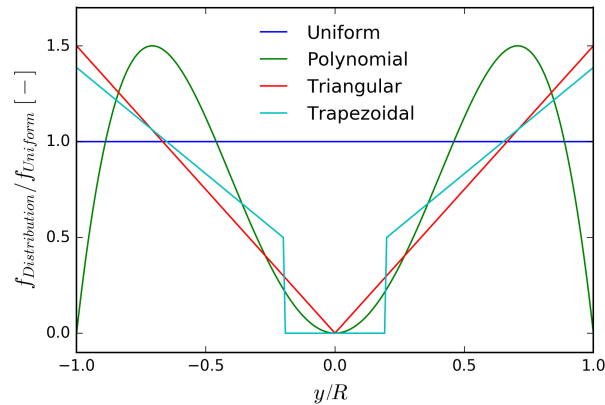


Figure 1.2: Thrust force distributions along the actuator disc tested by Simisiroglou et al. [1].

1.3.2 Actuator Line Model (ALM)

In ALM, instead of using the swept area, each blade is physically and discretely modeled in the domain. Instead of resolving the blade geometry and boundary layer, in a BEM-like approach, lines that represent the blades are divided into sections (Fig. 1.3). Each section has its geometrical specifications, i.e. radial position, chord and twist, as well as the airfoil profile. Additionally, each section is represented by a point, where aerodynamic forces are calculated locally, using 2D airfoil theory. This calculation requires angle of attack and velocity magnitude values, which are obtained from the domain. Where and how to get these data from the domain for each actuator point is called **velocity sampling** and it is a major unknown in ALM. It has a dramatic impact on accurate force calculations, and accordingly, wake predictions. The advantage of ALM over fully resolved mesh simulations comes from already-available C_l and C_d data. This data is tabulated for a range of angle of attack and Reynolds number values before the run and requires no computation during the simulation, but only interpolation. Reynolds number here

is also a variable, because it varies significantly over the span, due to rotational speed and chord length. Hence, multi-Reynolds simulations are expected to yield better results than single-Reynolds simulations. After the force is calculated, it is distributed among the cells in the vicinity of actuator point, instead of being applied to the nearest cell as a singular force directly. This is a crucial practice in preventing unstable and oscillatory solutions. Distribution is commonly done in the shape of a sphere, where each cell's weight is determined via a 3D Gaussian distribution. This is called **force projection**. The second most important question in ALM is the width (or radius) of this projection sphere, which is controlled by a parameter in Gaussian distribution function. This parameter shows up in the distribution equation as ϵ and is referred to as Gaussian kernel. It controls the projection width and radius of the sphere in which the calculated force (from 2D airfoil theory) is distributed. Together with these two variables, simulation parameters such as grid resolution, time step size and turbulence modeling are also ambiguous and not well-defined in the literature.

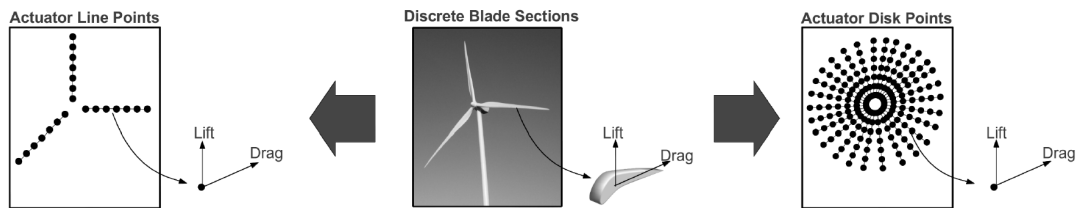


Figure 1.3: *Division of blades into actuator points in ALM and ADM (Source: [2]).*

Despite its numerous variations, due to the areal averaging, ADM could not generate the tip vortices that are entrained into wake. ALM on the other hand, due to representation of each blade discretely, is capable of predicting helical vortex structures in the wake region. Although both methods yield similar results in the far wake region due to dissipation of vortices, ALM has an apparent advantage in the near wake region where vortical structures are significant.

Actuator Line Model was first introduced by Sorensen and Shen [50]. Instead of the primitive variables (velocity-pressure), a velocity-vorticity based finite difference flow solver was used in cylindrical coordinate system. Authors did not give the specifications on velocity sampling methodology, but stated that tabulated 2D airfoil data was corrected for 3D effects and blade aspect ratio. This was due to rotational effects limiting the boundary layer growth and causing higher lift than 2D

calculations. 2D airfoil data was tabulated for an angle of attack range of $\alpha = -10^\circ$ to 110° , which is quite large when a typical wind turbine geometry is considered. Forces at each section were calculated in a way similar to the BEM approach. A regularization kernel in the form of 3D Gaussian distribution was applied to calculated forces to smooth out the force distribution in an attempt to resemble the pressure distribution over a real blade surface. Up to a certain inflow velocity, results were in excellent agreement with measurements. However, power was over predicted at higher free stream velocities. Vortex shedding remained distinguishable in the shape of vortex tubes for 2 full rotations downstream. This length for diffusion of helical vortex structures was found to be small compared to measurements, and this was attributed to the grid coarseness and low Reynolds number. Compared to experimental data, flow field results were found satisfactory overall.

A quantitative assessment of ALM can be done from the paper of Krogstad and Eriksen [51]. In this study, blind test results obtained from many researchers for the same wind turbine under same conditions were compiled and compared to each other. Used methods vary from BEM to ADM and ALM based LES. Very far downstream, i.e. $x/D = 10$ measurements was not available. Independent of the method, power production estimations were in an acceptable limit, however, results for velocity deficit and turbulence in the wake has shown a significant uncertainty. Authors have specifically concluded that Large Eddy Simulation yielded the most respectable results amongst others, also emphasizing the necessity of coupling it with a time-resolved method where blade details are present. Overall, ALM results were closer to the measurements than that of ADM. One interesting observation was LES had no superiority over RANS based turbulence models in time averaged simulations, such as ADM. A similar report was published by Sætran et al. [52] for another blind test, where two turbines were placed back-to-back with a certain amount of lateral offset. In addition to the complementary conclusions, results have clearly showed that LES was the only model to be consistent for various boundary conditions and reproducing the experimental data. ADM and ALM outperformed other methods in capturing turbulent stress and mean velocity profiles and standard $k - \varepsilon$ model fell behind LES in terms of accuracy.

Tabib et al. [53] have simulated an operational wind farm with 25 turbines which

are modeled with ALM. The highly complex terrain was geometrically resolved instead of being modeled via surface roughness coefficients. Both RANS and LES turbulence models were tested under neutral atmospheric conditions and predictive capabilities were assessed. OpenFOAM's transient incompressible solver was used. Grid resolution was considerably coarse; turbine diameter was 60m and finest cell size was 6m in the turbines region, corresponding to $\Delta_g/R = 1/10$. It was not explicitly stated whether or not the same resolution was used in both RANS and LES simulations. Blade geometry was defined in 40 actuator points, i.e. $\Delta_{AP}/R = 1/40$. Simulation has taken 15 flow passages throughout the domain to reach a quasi-steady state. Individual and overall power predictions were higher in RANS simulations compared to LES. Wake effect was significantly more pronounced in LES compared to RANS, because of higher turbulent momentum diffusion in RANS due to larger turbulent kinetic energy prediction. This caused downstream turbines to experience lower incoming mean velocities, thus the less power production. Vorticity contours showed that vortical structures were more distinctive in LES and were extending from one turbine to another, whereas significant wake decay in RANS simulations caused vortices to disappear rapidly. Higher terrain induced wake predictions by RANS has also played an important role in faster wake decay and higher power production estimation.

Benard et al. [9] have studied both near and far wake regions using ALM with an LES solver. They have assessed the technique on both structured and unstructured grids. Two cases were run; one with the turbine isolated from domain boundary effects and one with ground present. Due to computational concerns, a wall model was used instead of wall-resolved LES at the bottom boundary. A log-law wall model based wall shear stress was imposed to non-rotating regions in the domain. From the grid convergence study, authors concluded that the required grid resolution at the rotor plane for accurate results should be no coarser than $\Delta_g/R = 1/66$ and actuator point spacing should be approximately equal to grid spacing. 1st, 2nd and 4th order accurate spatial discretization schemes were tested. Although the grid resolution was constant, vorticity contours were significantly diverse just by changing the scheme order. 1st order scheme yielded very poor results in the wake region, helical vortices disappear after 1D downstream position. Order of discretization scheme was found

to be critical in capturing the wake development and use of high order schemes with lower dispersion and dissipation was suggested, especially on unstructured grids, which are mandatory to resolve highly complex terrains or even nacelle and tower.

In their recent study, Tzimas and Prospathopoulos [54] have employed three actuator models: uniform thrust based ADM, BEM based ADM and transient ALM. An in-house compressible RANS solver was used and two turbulence models were tested: $k - \omega - SST$ and Spalart-Allmaras. Time step size was determined based on a maximum angle per time step approach, such that the rotor would rotate 1° at each time step. Three different wind turbines were modeled. Axial force was predicted adequately at low inflow speeds but calculated tangential forces were divergent. At low free stream velocities, every method yielded acceptable results. However, as wind speed increased, due to increasingly prominent 3D effects like separation and stall, calculated local lift and drag forces were far from the measurements. Although near wake prediction of ALM was better than ADM, all methods have significantly underestimated the velocity deficit in that region. Discrepancies in wake profiles became minimal towards far wake zone. Overall performance in wake predictions were found to be poor and this is attributed to the shortcoming of two-equation closure models in estimating normal stresses and turbulent kinetic energy accurately. A finer grid with LES was suggested for better performance.

Bachant et al. [55] implemented an ALM code in OpenFOAM to simulate high and low solidity Darrieus type vertical axis wind turbines. To capture rapid changes in angle of attack due to the type of VAWT, a dynamic stall model was added. Also, sub-models for tip correction, added mass and rotation flow curvature corrections. High and low solidity turbines were simulated with Smagorinsky LES and $k - \varepsilon$ RANS turbulence models, respectively. Comparisons against experimental data has shown that both turbulence models has over predicted both torque and thrust at higher tip speed ratios, that are larger than the peak C_P value of the turbine. Although mean velocity profiles were in very good agreement with measured data, the biggest discrepancy has been seen in the turbulence kinetic energy profile at the hub height in RANS simulation, where LES model performed better. This was attributed to the less dissipative solution of LES. Power prediction in the RANS simulation of medium solidity wind turbine was also in overall disagreement with experimental

results. Nevertheless, authors concluded that ALM was capable of reflecting the flow physics better than potential flow based vortex models or ADM.

Jha et al. [56] have reviewed some of the important ALM parameters extensively in their study, primarily Gaussian ϵ and grid resolution, and proposed a general guideline to determine these parameters. They suggest that, especially for LES simulations, grid should be fairly isotropic and aspect ratio of cells should have very low (close to 1). Constant (cell size based) and chord size dependent force projection width approaches were tested on two wind turbines with different blade aspect ratios: NREL-Phase-IV and NREL 5MW. In addition, a new method to determine Gaussian ϵ that varies along the span is suggested, which resembles an elliptic wing by fitting an ellipse to the blade planform area. Various Δ_g/R , ϵ/Δ_g , ϵ/c and ϵ/c^* values are tested, where c^* is the ellipse-fitted chord length. Results showed that constant ϵ leads to over-predicted loads in the tip region of blade, however chord-based ϵ also fell short in accurate blade loading predictions. Two approaches showed different behaviors in low and high aspect ratio turbines. Ellipse-fitted chord dependent ϵ was found to yield closest results to experimental measurements. A reason for criticism on c^* based ϵ was the fact that it would not reflect a realistic pressure distribution over the blade, especially in the root region, where c^* is very small compared to large chord lengths in a real blade.

Yu et al. [57] simulated two NREL 5MW wind turbines in axially aligned position using ALM on OpenFOAM. RANS equations were solved with PISO algorithm and $k - \omega - SST$ turbulence model. First order implicit Euler scheme was used for time marching, gradient and divergence terms were solved with linear Gauss and linear upwind methods, respectively. Mesh in the wake zone was only refined at regions where the vortices shed from tip and root would advect along, hence some computation time was saved on. Different levels of grid resolutions have been tried, up to $\Delta_g = 3m$ and mesh independence study show a convergence at 6 million cells. 2D airfoil data was addressed to be unreliable at high Reynolds number and flow velocity zones. Q-criterion iso-surfaces were plotted for various free stream velocities (5, 8, and 11.4 m/s), where spacing in helical structures were distinct for each value. The tower has been introduced into the flow field as a static actuator line and its effect on power history was clearly visible as a drop at each $1/3^{th}$ full rotation. Shape

of the wake profile underwent a change from W to U (hub presence) at around 3D downstream distance and complete wake recovery was achieved at 8D downstream position. In the case of dual wind turbines, various tip speed ratio values ranging between 3.5 and 7.55 were tested on the downstream turbine and power coefficients were plotted. Optimum TSR value for the downstream turbine was found to be 6.1. Distance between two rotors was set as 7D and this concluded to be the optimal separation.

Troldborg's Ph.D. thesis [58] is one of the most cited studies among ALM researchers. He studied ALM extensively in method's relatively early years; under uniform and sheared inflow conditions, sensitivity to atmospheric turbulence, numerical parameters such as time step, solver type, differencing scheme and boundary conditions, single and multiple turbine configurations. A solver which is formulated in pressure-velocity variables is used along with LES method. Optimum Gaussian kernel value was suggested as $\epsilon = 2\Delta_g$ which is often used as the reference ϵ value in many papers. The study found that very small ϵ values causes oscillations and *wiggles* in blade force distributions. Introduction of turbulent perturbations has been shown to cause earlier breakdown of tip and root vortices. Non-uniformities of flow at the rotor plane caused skewed behavior of wake throughout the domain. A case with 3 turbines in a row is also studied, with and without turbulent fluctuations. It was found that laminar inflow case resulted in much more stable tip vortex structures and hence lower mean velocity magnitudes acting on the second wind turbine. Wake meandering was most visible in the turbulent inflow case. Sheared inflow simulation has also revealed extreme tilt moment experienced by all turbines, as well as yaw moments became prominent on downstream turbines due to wake generated by upstream rotors.

Draper and Uner [59] have evaluated the fidelity of ALM at grids that are much coarser (up to $\Delta_g/R = 1/8$) than usually suggested resolutions (around $\Delta_g/R = 1/30$ to $1/60$). Study was carried out for a single tip speed ratio and no tip loss correction was applied. Relations of wake profiles, power and thrust values with Gaussian smearing and time step size were investigated. Computed turbine power turned out to be strongly dependent on chosen projection width. Sensitivity to time step size also decreased as the Gaussian ϵ became larger. No clear relationship

between Δ_t , Δ_g , ϵ and error in power could be established. Among the big issues was the fact that although a reasonable ϵ value was found to match the rated conditions of wind turbine, same ϵ yielded over and under-predicted power productions in higher and lower tip speed ratio values, respectively. This showed that authors' model was dependent to rotational speed. In both cases, when a downstream turbine was placed, power error in that turbine was even larger than the upstream turbine. When small fluctuations were added to the free stream, better results were obtained in the wake area compared to laminar inflow case. Application of tip loss correction has changed the power characteristics of wind turbines dramatically and is found to be crucial in ALM simulations, despite the fact that wake remained fairly unresponsive to existence of tip corrections. Projection width and grid resolution had a big impact on calculated forces.

According to Martinez-Tossas and Meneveau [60], optimal Gaussian kernel size to obtain high fidelity results in ALM is very small (around 1/4 chord size) but much coarser values are used in practice. Hence, authors have aimed to develop a model that would mimic a fully resolved blade's vortex structures with a sub-filter model usable in LES with large Gaussian kernels. It is called sub-filter scale velocity model, based on a Gaussian-filtered lifting line theory. This approach differs from classical Prandtl lifting line theory by defining a length scale at each blade section along which the vorticity is distributed, whereas Prandtl's suggestion was infinitesimal vortex sources. This length (ϵ) was found to be optimal at $\epsilon/c \approx 1/4$. For simulations where resolving this thickness in sub-grid scale is not computationally possible, this study proposed a correction on sub-filter-scale velocity. Results were obtained via LES and compared against theoretical lifting line theory and very good agreement was observed. One major drawback of the developed method is shown to be the assumptions made; primarily neglecting turbulence effects and viscosity, but this was justified by pressure distribution being fairly insensitive to such effects.

Merabet and Laurendeau [61] has conducted a 2D study on parameters used in velocity sampling techniques for ALM. Actuator Line implementation was done in STAR-CCM+ flow solver. They addressed the issues of using values at the closest cell for velocity sampling and examined several other approaches: averaging a certain number of cells, bi-linear interpolation, integral velocity sampling and point

vortex correction. Instead of 3D, sampling techniques were investigated in 2D in the study, i.e for a single actuator point instead of the complete actuator line. Various grid resolutions were tested, where Δ_g/c varies between 2 and 0.0625. Larger mesh sizes yielded larger errors. At flow regimes where incompressibility or inviscid assumptions are near-invalid, all sampling methods has diverged from reference values. It was concluded that the integral velocity sampling method almost always performed better than others in power production and it was the most consistent with mesh size variations. This method was also praised for not being dependent on corrections or parameter tuning like others and its better applicability on unstructured meshes. Interpolated point sampling at the circulation yielded good results also, but authors noticed that it might be avoided by non-isometric Gaussian methods which are leaned towards by researchers recently.

Martinez-Tossas et al. [62] have employed both ADM and ALM to simulate wind turbine wakes using LES. Two of the most important parameters in actuator-based simulations were studied: force projection method and grid resolution. NREL 5MW rotor was simulated at optimum wind speed and TSR point, since the energy extraction is maximum and wake structures are the strongest. Rotational speed was kept constant and electrical efficiency was neglected. Cell size was uniform in all directions; $\Delta_g = 4.2, 2.1, 1.05$ values were experimented with. Tested Gaussian ϵ values were 2.1, 4.2, 6.3, 8.4, 10.5. Results were compared to BEM solutions. Both methods predicted similar power productions on fine grids. ALM was more sensitive to cell size compared to ADM, since singular forces were projected to the domain in ALM and forces were already averaged before projection in ADM. Grid resolution was also found to have an impact on wake profiles. Smaller values of cell size (and accordingly smaller ϵ values) caused an earlier transition to turbulence in the wake. Grid independence was reached at $\Delta_g < \epsilon/5$. It was found that both refining the grid and increasing the force projection width caused higher power production estimations. Only uniform and non-turbulent inflow case was investigated, where ADM yielded power production results very close to ALM within 1% margin. Although tip and root vortices generated by the blade were quite more distinctive in ALM, both methods resulted in similar wake predictions in the far wake region.

Fleming et al. [63] have successfully used ALM to study wake-redirection by

tilting and yawing rotors in wind farms. To obtain the fully developed atmospheric sheared inflow, a precursor simulation with periodic boundary conditions was run beforehand. Later, result of this simulation was used at the transient inflow boundary of wake study. In the code used, local angle of attack and relative velocity values are calculated in `OpenFOAM` by velocity sampling, then sent to a loosely coupled secondary BEM solver, which applied partial BEM calculation (by using sampled velocity values instead of induction factors), and finally computed forces are sent back to `OpenFOAM` to be applied to the flow field. NREL 5MW wind turbine was used. Results such as forces acting on turbine structures, bending on blades and overall farm production were obtained for various tilt/yaw scenarios. Yaw misalignment showed a significant change in wake center, reducing the wake effect on downstream turbines but increasing the cross-loadings at the yawed rotor. Although wind turbines are not tilt-controllable in practice, study has shown that tilting the rotor has increased the overall production of the wind farm and might be considered as a feature in turbine development.

Martinez-Tossas et al. [64] have studied the breakdown of vortical structures in wind turbine wakes and their relation with sub-grid modeling using both an in-house code and `OpenFOAM` solver. Two sub-grid modeling types were tested, which are standard and dynamic Smagorinsky models, where the Smagorinsky coefficient C_S is constant throughout the domain or calculated as a space and time, respectively. Gaussian ϵ was kept constant. Results were compared to BEM solutions. Two solvers showed significant discrepancies in wake velocity contours at higher C_S values, where results at smaller C_S values were very close. Higher C_S predicted a later transition due to damping effect of higher sub-grid viscosity ν_{SGS} . SGS model did not affect the velocity field up to 4D downstream, however Reynolds stress components were very sensitive. Also, blade loadings turned out to be not affected by the type of sub-grid model used, however wake characteristics and turbulent transition location were highly sensitive. Authors have also suggested that although there are no well-established methods to estimate, a well chosen constant C_S would yield similar results to that of dynamic C_S , saving computation time.

Churchfield et al. [65] have proposed a new velocity sampling approach to calculate blade loadings more accurately. Due to classical velocity sampling methods being

ambiguous and incapable of estimating near wake details accurately, authors have suggest a new integral free stream velocity sampling method with a non-isotropic body force smearing function instead of point-sampling. In the new method, a force projection function was derived and applied to calculated forces in accordance with the integral of velocity field. Results were compared to BEM solutions for NREL 5MW rotor and experimental results as well for NREL-Phase-VI rotor. The new method removed the uncertainty of monitoring location for velocity vectors, ruled out the necessity of empirical corrections and was found to be less mesh-dependent. Non-isotropic Gaussian method predicted lift forces and axial velocity along the span better than isotropic Gaussian approach. One important finding was that the classical point velocity sampling method produced oscillatory power history which should be absent in non-turbulent conditions and this was attributed to linear interpolation of bound vortices at discrete locations being prone to errors.

Realizing the lack of literature on effect of atmospheric turbulence on wind turbine wakes, Troldborg et al. [3] have investigated the behavior of vortical structures and meandering formation in turbine wakes in terms of turbulence characteristics in a non-sheared inflow. In the case of uniform inflow conditions without atmospheric turbulence, conditions at 10 rotor radii downstream was determined primarily by root and tip vortices, since they have remained stable without breaking up. With introduction of turbulent perturbations to external flow, this distance has dropped to 4 rotor radii where organized structures became non distinguishable and the solution has underwent a dramatic change (Fig. 1.4). One interesting outcome of the simulations was that the root mean square of axial velocity was higher in the far wake region ($x/R \approx 14$) when inflow turbulence was not included. This led to the conclusion that estimating the wake of a wind turbine by adding up atmospheric and turbine induced turbulence in unsteady simulations would not necessarily give good results. Authors have concluded that coherent structures in the atmospheric turbulence dominates large-scale wake motion and also turbulence is more isotropic in the far wake region compared to outside flow.

ALM can compute vortex structures in the wake region better than ADM, but this comes at the cost of 20 to 40 times smaller time step sizes. This becomes much more limiting than the CFL condition. Nathan et al. [66] have proposed a new

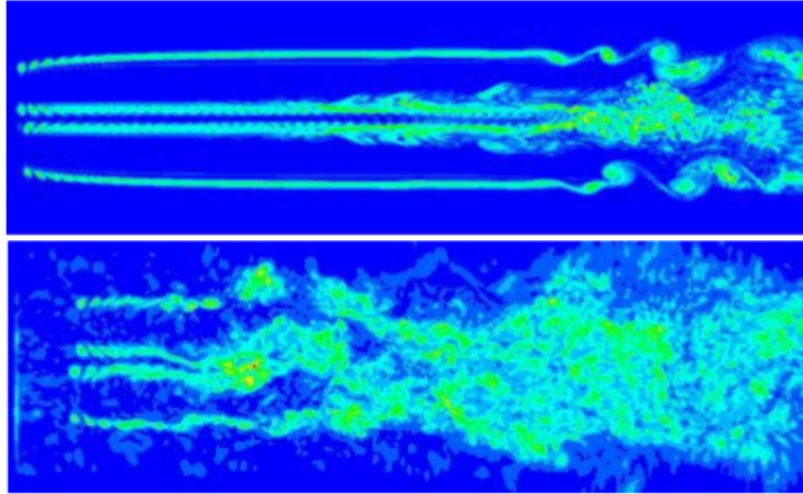


Figure 1.4: *Troldborg's wake results with (top) and without (bottom) atmospheric turbulence shows its impact on the ALM solutions [3].*

approach to overcome much finer spatial and temporal resolution requirements of ALM when compared to ADM. They suggested a *swept ALM method*, in which lines are swept for a certain amount of angle for each time step, which can be considered as a partial ADM. Solutions were obtained in `OpenFOAM` using the transient PISO algorithm and LES. Although execution time per time step was increased by 1.45 times, total execution time has dropped by $1/5^{th}$ compared to classical ALM. One of the major drawbacks of the new method showed up in the resultant torque values, where ADM had a better agreement with reference values. This was attributed to the complexity of velocity sampling in swept-ALM, where angle of attack and relative flow are computed at the latest position of each blade but are applied to the whole swept area. Although helical vortices (which are as much as the number of blades) shed from the blades became less distinct in the swept-ALM, new method were found to be promising with further improvements.

Matiz-Chicacausa and Lopez [67] has simulated a downwind-type wind turbine, i.e. which has its rotor located behind the tower. Simulations were carried out with `OpenFOAM` RANS solver for NREL Phase-VI wind turbine, which has 12.2 m diameter and 10 m hub height. Grid resolution was 50 cells per rotor radius ($\Delta_g/R = 1/50$). Effect of wake generated by the tower was clearly observable in the power history of wind turbine, which is called *tower shadow*. Different values of Gaussian kernel ϵ were tried and its effect on blade force distributions were assessed

by comparing against experimental data. ϵ was found to have a dramatic impact on the tangential force predictions, whereas axial forces were relatively insensitive to it. Although loading predictions were in very good agreement in mid-span regions, ALM showed some discrepancies close to the blade tip (where tangential velocity is high) and authors suggested that a chord length based Gaussian ϵ should be used towards the blade tip ($r/R > \approx 80\%$). It was also highlighted that vortical structures in the wake were not noticeable due to URANS approach, and LES was recommended to capture such detail.

Rai et al. [68] developed a generalized ADM/ALM framework to overcome load balancing issues in parallelization and implemented to an in-house LES solver. An intermediate module connects the meso-scale solution (which provides transient initial and boundary conditions) to micro-scale solver, where ALM is employed. For load balancing, actuator points are prioritized during distribution of cells among processors. Developed code was applied to both complex and flat terrains. Validation was done in both uniform and WRF coupled full-scale wind farm simulations. Discrepancies at high wind speeds were attributed to the absence of stall models in 2D airfoil calculations. In the complex terrain case, elevation of a turbine was found to have an effect on the power production due to ground-rotor interactions. Power production of some turbines in regions with steep elevation variation were over estimated, showing the importance of accurate ground interaction modeling and wall treatment choice. It is emphasized that accuracy of wind farm simulations heavily depend on reproducing the inflow conditions (primarily turbulence characteristics) correctly.

Bühler et al. [69] have used ALM to simulate both a helicopter and a wind turbine rotor in the same domain to investigate the impact of turbulent structures in the wake generated by wind turbines on a hovering helicopter. The study has a significance of using ALM on rotors which are at the two extremes of length and velocity scales in the same domain (i.e. $D = 126m$ and $n = 12RPM$ for the wind turbine vs. $D = 10.2m$ and $n = 395RPM$ for the helicopter). In the paper, a newly developed angle of attack calculation and velocity sampling method was compared to two other methods, one of which uses the actuator point itself as the monitoring point and other uses a point upstream of the airfoil. It was suggested that angle of attack and relative velocities

are better predicted by averaging values at some number of monitoring points around airfoil sections. Blade loadings and angle of attack distributions on wind turbine blades were compared to fully resolved mesh results and a good agreement was found. Vortex and Q-criterion iso-surfaces were visible and transient thrust force instabilities acting on the helicopter were calculated.

Apsley et al. [70] investigated several turbulence models in their recent paper, including $k - \varepsilon - Standard$, $k - \varepsilon - Realisable$ and $k - \omega - SST$. In addition to isolated rotor simulations, multi-rotor arrays were also simulated. Several lateral and axial spacing scenarios were studied. Effect of wake was apparent in velocity deficit profiles up to 4 rotor diameters downstream. They have found that choice of turbulence model has little to no effect on blade loadings of an isolated rotor, but it makes a significant difference in wake profiles. This makes simulations with multiple wind turbines dramatically dependent on turbulence models, where power production is affected by wake interactions. ALM was also capable of capturing large cyclic loading fluctuations on the blades of downstream turbines. Compared to other eddy-viscosity and Reynolds-stress-transport models, $k - \varepsilon$ was found to be more diffusive in the near wake region.

Sorensen et al. [71] simulated an isolated small-scale NTNU wind turbine using ALM along with LES. Incompressible PISO algorithm was adopted. A regular Cartesian grid was used, where number of actuator points along blade span was 43, the mesh composed of 24.5 million cells and cell size was homogeneous in the rotor vicinity. Inflow was uniform and atmospheric turbulence was implemented by applying body force fluctuations at the inlet boundary. This was primarily used to investigate the stability of vortices shed from tip and root. Purpose of this was to assess the frequencies that starts vortex break down in wake spirals, by computing present stability modes and their growth. Rotor performance and wake characteristics were compared against experimental data. ALM has predicted power and thrust vs tip speed ratio curves very close to experimental data. Also in the study, analytical expressions were formulated to estimate near wake length and wing tip vortices break down length.

Wimshurst and Willden [72] carried out an ALM validation study on MEXICO

rotor using OpenFOAM. Validation is done on experimental blade loading and wake measurement data where PIV methodology is used. RANS equations were solved with $k - \omega - SST$ closure. A block-structured mesh was used instead of a fully structured Cartesian grid, where a physical inner boundary for nacelle representation was defined. Hence, cell size was not constant along blade span but rather increasing gradually. It was found that presence of nacelle and grid resolution in the near wake region have very little influence on calculated blade loadings but have a significant impact on near-wake velocity profiles. Also, constant and chord length based force smearing methodologies were investigated with 3 different ϵ values. They have concluded that chord-based projection width gives significantly better tip vortex predictions compared to constant ϵ approach, while blade loading computation is less sensitive. Tip correction factor was found to have a dominant effect on accurate loading predictions in ALM.

1.4 Objectives

Review of recent studies on ALM based wind turbine and wake simulations show that a majority of research is concerned with simulation parameters, such as projection width, grid resolution, velocity sampling and time step size selection. This is due to the ambiguity of determination of these parameters, as well as their effect on computational economy when it comes to full-scale wind farm simulations with multiple wind turbines, which is the ultimate goal of ALM approach. In terms of turbulence, LES shines out as the most widely used method, although RANS based turbulence closures are occasionally used. Despite the fact that LES gives high fidelity results, its computational demand remains considerably high compared to RANS simulations where cheaper one or two equation turbulence models (like Spalart-Allmaras or $k - \epsilon$, respectively) are employed. On the other hand, ALM was shown to be very sensitive to grid resolution in blade loading predictions. Many papers suggest $\Delta_g/R = 1/30 - 1/60$ for accurate results. This level of refinement is close to satisfy LES-scale atmospheric flow grid resolution requirements. Also considering the fact that LES offers much better turbulence resolution (which is crucial in wake structures), LES serves better for the purpose of this study.

In this study, an ALM code is implemented into a flow solver and tested for various cases. Navier-Stokes equations are solved and LES model is employed in terms of turbulence closure. In Chapter 2, details of solver, Actuator Line Model and numerical methods used are given. Several simulation parameters are experimented with and their effect on the accuracy of ALM are assessed in Chapter 3, also results are presented including a rotor isolated from boundaries, rotors in tandem configuration under sheared flow and yawed/non-yawed orientations. Turbine performance, blade loading and wake profiles are compared against numerical (BEM and FRM) solutions to verify ALM's accuracy. Parallelization and computational cost are also discussed. Finally, concluding remarks are presented in Chapter 4. Findings of this study are also expected to be used in pre-simulation parameter decisions in future ALM simulations and lead to full-scale wind farm simulations.

CHAPTER 2

METHODOLOGY

In this study, CFD simulations of a full scale model wind turbine are carried out, findings are compared to results obtained by other methods and presented by other studies. Incompressible and unsteady Navier-Stokes equations are discretized to obtain time-accurate numerical solutions. Spatial discretization (generation of the grid) and solution are done in open source flow solver OpenFOAM modules [73]. Turbine blades are introduced into the solution domain using ALM to save on computational cost. ALM implementation is done by the OpenFOAM library extension `turbinesFoam` [74]. Necessary 2D airfoil calculations are done by low Reynolds Number airfoil analysis code XFOIL [75]. BEM results are often used as reference for validation and verification, the open source BEM code QBlade is used for solutions [76]. NREL's 5MW reference wind turbine [77] is chosen as the test turbine.

2.1 Basics of Wind Power

Understanding wind energy and turbine aerodynamics starts with the actuator disk representation of the rotor. This approach is commonly referred as *1D Momentum Theory*. It is the most idealized case where fluid flow is assumed to be 1D, incompressible, inviscid and irrotational. The flow going through the disc is contained within a stream tube and the disc acts as a momentum sink only in axial direction. Since wind turbine is a device which extracts energy from the flow, velocity of air drops as it passes the rotor, hence the stream tube expands. Total thrust force and power available in the flow passing through an area A_r are respectively

calculated as:

$$T_{wind} = 0.5\rho U_{\infty}^2 A_r \quad (2.1)$$

$$P_{wind} = 0.5\rho U_{\infty}^3 A_r \quad (2.2)$$

Thrust and power captured by the wind turbine is usually normalized with respect to the amount available in the wind as a performance measure. Resultant non-dimensional values are used as primary performance parameters and denoted as thrust and power coefficients respectively:

$$C_T = \frac{T}{T_{wind}} \quad (2.3)$$

$$C_P = \frac{P}{P_{wind}} \quad (2.4)$$

In 1D momentum theory, it is assumed that pressure is equal far up and downstream with a discontinuous jump at the rotor plane and axial velocity changes smoothly (Fig. 2.1). Velocity loss at the rotor plane $U_{\infty} - U_r$ is normalized by the free stream

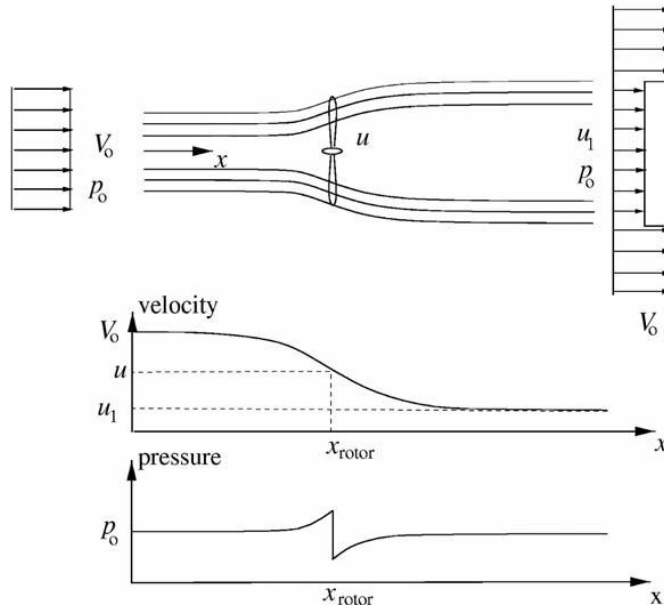


Figure 2.1: Flow through a porous disk in 1D momentum theory. (Source: [4])

velocity and denoted as the axial induction factor:

$$a = 1 - (U_r/U_{\infty}) \quad (2.5)$$

Thrust exerted on the turbine is due to the pressure difference across the rotor. Power is calculated by taking the stream tube as the control volume and applying energy

conservation. Using Bernoulli equation, induction factor definition and with further manipulations, thrust and power coefficients can be found as functions of axial induction factor:

$$C_T = 4a(1 - a) \quad (2.6)$$

$$C_P = 4a(1 - a)^2 \quad (2.7)$$

Eq. 2.7 implies that there is a maximum power obtained at a certain axial induction value. Indeed, even in this ideal case, converting the wind flow into usable energy with a hypothetical 100% efficiency is impossible since it means bringing the flow to a complete stop, contradicting the continuous flow case. Optimizing C_P yields $a = 1/3$ for maximum energy extraction, where the idealized disc can not extract more than $16/27$ (≈ 0.593) of the kinetic energy available in a continuous flow. This is known as the Betz Limit [40].

2.1.1 Generalized Momentum Theory

For a better wind turbine resemblance, rotation should be added to the rotor, which also imparts rotation to the flow going through itself. Glauert [41] has generalized the non-rotational 1D Momentum Theory to allow tangential flow. This model is known as the *Generalized Momentum Theory*. Disc is now divided into differential annular elements which rotates with the angular speed Ω . Key assumptions are: rotation does not affect the upstream and downstream flow experiences a tangential component just behind the rotor, imparted by the rotating annuli. Tangential induction factor, local speed ratio and tip speed ratio show up as some of the important parameters and they are respectively defined as:

$$a' = \omega/(2\Omega) \quad (2.8)$$

$$\lambda_r(r) = \Omega r/U_\infty \quad (2.9)$$

$$\lambda = \Omega R/U_\infty \quad (2.10)$$

Now that torque and tangential forces are introduced, applying conservation of angular momentum to the flow encapsulated by the stream-tube and integrating the

power produced by the infinitesimal annular rings from root to tip yields:

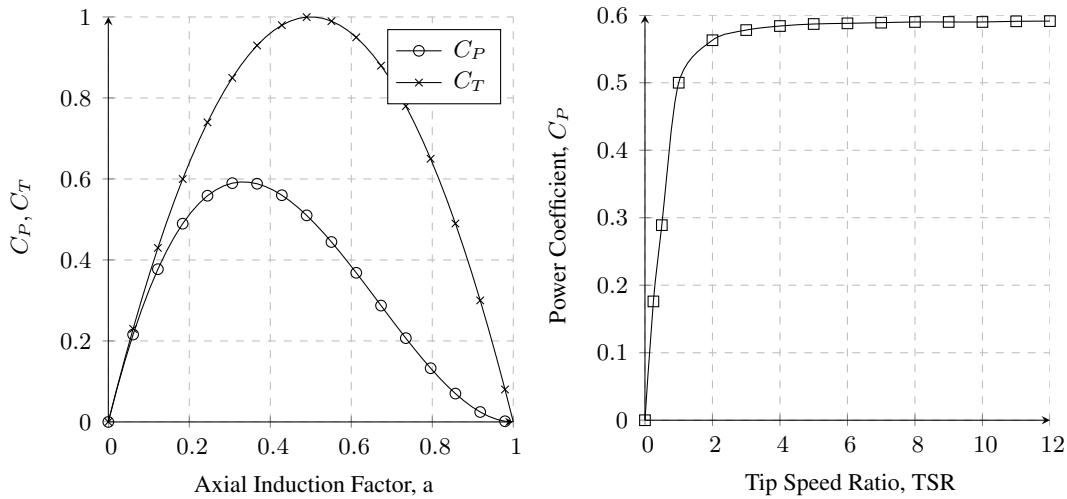
$$C_p = \frac{8}{\lambda^2} \int_{\lambda_{root}}^{\lambda} a'(1-a)\lambda_r^3 d\lambda_r \quad (2.11)$$

Induced tangential velocity (ω) is perpendicular to the relative velocity (and thus parallel to the lift force), hence the following equation can be obtained;

$$\lambda_r^2 = \frac{a(1-a)}{a'(1+a')} \quad (2.12)$$

Maximum power requires local optimization of the integrand of Eq. 2.11 since axial and tangential induction factors are not independent of each other. Optimal relation between tangential and axial induction factors can be found as:

$$a' = \frac{1-3a}{4a-1} \quad (2.13)$$



(a) 1D Momentum Theory

(b) Generalized Momentum Theory

Figure 2.2: Relation of C_p with axial induction factor in no rotation case (a) and with TSR in case with wake rotation (b).

Tabulating a , a' and λ_r makes numerical integration of Eq. 2.11 possible. Plotted curve shows C_p variation with local speed ratio (Fig. 2.2). This result shows that larger the tip speed ratio, higher the power output of an ideal rotating turbine. At low tip speed ratios, loss caused by rotation becomes significant. On the other hand, power gain becomes diminished past $\lambda_r \approx 7$ and asymptotically reaches the terminal value of $C_p = 16/27$ (the Betz limit) at $\lambda = \infty$.

2.2 Blade Element-Momentum Theory (BEM)

Generalized Momentum Theory provides an insight for a theoretical disk with optimal induction factors but does not involve characteristics of the turbine; such as blade geometry (twist and taper), number of blades and airfoil properties. Developed by Glauert in 1935 [41], BEM is a simple yet powerful approach to model a rotor, which is still widely in use today. ALM inherits its main concept from BEM, hence it provides comparable results to verify ALM solutions.

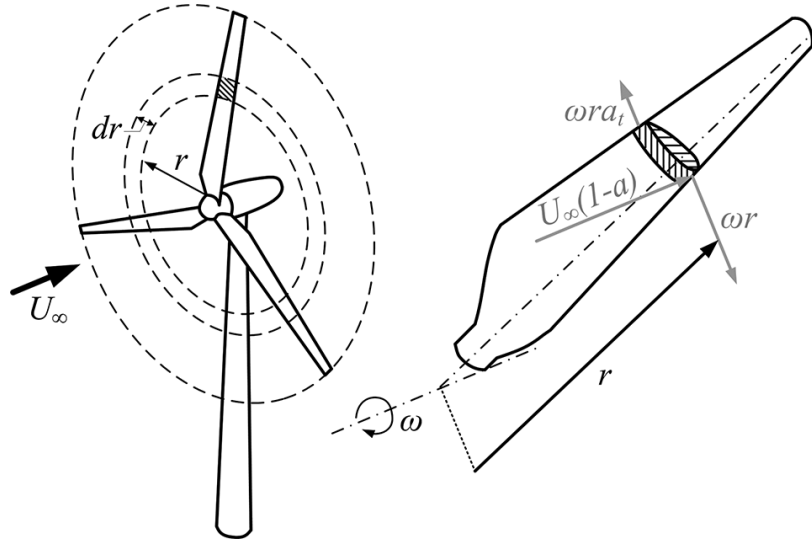


Figure 2.3: Differential annular element used in BEM calculations (Source: [5])

Using axial and tangential induction factor definitions, torque and thrust created by a differential element are found as;

$$dQ = \rho U_{\infty} \Omega 4\pi r^3 (1-a) a' dr \quad (2.14)$$

$$dT = \rho U_{\infty}^2 4\pi r (1-a) a dr \quad (2.15)$$

Differential torque (dQ) and thrust (dT) are calculated using 2D airfoil theory. Sectional lift and drag in chord reference frame are given as:

$$L' = \frac{1}{2} \rho U_{rel} C_l c \quad (2.16)$$

$$D' = \frac{1}{2} \rho U_{rel} C_d c \quad (2.17)$$

Converting sectional lift and drag into rotor coordinate system gives sectional axial

and tangential forces respectively;

$$F'_a = L' \cos \phi + D' \sin \phi \quad (2.18)$$

$$F'_t = L' \sin \phi - D' \cos \phi \quad (2.19)$$

Similar to lift and drag coefficients, axial and tangential force coefficients can be defined by normalizing relevant forces by $0.5\rho U_{rel}c$:

$$C_a = \frac{F'_a}{0.5\rho U_{rel}c} = C_l \cos \phi + C_d \sin \phi \quad (2.20)$$

$$C_t = \frac{F'_t}{0.5\rho U_{rel}c} = C_l \sin \phi - C_d \cos \phi \quad (2.21)$$

Using axial and tangential force coefficient definitions in respective sectional force equations and geometrical relations (Fig. 2.9), differential torque and thrust can be calculated as:

$$dQ = r N_B F'_t dr = 0.5\rho N_B \frac{U_\infty(1-a)\Omega r(1+a')}{\sin \phi \cos \phi} C_t r c dr \quad (2.22)$$

$$dT = N_B F'_a dr = 0.5\rho N_B \frac{U_\infty^2(1-a)^2}{\sin^2 \phi} C_a c dr \quad (2.23)$$

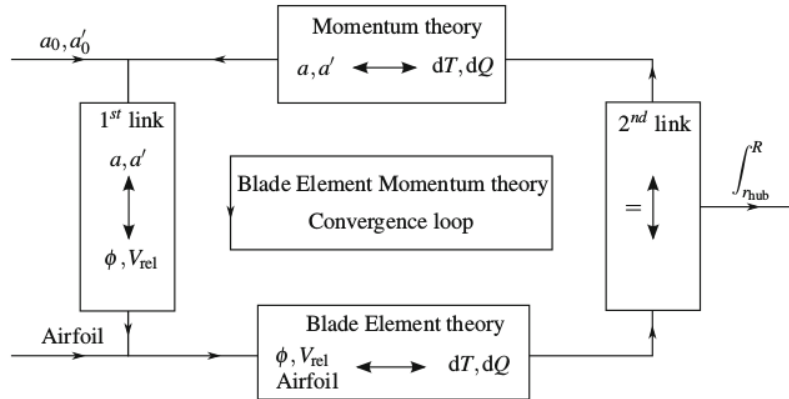


Figure 2.4: Solution loop of BEM as a combination of Momentum and Blade Element Theories
(Source: [6])

Span-wise continuous integration of Eq. 2.22 and 2.23 are often not possible since key parameters that effect lift and drag forces (relative velocity, chord and lift coefficient) vary along span and they almost always can not be represented as a continuous function of radial position. Hence, blades are divided into (preferably small) elements and a discrete summation is performed instead, which is also inevitable in ALM due to nature of the model.

Results in this study are often compared against BEM solutions, which are obtained by QBlade, an open source BEM solver developed by Marten et al. [76].

2.3 2D Airfoil Calculations: XFOIL

Both ALM and BEM rely on pre-calculated C_l C_d data which can be obtained via experiments or CFD solutions. Another popular option is integral boundary layer based panel methods. They have been the primary method used for 2D airfoil computations among researchers for years despite the advances in CFD, thanks to its high fidelity results with considerably low computation cost.

XFOIL is an integral boundary layer code developed by Drela in 1989 [75], still widely used in airfoil design and prediction. XFOIL employs a viscous-inviscid interaction method, where highly viscous boundary layer and almost inviscid outer flow field are handled separately. Potential flow assumption is made outside the boundary layer and flow is solved using panel methods. Airfoil surface is composed of vorticity and source sheets, wake line is modeled with only source sheets and Kutta condition is applied on the trailing edge. Flow within the boundary layer is calculated by numerical integral method, where conservation equations are converted into ordinary differential equations.

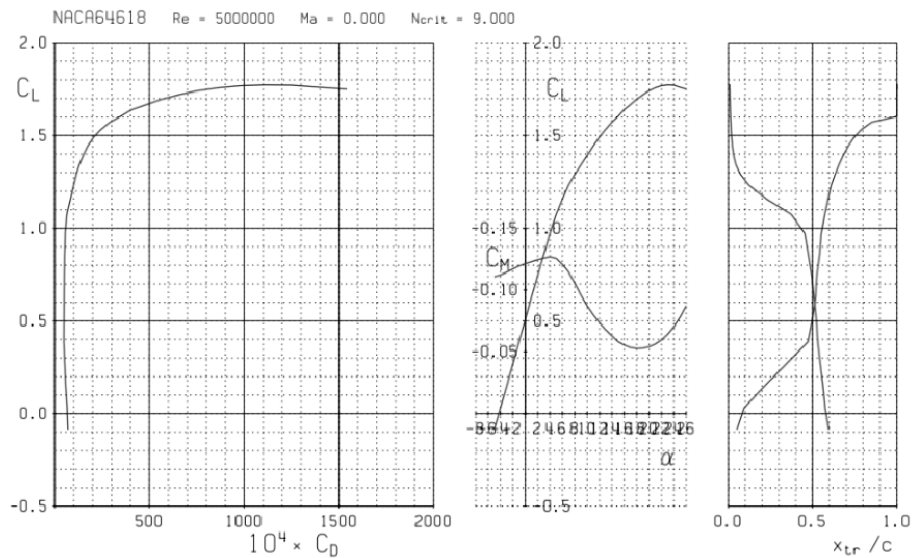


Figure 2.5: A sample XFOIL solution of NACA64-618 airfoil at $Re=5M$

Aerodynamic coefficients vary significantly with Reynolds number. Since Reynolds number is a function of chord and relative velocity, it is different for each actuator point. Its distribution also varies with operation conditions, such as TSR and free stream velocity. Thus, C_l C_d tables are generated for a range of Reynolds numbers and instantaneous Reynolds number at an actuator point is interpolated from available data. On the NREL 5MW wind turbine blade, Reynolds number ranges roughly between 40,000 and 28,000,000 for its normal operation conditions. Thus, airfoil data is generated for 17 Reynolds numbers within this interval. On the other hand, angle of attack range is between -10° and 35° . Although relative angle on NREL 5MW sections ranges within $\alpha = 0^\circ$ and 10° in optimal operating conditions, the margin is necessary to stay on the safe side especially during initial steps of the simulation where angles of attack along blade sections are high due to non-converged flow field.

In terms of XFOIL's simulation parameters, free transition model is employed and standard $N_{crit} = 9$ value is used for turbulence level control.

2.4 Tip Loss Correction

Tip loss correction was conceptualized by Prandtl [78] to facilitate the turbine wake by modeling helical patterns in the wake as vortex sheets. His model was directed towards BEM by adjusting the momentum equations. Tip loss factor is defined as:

$$F_{loss} = \frac{2}{\pi} \cos^{-1} \left(\exp\left(-\frac{N_B(R-r)}{2r \sin \phi}\right) \right) \quad (2.24)$$

Tip loss factor F_{loss} is applied to the forces acting on blades by directly multiplying differential torque (Eq. 2.14). The factor has little to no effect in the mid-span region and gradually reduces the lift force towards the tip. This resembles a fully resolved blade where lift is zero at the tip due to pressure leakage that generate tip vortices.

However, Prandtl's assumption of wake being confined instead of expanding has put a limitation on its use. Additionally, in cases where TSR and axial induction factor are high (approximately $a > 0.4$), discrepancies in BEM becomes apparent. Glauert [79] approached this limitation by correcting the thrust coefficient by fitting a curve to empirical data (Fig. 2.6). This improvement was also applicable to BEM by providing each blade element a correction coefficient as a function of span-wise location.

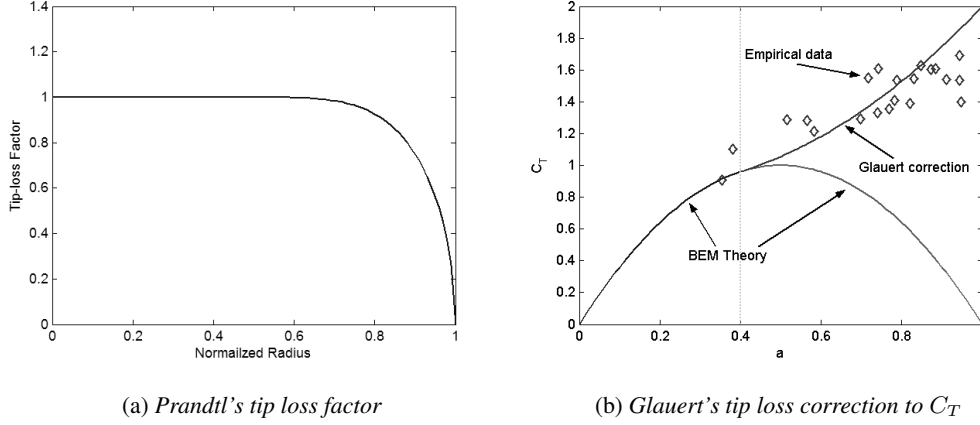


Figure 2.6: Tip loss factor in accordance with empirical data (Source: [7])

There are other functions available for tip loss correction; namely Wilson & Lissaman [80] and de Vries [81]. In their recent study, Shen et al. [82] did further corrections to Glauert's tip loss equation to include 3D tip loss effects, multiplying the exponent as such:

$$F_{loss} = \frac{2}{\pi} \cos^{-1} \left(\exp \left(-g \frac{N_B (R - r)}{2r \sin \phi} \right) \right) \quad (2.25)$$

where g is given as;

$$g = \exp(-c_1(N_B \lambda - c_2)) + 0.1 \quad (2.26)$$

and $c_1 = 0.125$, $c_2 = 21$ constants are acquired from measurements. Shen's model reduces to Glauert's function when $g = 1$. It is concluded that the new correction method is applicable for a wider range of tip speed ratios and in better agreement with measurements. In this study, Shen's tip correction function is used. Also, the loss factor is applied to root in addition to the tip, since the hub is not modeled. A resultant distribution of tip loss factor is given in Fig. 2.7, where both tip and root are affected.

2.5 Flow Solutions with OpenFOAM

Specifically for NREL 5MW wind turbine, it has been shown that compressibility effects can be neglected up to $TSR = 10$ [83]. This can be justified by the fact that blade tip Mach number is $M_{tip} = 0.23$ at rated conditions ($U_\infty = 11.4m/s$ and $TSR = 7$). Free stream velocity does not exceed the rated value throughout this thesis, but maximum simulated tip speed ratio is $TSR = 10$. Even under this

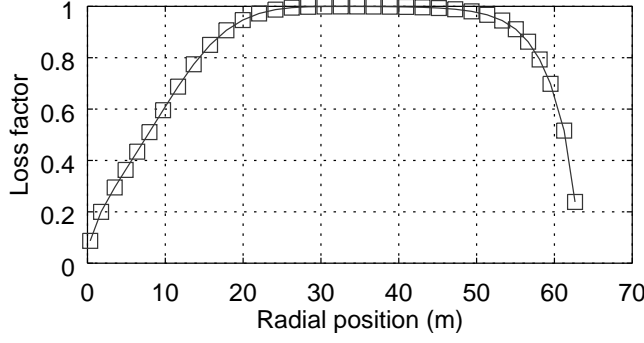


Figure 2.7: An example of calculated tip loss factor distribution in simulations.

conditions, $M_{tip} = 0.33$, barely exceeding the commonly accepted compressibility limit of $M_{max} = 0.30$. Hence, incompressible fluid assumption is found to be adequate for all simulations.

Incompressible flow of a Stokesian fluid is governed by conservation of mass and momentum equations, given as:

$$\nabla \cdot \mathbf{u} = 0 \quad (2.27)$$

$$\frac{\partial \mathbf{u}}{\partial t} + \nabla \cdot (\mathbf{u}\mathbf{u}) = -\nabla p + \nabla \cdot (2\nu\mathbf{S}) + \mathbf{f} \quad (2.28)$$

equivalently in tensorial form:

$$\frac{\partial u_i}{\partial x_i} = 0 \quad (2.29)$$

$$\frac{\partial u_i}{\partial t} + \frac{\partial}{\partial x_j} (u_j u_i) = -\frac{\partial p}{\partial x_i} + \frac{\partial}{\partial x_j} (2\nu S_{ij}) + f_i \quad (2.30)$$

where $\mathbf{u} = u_i$ is the velocity vector, $\mathbf{f} = f_i$ denotes the body force vector and

$$\mathbf{S} = S_{ij} = \frac{1}{2} \left(\frac{\partial u_i}{\partial x_j} + \frac{\partial u_j}{\partial x_i} \right) \quad (2.31)$$

is the rate of strain tensor. An important parameter at this point is body force \mathbf{f} , which is the term used to pass the calculated blade forces into the solution domain (see Sec.

2.6). By applying continuity equation, conservation of momentum equation can be rewritten in differential and tensorial forms respectively as:

$$\frac{\partial \mathbf{u}}{\partial t} + \mathbf{u} \cdot \nabla \mathbf{u} = -\nabla p + \nu \nabla^2 \mathbf{u} + \mathbf{f} \quad (2.32)$$

$$\frac{\partial u_i}{\partial t} + u_j \frac{\partial u_i}{\partial x_j} = -\frac{\partial p}{\partial x_i} + \nu \frac{\partial^2 u_i}{\partial x_i \partial x_j} + f_i \quad (2.33)$$

It should be noted that p represents not the dynamic pressure, but rather *reduced pressure* (i.e. pressure per density) in these equations. These are the incompressible Navier-Stokes equations and is capable of handling turbulence, but only on a grid that is extraordinarily fine to capture all scales of eddies. That is called Direct Numerical Simulation (DNS) and is extremely expensive to compute, hence turbulence is incorporated through some assumptions and simplifications. Two of the most common approaches in modern CFD are:

- RANS: where all turbulent eddy scales are modeled,
- LES: where small eddies are still modeled and large-scale eddies are resolved via a filtering process.

2^{nd} order unbounded upwind scheme is used in divergence and gradient terms. Transient, 1^{st} order implicit and bounded Euler scheme is used in time derivative terms. LES is employed for turbulence modeling.

2.5.1 Large Eddy Simulation (LES) Equations

Applying a spatial low-pass filter to general Navier-Stokes equations yield the LES equations in differential form:

$$\widetilde{\nabla \cdot \mathbf{u}} = 0 \quad (2.34)$$

$$\frac{\partial}{\partial t} \widetilde{\mathbf{u}} + \widetilde{\mathbf{u} \cdot \nabla \mathbf{u}} = -\nabla \widetilde{p} + \nu \nabla^2 \widetilde{\mathbf{u}} + \widetilde{\mathbf{f}}_b \quad (2.35)$$

OpenFOAM employs a so called top-hat filter method, where volume average of physical quantities are filtered. In this method, filtering is not a function of spatial coordinates, hence, due to the homogeneity property, incompressible continuity is valid also as $\nabla \cdot \tilde{\mathbf{u}} = 0$. Using this property, nonlinear term in filtered momentum equation can be written as:

$$\widetilde{\mathbf{u}\nabla\mathbf{u}} = \tilde{\mathbf{u}}\nabla\tilde{\mathbf{u}} + \nabla \cdot \tau \quad (2.36)$$

$$\tau_{ij} = \widetilde{u_i u_j} - \tilde{u}_i \tilde{u}_j \quad (2.37)$$

Here, τ_{ij} tensor denotes the sub-grid scale (SGS) stress (or residual stress). Isotropic part of the SGS stress can be combined with the filtered pressure term, however, the remaining deviatoric part should be modeled in terms of velocity $\tilde{\mathbf{u}}$ and pressure \tilde{p} . In the homogeneous filtering case, filtered Navier-Stokes equations can be written as:

$$\widetilde{\nabla \cdot \mathbf{u}} = 0 \quad (2.38)$$

$$\frac{\partial}{\partial t} \tilde{\mathbf{u}} + \widetilde{\mathbf{u} \cdot \nabla \mathbf{u}} = -\nabla \tilde{p} + \nu \nabla^2 \tilde{\mathbf{u}} - \nabla \cdot \tau^d + \tilde{f}_b \quad (2.39)$$

$$\tau_{ij}^d = \tau_{ij} - \frac{1}{3} \delta_{ij} \tau_{kk} \quad (2.40)$$

Here, τ_{ij}^d is the remaining deviatoric component of the SGS stress tensor. To obtain closure, it is expressed in terms of filtered velocity $\tilde{\mathbf{u}}$ and pressure \tilde{p} . This procedure is called *SGS modeling* and there are several approaches available in the literature. One of the earliest and still popular methods to relate τ to \mathbf{u} was proposed by Smagorinsky in 1963 [84] as the following:

$$\tau_{ij}^d = -2\nu_{SGS} S_{ij} \quad (2.41)$$

$$\nu_{SGS} = (C_S \Delta)^2 \|S\| \quad (2.42)$$

$$S = \frac{1}{2} (\tilde{u}_{j,i} + \tilde{u}_{i,j}) \quad (2.43)$$

$$\|S\| = (2S_{ij}S_{ij})^{(1/2)} \quad (2.44)$$

where ν_{SGS} is the sub-grid scale viscosity, S is the rate of strain tensor and C_S is the model constant. Δ is taken as the cube root of cell dimensions in all directions, i.e. $\Delta = (\Delta_x \Delta_y \Delta_z)^{1/3}$. In simulations where turbulence is dominantly isotropic, suggested C_S value is 0.168. However, C_S should be reduced closer to walls. $C_S \Delta$ term denotes sub-grid length scale and it is assumed constant in the classical Smagorinsky SGS model, which causes high dissipation at near wall regions. This is one of the major drawbacks of this model, but still useful and easy to implement in isolated rotor studies where boundary effects are not resolved.

2.5.2 Flow Solver: pimpleFoam

OpenFOAM's transient solver for incompressible fluids; `pimpleFoam` is used to solve the given equations. It employs a combination of SIMPLE (Semi-Implicit Method for Pressure-Linked Equations) and PISO (Pressure Implicit with Splitting of Operator) algorithms [85]. SIMPLE is essentially an algorithm developed for steady-state flows. In `pimpleFoam`, SIMPLE algorithm is applied (pressure-velocity coupling is solved via iterations and under-relaxation) for a single time step, and then solution moves on to the next time step upon convergence. The total number of SIMPLE applications is controlled by `nOuterIterations` parameter, or by a residual control. That is, if `nOuterIterations` is set to 1, PIMPLE solver reduces to the basic PISO algorithm.

Gaussian integration is used for finite volume integration, where values on cell faces are interpolated from cell centers and then summed up. Second order central differencing is used for interpolation. Convective fluxes are computed using second order upwind differencing. First order implicit Euler method is employed for time discretization.

Depending on the residual control setting, required number outer correction loops for convergence is between 3 and 5 in this study.

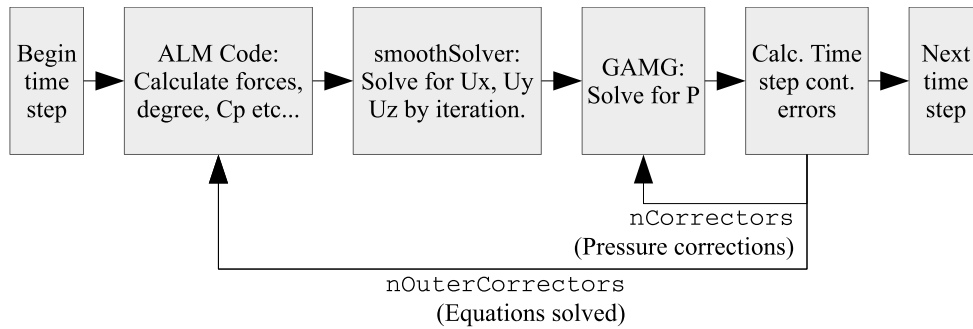


Figure 2.8: Flow chart showing the PIMPLE loop within a single time step

2.6 Actuator Line Model (ALM)

In a conventional CFD simulation, blades are introduced into the solution domain as solid entities and certain boundary conditions are applied on the surfaces, such as no-slip BC for velocity and wall functions for turbulence. This approach requires the blade boundary layer to be fully resolved, hence a large number of cells in the mesh, especially considering the geometry is 3D. On the other hand, wind turbine simulations are unsteady due to rotation, if no simplifications are done. There are several approaches available for simulations of rotary geometries; such as Sliding Mesh Interface (SMI) where different regions in the mesh physically moves and special treatment is applied to mesh boundaries that are sliding on each other, or Multi Reference Frame (MRF) where the whole domain is geometrically stationary but relative movement of different zones are modeled by additional terms in the conservation equations. Another often used simplification is to use an axisymmetric domain and applying cyclic boundary conditions to the azimuthal slices. Grid size is reduced to $(1/N_B)^{th}$ in this approach, where N_B is the number of blades. It is feasible to study a single isolated wind turbine, however due to its axisymmetric assumption, it is not applicable for full scale wind farm simulations or combination with terrain modeling.

Actuator Line Model is based on the idea of representing wind turbine blades as *virtual* lines instead of fully resolved solid geometries. Using a BEM-like approach, lines are divided into a finite number of sections. Each section is represented by an *actuator point* in the domain. In an FRM, blade loadings and flow field are obtained primarily from 3D pressure distribution calculated over blade surfaces. In ALM,

this is replaced by calculating forces for each actuator point in a more simplified way externally and passing it to the domain as body forces; no physical surfaces or boundary conditions exist for turbine representation.

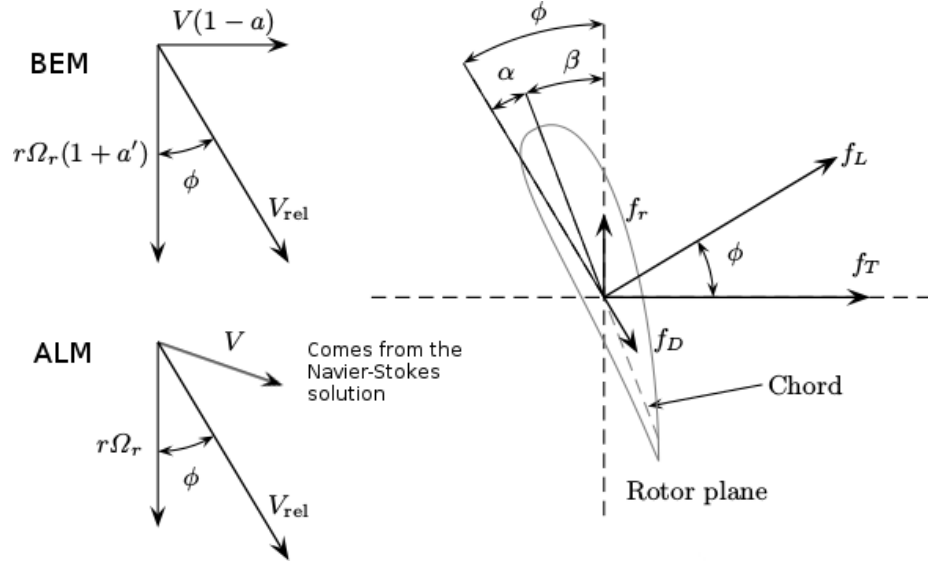


Figure 2.9: Relative velocity, angle definitions and forces acting on a blade section in BEM and ALM approaches. (Original image: [8])

Sectional lift and drag forces are calculated using 2D airfoil theory for each actuator point, converted into rotor coordinate system;

$$L = \frac{1}{2} \rho U_{rel}^2 C_l c \Delta_{AP} \quad (2.45)$$

$$D = \frac{1}{2} \rho U_{rel}^2 C_d c \Delta_{AP} \quad (2.46)$$

$$f_a = L \cos \phi + D \sin \phi \quad (2.47)$$

$$f_t = L \sin \phi - D \cos \phi \quad (2.48)$$

$$\mathbf{f}_R = \mathbf{f}_a + \mathbf{f}_t \quad (2.49)$$

Here, \mathbf{f}_R is the 2D force vector, which is then multiplied by the element width and becomes the 3D force vector to be passed into the solution domain via \mathbf{f} term given in Eq. 2.32. Force coefficients (c_l, c_d) are obtained from pre-calculated airfoil data, tabulated as a function of angle of attack α and Reynolds number Re . Local Reynolds number is calculated as:

$$Re = \frac{\rho U_{rel} c}{\mu} \quad (2.50)$$

Hence, values to be determined here are angle of attack α and relative velocity U_{rel} . In BEM, they are obtained by iterating on axial and tangential induction factors. In contrary, ALM uses the velocity vector components that are computed by the Navier-Stokes solution and uses them instead of the induction factors; in other words, induced velocity effects are handled by the Navier-Stokes solution in ALM. Turbine's rotation speed is assumed to be constant and controlled by an ideal generator, hence rotor's inertial effects or variations in the blade loadings have no role in instantaneous angular velocity. This is an important assumption made in this study which simplifies calculations. Rotor's and each blade's orientation vectors are also calculated for each time step. Then, calculated f_a and f_t are converted into absolute coordinate system components (f_x, f_y, f_z) and reflected into the solution grid. These forces cause the flow field to be deflected, changing the velocity field; variations in the velocity field dictates α and U_{rel} values monitored in the domain. Hence force and velocity fields are strongly coupled in an ALM solution and results are very sensitive to this coupling. In this procedure, two steps have a major impact on results:

- **Velocity sampling:** Where and how to monitor α and U_{rel} in the domain?
- **Force projection:** How to pass calculated forces into the solution domain?

These questions still does not have well established answers in the literature that are applicable to every problem and remains an ambiguous zone in ALM to this date. Actually, these are the primary steps which directly determines how aforementioned force-velocity coupling should be solved. Hence, a large portion of this thesis involves examination of parameters related to these steps.

2.6.1 Velocity Sampling

In the rotor coordinate system, relative velocity at each actuator point can be separated into two components: tangential (on the rotor plane) and axial (normal to rotor plane).

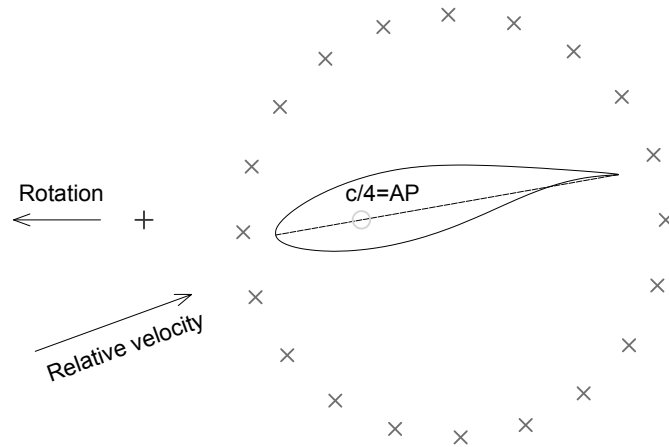


Figure 2.10: Various velocity sampling techniques: upstream monitoring (+), line averaging (x) and monitoring on the actuator point (o)

In ALM, no special rotation or movement techniques -such as SMI or MRF- are employed; instead, actuator lines are moved according to time step size and angular velocity of the rotor and coordinates of each actuator point are calculated for each time step. Thus, no effects are present to manipulate the velocity field such that tangential components due to rotation are generated. In the ALM code, this is handled by combining two results: linear velocity due to rotation, calculated for each actuator point using the simple $U_{linear} = \omega r$ formula and velocity component in the same direction that is monitored from the flow field are summed up. Resultant value forms the tangential velocity, U_t . On the other hand, axial velocity U_a is strongly affected by the presence of rotor and generated forces, already slowed down along blades. It is directly read from the domain and used. It should be noted that magnitude of tangential velocity component is considerably higher than that of axial velocity component.

A force applied in the flow field results in circulation due to Kutta-Joukowski theorem. This circulation causes downwash and upwash in the trailing and leading edge regions, respectively. A good velocity sampling should be free of such effects, whereas axial induction must still be felt by the blade elements since that is the actual free stream for them. One reasonable approach to this problem is to use points directly on the actuator lines, which corresponds to the center of bound vorticity where such effects are felt minimally. Martinez-Tossas et.al [10] had results

in support of this idea in their studies, but also suggested corrections for cases where drag is high. However, in the computations where c_l c_d tables are obtained, Reynolds number and angle of attack definitions are based on the free stream, which is very far away from and undisturbed by the airfoil. Based on this idea, Shen et al. [86] performed the sampling at a distance upstream of blade element leading edge to capture a more accurate free stream velocity vector while being away from blade-local flow effects. However, it was found that such approach is highly sensitive to selected location and in cases with high turbulent inflows (i.e blades experiencing wake caused by upstream turbines) sampled velocity is affected by turbulent structures before blades actually encounter them. On the other hand, Sreenivas et al. [87] has used an average of 7 to 21 closest cells as the monitored velocity. Although this technique yielded better power predictions, authors have concluded that the improvement was small and the primary issue with ALM was still mesh dependency.

In this thesis, velocity is sampled precisely on the quarter chord point (which also serves as the actuator point) due to its simplicity and common usage in literature. Since a cell center and actuator point does not usually coincide during rotation, velocity components are linearly interpolated from the velocity field to the actuator point.

2.6.2 Force Projection

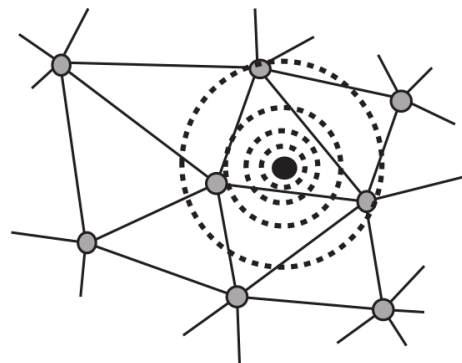


Figure 2.11: *Projection of computed force to cells in vicinity, as a function of distance. (Source: [9])*

After the resultant force is calculated for a blade section, it is passed into the solution

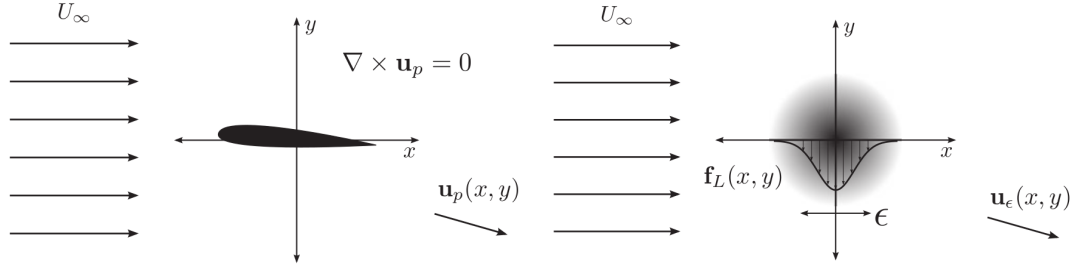


Figure 2.12: Resemblance of pressure field past an airfoil via distributed point force (Source: [10])

domain as an addition to the body force term \mathbf{f} in the momentum equation (Eq. 2.28) which creates a new variable in the domain: force field. Simplest idea would be to pass the resultant force to the nearest cell center, but this causes singular behavior and highly unstable and oscillatory flow near actuator points. On the other hand, ultimate goal in ALM is to resemble the pressure field generated over a real blade surface as close as possible, which is smooth along the span. Starting from the introduction of ALM by Shen et al., these issues were handled by *smearing* calculated forces among cells that are in the vicinity of each actuator point. Most widely employed method is to distribute each force in the form of 3D normal (Gaussian) distribution; such that force to be imposed at a cell center is inversely proportional with its distance to actuator point, and the sum of forces at cell centers would be equal to the calculated singular force. 3D Gaussian kernel function is given by:

$$\eta = \frac{1}{\epsilon^3 \pi^{3/2}} \exp\left(-\left(\frac{|\mathbf{r}|}{\epsilon}\right)^2\right) \quad (2.51)$$

where \mathbf{r} is the distance from actuator point and ϵ is a parameter which controls the width of Gaussian kernel; higher the ϵ , wider region the force is smeared to. Initial intuition is to take the chord as reference length. Instead of distributing forces spherically using a single radius in all directions, Sreenivas et al. [87] defined two projection widths to form an ellipsoidal smearing shape. This enabled them to take both chord and element size as reference lengths in force projection, achieving a better resemblance with pressure distribution.

In this study, Gaussian distribution is done isotropically, i.e. a virtual sphere is determined around each actuator point and force to be added to each cell center \mathbf{f}

is calculated as the convolution of resultant force and Gaussian kernel, $\mathbf{f} = \mathbf{f}_R \otimes \eta$. This guarantees the sum of cell-center forces to be equal to singular force and is useful especially on grids where cells in the rotor plane are non-uniform.

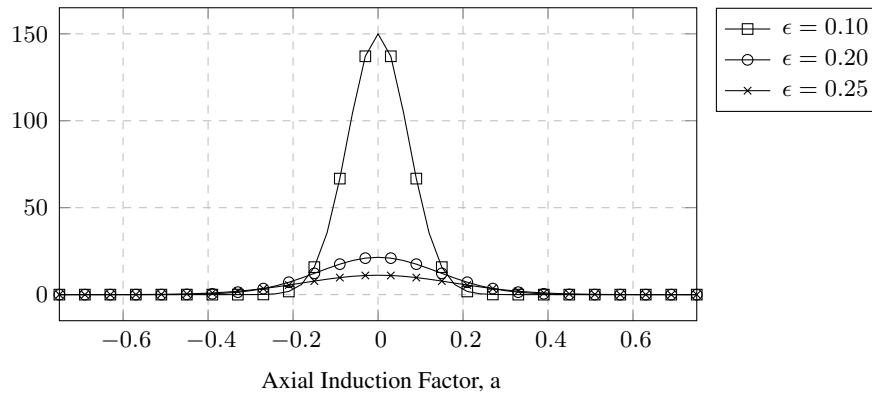


Figure 2.13: Comparison of various ϵ parameters in Gaussian function.

A single and universal value for ϵ to fit every case could not be determined in the literature. Moreover, seeing different ϵ suggestions for similar conditions in various studies is quite common. Projection width is still one of the most ambiguous parameters in ALM. Also, solution is highly sensitive to the projection width. This can be observed in Fig. 2.13, where a representative 1 unit of force is distributed in 3 dimensions among 31 cells within $[-1, 1]$ interval using Eq. 2.51 and cell center values are plotted along the mid-line. Cell volume is 2.9630×10^{-4} units in this case. Doubling ϵ from 0.1 to 0.2 causes the overall profile to change dramatically, increasing the value from 18 to 74 for the cell located at the sphere center (which will also be the actuator point in ALM). Considering that the velocity field is deflected and shaped by these forces, it would be reasonable to expect a big difference between monitored angle of attacks for these ϵ values.

2.6.3 ALM Implementation in OpenFOAM: turbinesFoam

The code developed by Bachant et al. [74] was primarily used to implement ALM in OpenFOAM. The ALM code becomes operational at the beginning of the time step. Forces are calculated on actuator points based on the velocity field that is computed in the previous time step. Now that forces are reflected to the domain, momentum matrix is constructed with body force term present. PIMPLE algorithm's pressure correction

takes place afterwards, which constitutes the inner loop and can be iterated on as many times as wished. This whole procedure happens within the outer corrector loop of `pimpleFoam`. Iterating on outer loop re-constructs the momentum matrix, hence it is crucial in solving for the force-velocity coupling and achieving convergence within a single time step.

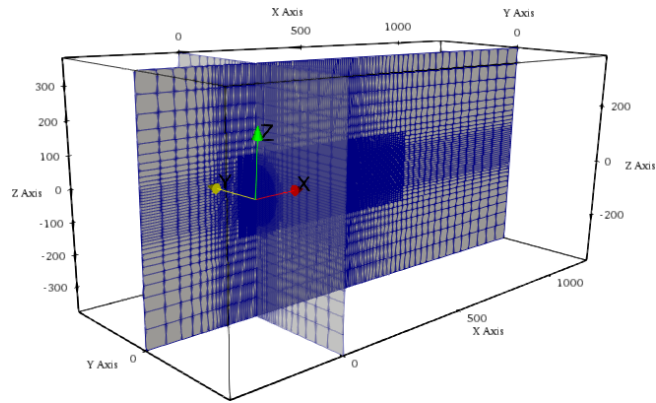
2.7 Computational Grid

Solution domains in this study are discretized into uniform Cartesian hexahedral cells. Mesh consists of regions with different refinement levels. Cell size is the largest at outermost regions (far-field) and gets gradually refined towards rotor zones. Refinement is done by a simple halving method; size is halved at each successive level. Triangulated cells are generated in transition layers, hence not the whole domain is composed of hexahedral cells, but number of these tetrahedral cells are very few in number. This way, 90° orthogonality and zero skewness were achieved throughout the domain. Typical cell sizes are $63m$ at the far-field and $0.5 - 1m$ at the rotor plane, obtained through 5 to 6 refinement zones.

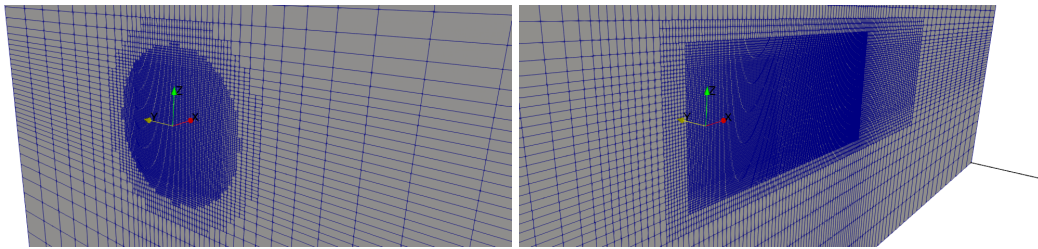
Refinement levels are designated in various configurations:

- Rotor zone only: for cases which the scope does not include the wake region (such as computed blade loadings).
- Rotor and wake zones: for cases which points of interest are turbulent structures and velocity profiles in the wake region.
- Rotor zones of two turbines and the wake region between: for the case where wake interaction between two turbines and impingement of the wake generated by upstream turbine is wanted to be captured.

This distinction was necessary because of the computational limitations. It is common that number of cells is typically more than the order of 10^7 in similar LES of atmospheric flows. However, number of cells is tried to be kept under 5M for the majority of simulations.



(a) 3D view with slices through x and y planes.



(b) Close-up view of refinement zones on x-plane (left) and y-plane (right) slices.

Figure 2.14: Discretized solution domain for an isolated rotor simulation. Resolution at rotor plane is $\Delta_g/R = 1/32$.

OpenFOAM's built-in mesh modules `blockMesh` and `snappyHexMesh` were used for generation and manipulation of grids. Refinement levels are defined in the shape of cylinders. Refinement zone for the rotor is typically defined as a cylinder that is extruded by a margin of $0.5D$ in all directions from the rotor swept disk. For wake zone, this refined region is extended by a distance of $5D \sim 10D$ towards downstream, according to the post-processing needs. In dual turbines case, rotor refinement level is extended up to downstream turbine, and some more ($\sim 3.5D$) afterwards. Domain extends are typically $-3D$ to $3D$ in lateral (y and z) directions and $-3D$ to $10D$ in

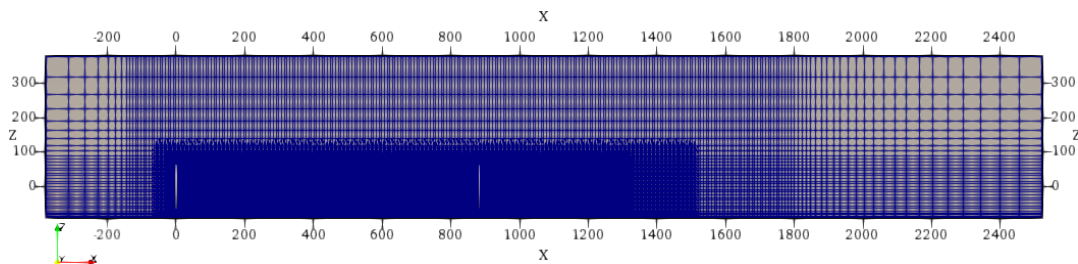


Figure 2.15: Mid-y-plane sliced view of the mesh used in ABL flow simulations.

flow (x) direction. It should be noted that these values are not kept constant always and prone to slight changes according to specific conditions of each case. With a grid resolution of $\Delta_g/R = 1/32$, grid sizes are approximately 820K and 6M for single and dual wind turbine cases, respectively.

Applied boundary conditions are given in Tables 2.1 and 2.2 for isolated turbine and sheared flow cases, respectively. Main differences are at the inlet and ground boundaries.

Table 2.1: *Boundary conditions in the isolated turbine case (ZG: zero gradient, Calc.: calculated, ABL: atmospheric boundary layer)*

	Inlet	Outlet	Sides&Top	Bottom
U	Uniform	ZG	ZG	ZG
p	ZG	0	0	0
ν_{SGS}	ZG	ZG	Calc.	Calc.

Table 2.2: *Boundary conditions in the sheared flow case*

	Inlet	Outlet	Sides&Top	Bottom
U	ABL	ZG	ZG	0
p	ZG	0	0	ZG
ν_{SGS}	ZG	ZG	Calc.	ZG

CHAPTER 3

RESULTS AND DISCUSSION

The root idea of using ALM in this study is to represent wind turbine rotors in the blade chord length scale, with enough discretization resolution to generate accurate wake structures while being computationally inexpensive, and eventually run full wind farm simulations. For this purpose, conducted study and presented results are divided into two main sections: (1) assessment of optimum simulation parameters, (2) simulation of wake interaction between two wind turbines in tandem using the simulation parameters found.

Hitherto discussed chapters, there does not exist a certain constant value for most of the key simulation parameters and no methods prove to be suitable for all cases. The first section of this chapter is dedicated to investigation of these simulation parameters with the aim of finding the best performing values to be used in further simulations. Solution of force-velocity coupling and its sensitivity to residual control of PIMPLE loop, temporal and spatial discretization, force projection width and number of actuator points to be experimented with. Later, the best performing parameters are concluded and tested for a range of different TSR values.

In the second section, two in-line wind turbines are simulated using the parameters found in the previous section. The model is tested in configurations with and without ground present, as well as non-yawed and yawed rotors. Results in form of wake interaction and power loss at the downstream turbine are discussed.

Later in this section, parallelization efficiency and speed-up values are also presented.

NREL 5MW wind turbine is used as the test rotor in all simulations [77] and it is simulated in full-scale. It is a 3-bladed horizontal axis wind turbine with $D = 126m$

rotor radius and $90m$ hub height, rated at $U_{ref} = 11.4m/s$ free stream wind speed and tip speed ratio $TSR = 7$ (corresponding to $\Omega = 12.1RPM$ and $U_{tip} = 80m/s$). The blade geometry is defined in 19 sections with 2 circular and 6 airfoil profiles, along which Reynolds number changes between $2M$ and $12M$ at rated conditions (Fig. 3.1). Direction of rotation is positive (CW), assuming the rotor axis coincides with $+x$ axis. Since NREL 5MW is a notional wind turbine, there is no experimental data available in the literature to this day. Therefore, BEM results obtained by QBlade and FRM results presented by Dose et al. [11] are used for validation.

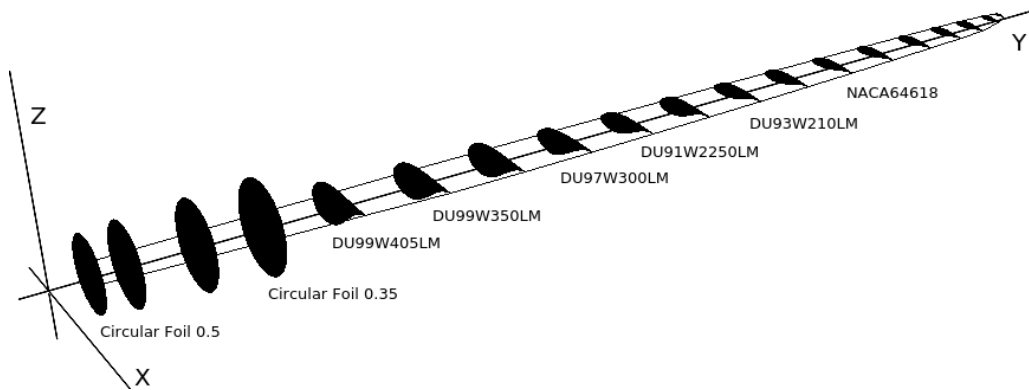


Figure 3.1: Sections of the NREL 5MW wind turbine.

3.1 Assessment of Simulation Parameters on a Single Isolated Turbine

Performance of ALM heavily relies on accurate relative flow estimation; that is, (1) orientation (angle of attack) and (2) magnitude of velocity vectors at actuator points, which are interpolated from the flow field in the vicinity. These two primary variables are very sensitive to the following parameters, which are tested in this section:

1. Number of iterations on force-velocity coupling
2. Time step size, Δ_t
3. Grid resolution at the rotor plane, Δ_g/R
4. Force projection width, ϵ (chord or grid size dependent)
5. Number of actuator points, Δ_{AP}/R

All simulations are run at rated conditions of NREL 5MW turbine ($U_\infty = 11.4m/s$, $TSR = 7$ ($\Omega = 12.1RPM$)) where pitch angle is zero. Rotor is isolated from boundary effects, i.e. it is placed in the span-wise midpoint of the domain. Accuracy is evaluated based on computed angle of attack and tangential force distributions, as well as power the coefficient. Therefore only the rotor region is refined in mesh to save computation time. All presented results are obtained after the turbine reaches a steady C_P value, corresponding to approximately 100 seconds of simulation time (≈ 20 revolutions).

3.1.1 Iterative Solution for Force-Velocity Coupling

Solution of force-velocity coupling has a direct effect on the formation of local flow field, and estimated angle of attack accordingly. ALM code works in the outer corrector loop, right after the time step begins (Fig. 2.8). Each outer correction means a complete reconstruction and solution of momentum equation, which magnifies the overall computational cost. Thus, it is important to find the optimum number of iterations for convergence without excessive computation.

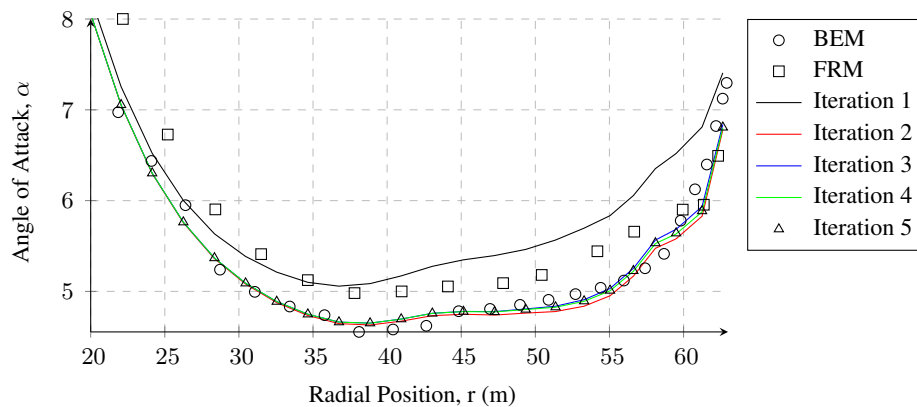


Figure 3.2: Convergence of angle of attack distribution along blade span with PIMPLE iterations (FRM: [11])

Fig. 3.2 shows the convergence of calculated angle of attack and relative velocity magnitude within the first 5 PIMPLE iterations, compared with the BEM solution. Only mid-to-tip region of the blade is zoomed in, which is source of most of the torque generating forces. Residual control is set to 10^{-4} for the current simulation.

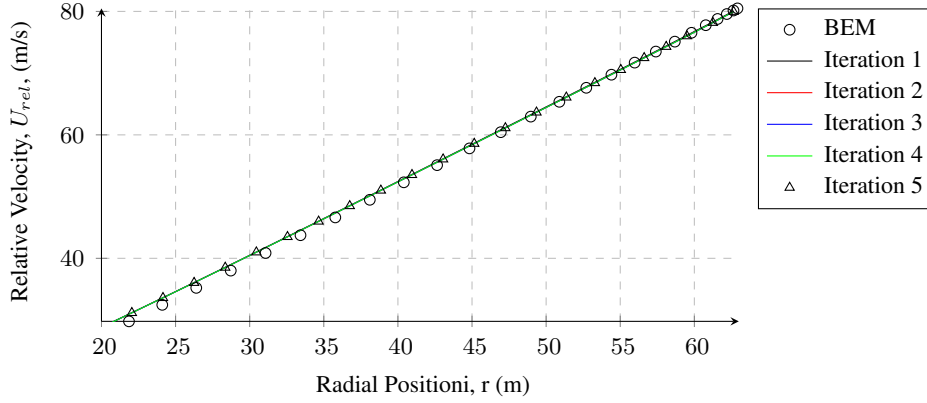


Figure 3.3: Convergence of relative velocity magnitude distribution along blade span with PIMPLE iterations

Angle of attack is significantly over-predicted in the first iteration, showing up to %10 difference towards the tip. Largest correction takes place in the second iteration, yielding an angle of attack distribution very close to the BEM result. Although consecutive iterations provide some further convergence, these acquired gaining diminish after third iteration. Calculated residual at this point is in the order of 10^{-3} , which can be considered for simulations where computational efficiency outweighs accuracy. Under this condition, convergence is achieved after 3 to 4 outer loop iterations in the simulations performed.

In contrast to angle of attack, there is almost no change in velocity magnitude throughout iterations. This observation relates to the velocity sampling method used in the ALM. Analogous to BEM definitions, we can define the components of relative velocity as seen by an actuator point:

- Tangential component $U_t(r) = \Omega r(1 + a')$ in ALM: the linear velocity due to rotation is calculated analytically and the velocity monitored from domain is summed up with. Hence, the tangential induction effect is evaluated from the Navier-Stokes solution.
- Axial component $U_a = U_{ref}(1 - a)$ in ALM: which is solely read from the domain, with induction already included.

Due to the fact that tangential velocity is more than one order of magnitude larger than axial velocity in the majority of blade span, resultant velocity magnitude is dominated

by it. Additionally, the contribution of tangential induction to the resultant tangential velocity is considerably small. This means that along with iterations, changes in the axial velocity component has a significant effect on orientation of the resultant velocity, rather than its magnitude. Despite the small variations in angles in this case ($0.5^\circ - 1^\circ$), the aerodynamic coefficients change rapidly around these angle of attack values ($\partial c_l / \partial \alpha$ is large). It can be said that the calculated forces and coupled velocity field are sensitive to this variation. This experimentation shows that angle of attack prediction is highly sensitive to force-velocity coupling, whereas velocity magnitude is not.

3.1.2 Temporal Discretization

In most of the ALM related studies, it is suggested that the time step size should be constant and chosen such that none of the actuator points travel more than a cell size within a single time step. On grids where cell size is uniform in the rotor plane (as in this study), maximum Δ_t size is limited by the blade tip, where linear speed is maximum. This creates a constraint on the time step size more rigid than the maximum field Courant number, which is defined as $CFL = |\mathbf{U}| \Delta_t / \Delta_g$ and expected to be smaller than 1 (Fig. 3.4). In this regard, a conceptual Courant number is defined in this study to represent its hypothetical CFL condition at the blade tip: $CFL_{tip} = \Delta_t U_{tip} / \Delta_g$.

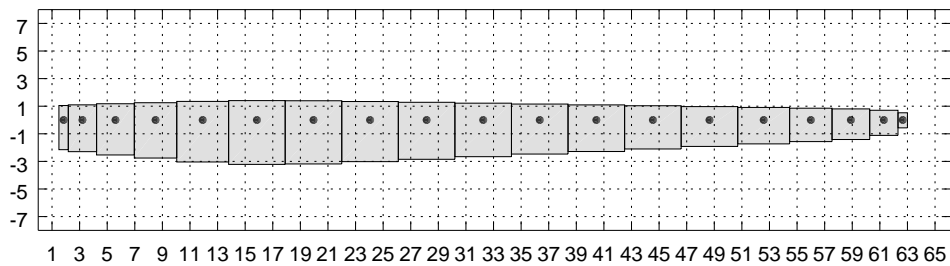


Figure 3.4: Visualization of an Actuator Line that is divided into 19 actuator points on a $\Delta_g/R = 1/32$ solution grid.

Although $CFL_{tip} < 1$ is a widely used and referred rule in literature, it has yet not been justified. In this section, various CFL_{tip} values are tested on a grid with $\Delta_g/R = 1/32$ resolution at the rotor plane. As in the conventional practice,

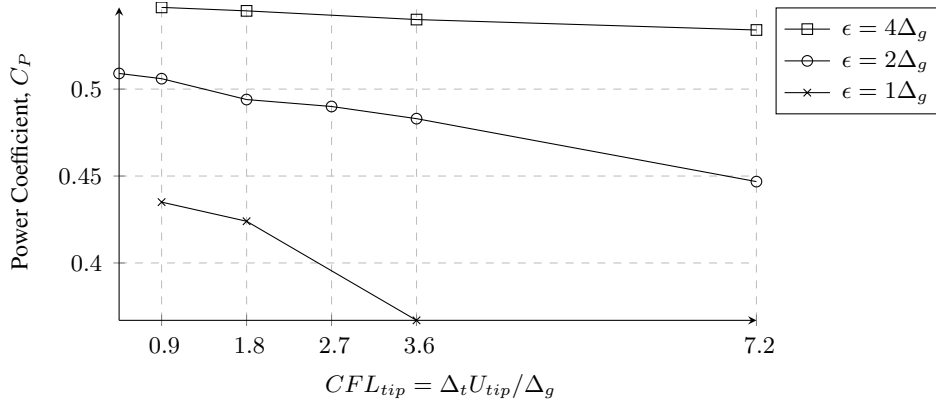


Figure 3.5: Change of predicted C_P with CFL_{tip} for different Gaussian ϵ values ($\Delta_g/R = 1/32$)

$CFL_{tip} = 0.90$ is a reasonable reference value to start with. Fig. 3.5 shows that as the blade tip travels more distance per time step, the predicted power gets lower. In addition, $CFL_{tip} = 0.90$ dependency varies with ϵ (the projection width control parameter); as the projection width increases, C_P becomes less sensitive to CFL_{tip} . When Troldborg's suggestion of $\epsilon = 2\Delta_g$ is used, power coefficient varies in a very small range of 0.45 – 0.59 for the tested tip Courant numbers. BEM result for same conditions is $C_P = 0.48$ but there is no clear indication of convergence towards that value within this range. A solution could not be obtained for $CFL_{tip} = 7.2$ with $\epsilon = 1\Delta_g$, which is due to peak force approaching very large values such that it generates instabilities.

For a fixed $\epsilon = 2\Delta_g$, computed angle of attack and tangential forces are shown in Fig. 3.6. The overall disagreement is attributed to the ϵ value, which is yet to be determined in the following sections. As the CFL_{tip} is increased, computed α and F_t decreases. The variation in tangential force is more pronounced towards the blade tip, where linear velocity and displacement due to rotation are larger. This shows that as the temporal discretization is coarsened, deflected velocity field from the previous time step could not be felt by actuator points in the next time step. From $CFL_{tip} = 0.45$ to 3.60, the deviation remains small and acceptable. $CFL_{tip} = 7.20$ results in a large jump, which makes it unsuited for simulations.

Specific to this case, rotor region refinement level is extended up to 3D downstream distance to enable measurement of velocity profiles at the near wake region, where axial velocity distribution is found to be very close for all CFL_{tip} values (Fig. 3.7).

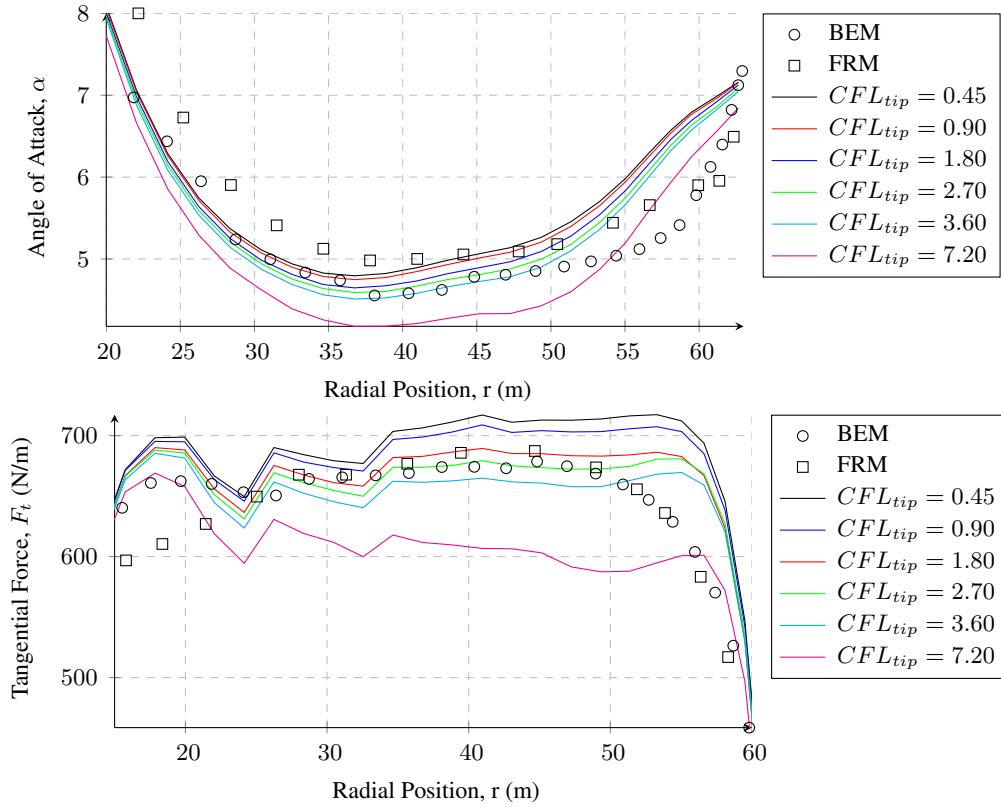


Figure 3.6: Computed Angle of Attack and Tangential Force distributions for different CFL_{tip} values ($\epsilon = 2\Delta_g$) (FRM: [11])

Except for the vicinity of blade tip, velocity profiles are almost identical; whereas the most significant variations are seen in mid-span to tip region, with $CFL_{tip} = 7.20$ showing the largest deviation again. With regards to the velocity deficit ($1 - U_x/U_{ref}$), model is fairly insensitive to time step size within a reasonable range ($CFL_{tip} = 0.5 - 8.0$), but large variations in α and F_t results prevents use of bigger time steps. It can be said that the blade tip can be allowed to exceed 3 cells per time step without a significant loss in accuracy.

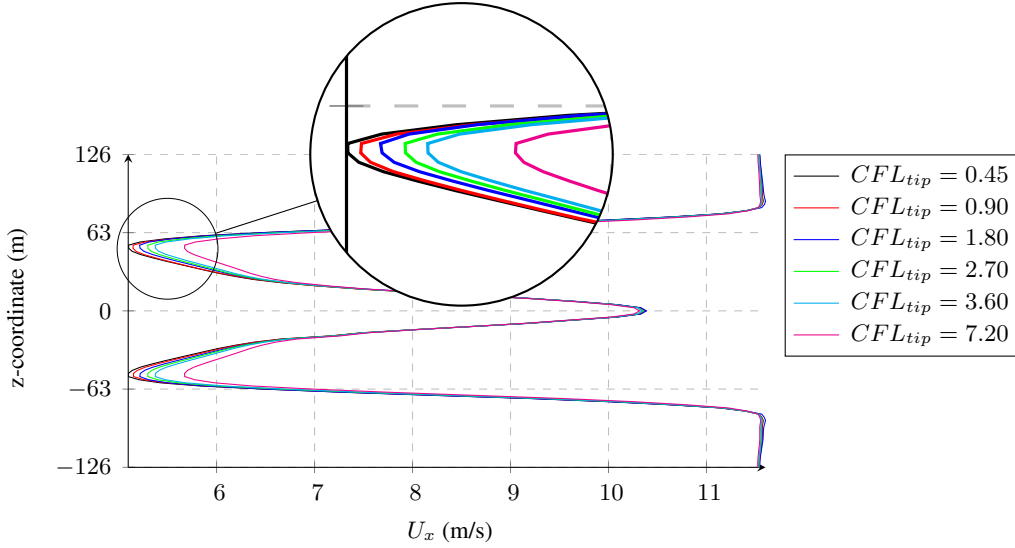


Figure 3.7: U_x profile along z -axis passing through rotation axis at 3D downstream for different CFL_{tip} values.

3.1.3 Spatial Discretization

Grid resolution is the second most influential parameter with respect to the computation time along with time step size. In this section, 3 different refinement levels are tested at the rotor region: $\Delta_g/R = 1/16, 1/32, 1/64$. The refinement is applied only to the rotor region ($-1D$ to $1D$). Accuracy is assessed based on α and F_t distributions along blade span. Choosing a constant value of CFL_{tip} for all simulations would result in different time step size for each grid resolution, which might cause unequal assessment. Hence, Δ_t is kept constant for all grid resolutions, such that $CFL_{tip} = 0.90$ is satisfied on the finest grid $\Delta_g/r = 1/64$. In addition, projection width and cell size are closely related in resultant force distribution. Thus, various ϵ (the projection width control parameter) values are also tested in combination with grid resolution.

Power coefficient is considered the primary convergence criterion throughout this study. Fig. 3.8 shows that for a constant ϵ value, estimated power converges as the grid is refined. Also, different ϵ values has an effect on predicted power, terminal value to be reached and convergence rate. For a smaller ϵ , predicted power and convergence rate decrease simultaneously. For $\epsilon = 5R/64 = 3.94m$, refining the cell size 4 times from $R/16$ to $R/64$ causes C_P to increase by $\approx 3\%$ from 0.500 to 0.514, which is a

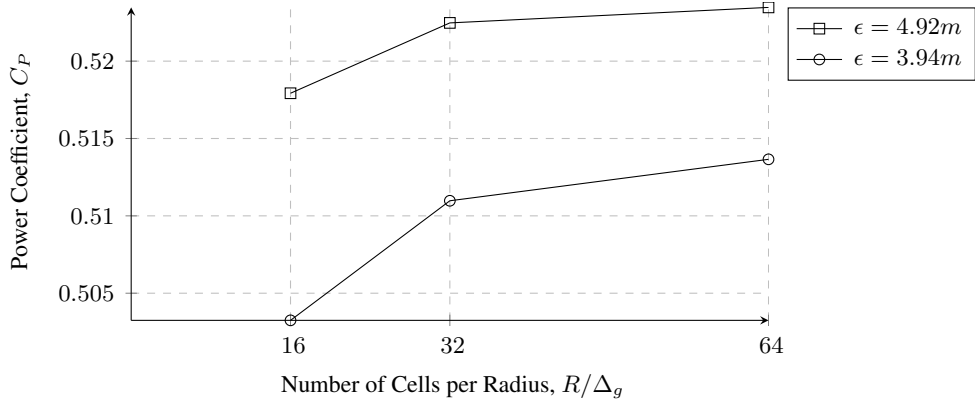


Figure 3.8: Convergence of computed Power Coefficient with various grid resolutions for different grid size independent constant ϵ values

very small change.

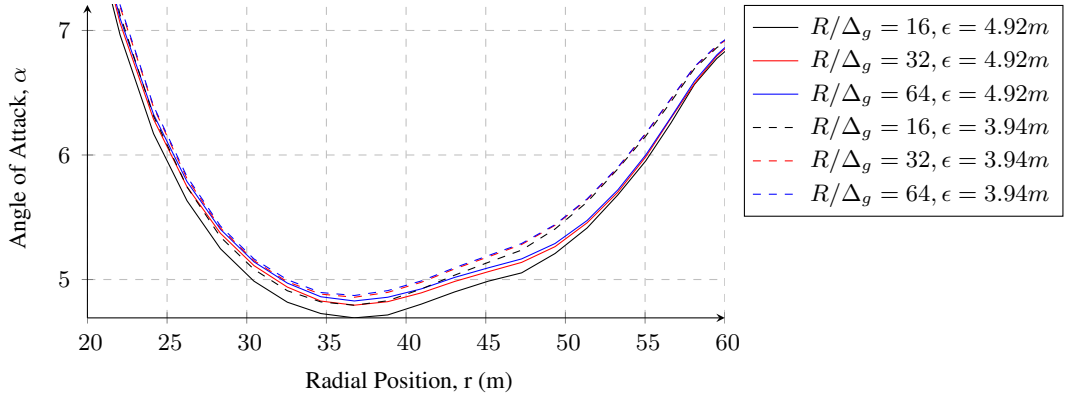


Figure 3.9: Computed Angle of Attack distribution for different constant ϵ values

The variation of angle of attack due to grid size can be seen on Fig. 3.9. Although the overall variation is small, the most affected part is the mid-span region. Forces are smaller towards root and tip due to tip loss effects, therefore grid size has a lesser effect in these regions. Similar trend is visible in F_t graph (Fig. 3.10).

Another cell size-independent method for testing the effect of ϵ on grid size sensitivity is to use chord based ϵ . Fig. 3.11 shows that similar to the constant ϵ case, as the projection width gets larger, power is overpredicted. Compared with other multipliers, reducing ϵ to 1 chord length results in some inconsistent trend, especially for $R/\Delta_g = 32$. This is due to depleted projection widths which causes instabilities and chord size reducing to exceedingly small values towards the tip. This will be discussed in depth in the next section.

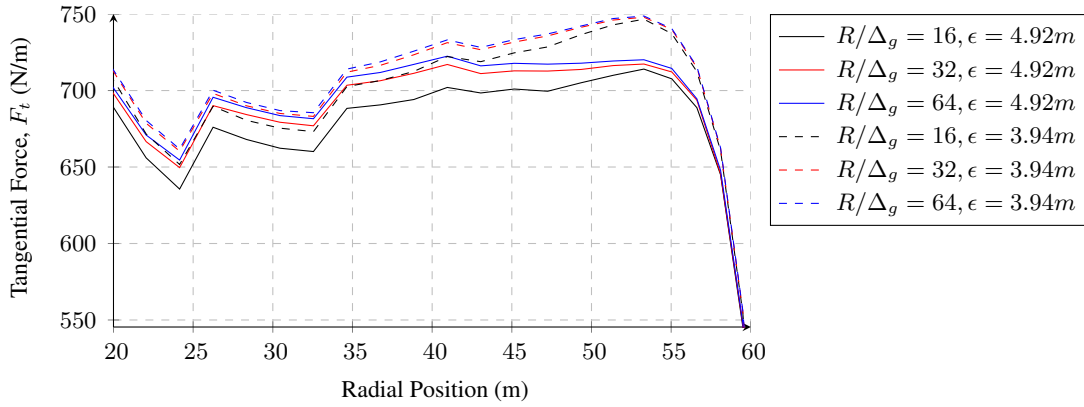


Figure 3.10: Computed Tangential Force distribution for different constant ϵ values

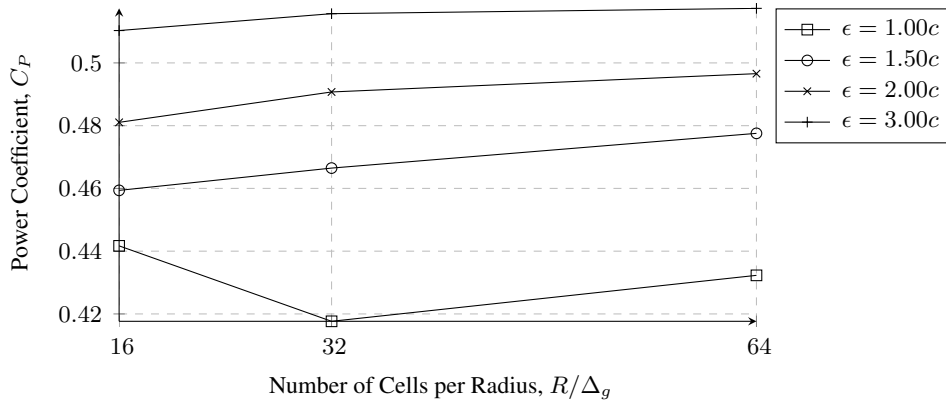


Figure 3.11: Convergence of computed C_P with various grid resolutions for different chord size based ϵ values

If cell size dependent ϵ is used, (Fig. 3.12) projection width varies with the grid size. For the tested $R/\Delta_g = 32 \sim 64$ range, $\epsilon = 1\Delta_g$ and $2\Delta_g$ shows an almost linear trend for grid refinement. For ϵ values larger than $\approx 1.5\Delta_g$, a more convergent behavior is observed and convergence rate becomes proportional with ϵ value.

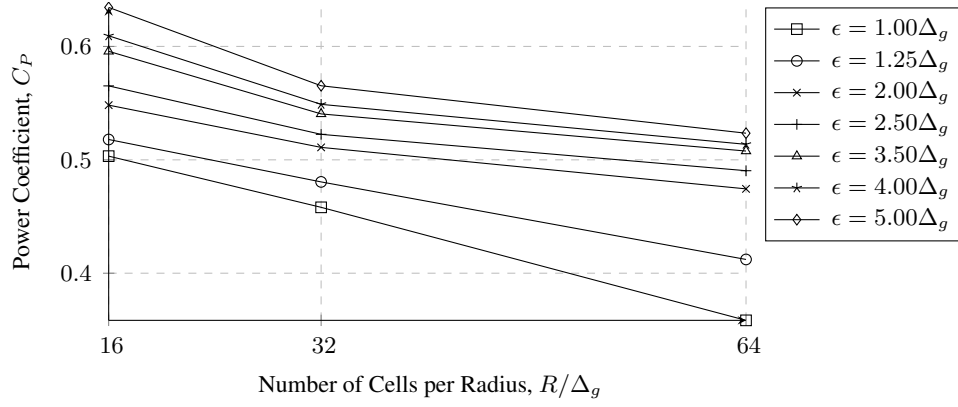


Figure 3.12: Convergence of computed C_P with various grid resolutions for different cell size based ϵ values

3.1.4 Force Projection Width and Gaussian ϵ

Lift and drag forces calculated by 2D airfoil theory are *smear*ed to cell centers in the vicinity of the actuator point. Distribution is done isotropically, i.e. in the shape of a sphere. The largest force is applied on the closest cell to the actuator point (sphere center). The magnitude of this central force is extremely sensitive to the projection width (radius of the sphere), which is controlled by the ϵ parameter (Eq. 2.51). Two commonly used methods to determine ϵ are chord length based and cell size based. Even a small change in ϵ causes a dramatic variation in central force magnitude along blade span. This can be seen for both chord and cell size based ϵ in Fig. 3.13. In this section, both approaches are examined with various multipliers to find the best fitting value.

After realizing that even very small changes in ϵ causes big difference in central force magnitude, 4 different multipliers are tested within 1 – 3 range on 3 different grid resolutions. α and F_t distributions are wiggled in coarser grids, and they are smoothed out as the grid is refined. This is due to the less number of cells in coarser grids, causing each cell to include a larger magnitude of force in Gaussian distribution and the cell which is located closest to the center also get its share. In coarsest grid, computed α shows different trends at blade tip and mid-span: it increases in mid-span but decreases at the tip as ϵ gets larger. Grids with $\Delta_g/R = 1/32$ and finer resolution performed the best for all multipliers. For all grid resolutions, best agreement with both BEM and FRM results is obtained with $\epsilon = 2c$. Even so, chord

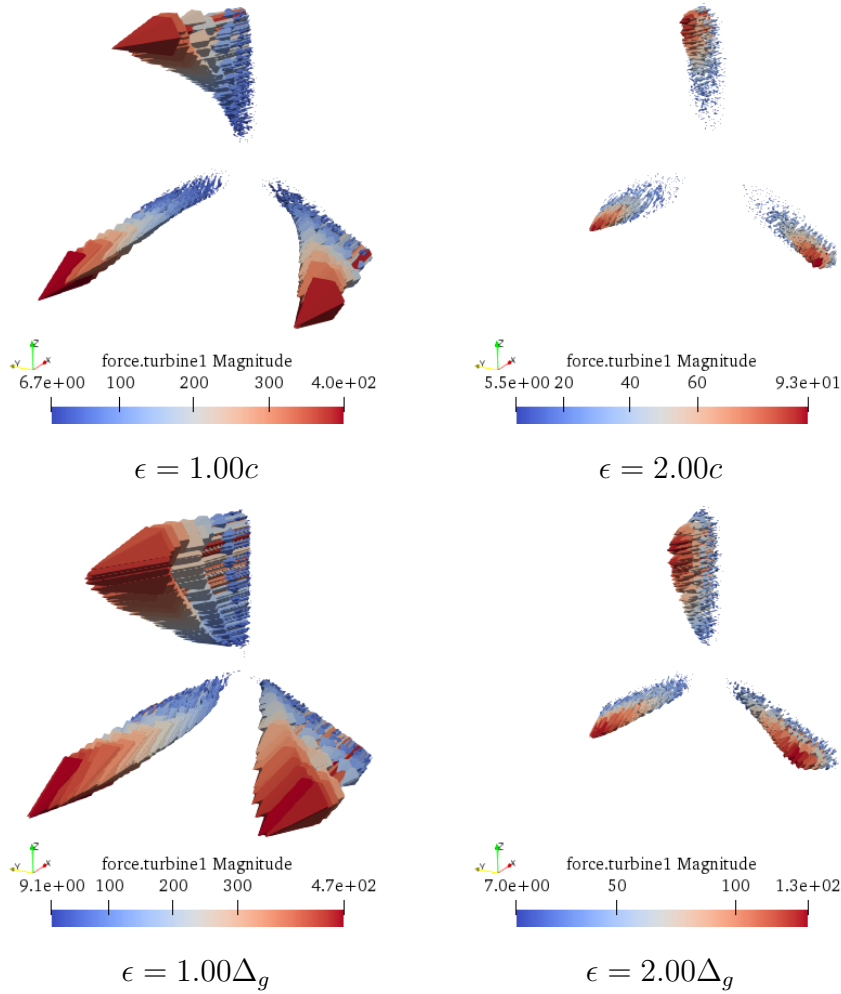


Figure 3.13: Force vector field with different magnitudes of chord and cell size based ϵ (at $\Delta_g/R = 1/64$).

based ϵ method is unable to capture the whole span with a constant multiplier. For instance, F_t computation using $\epsilon = 2c$ in $\Delta_g/R = 1/64$ grid resolution shows a very good agreement with BEM results for $r > 30$, but it is over-estimated towards the root. This is due to the fact that chord is always smaller at the tip, where ϵ gets very small and force distribution is confined in a small sphere. This situation becomes evident in the coarse grids, where grid convergence at the tip behaves in opposite with mid-span. Although NREL 5MW blade has a fairly large span and aspect ratio, this problem would become more evident with wind turbines where chord changes rapidly. Choosing a radial position-dependent multiplier instead of a constant value has a potential of solving this shortcoming; Jha et al. [56] suggests such an elliptic distribution.

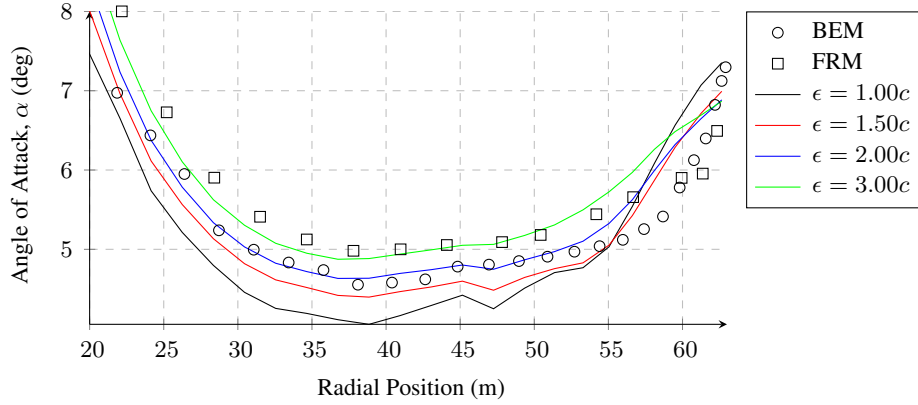


Figure 3.14: Computed α for different chord based ϵ values (at $\Delta_g/R = 1/16$) (FRM: [11])

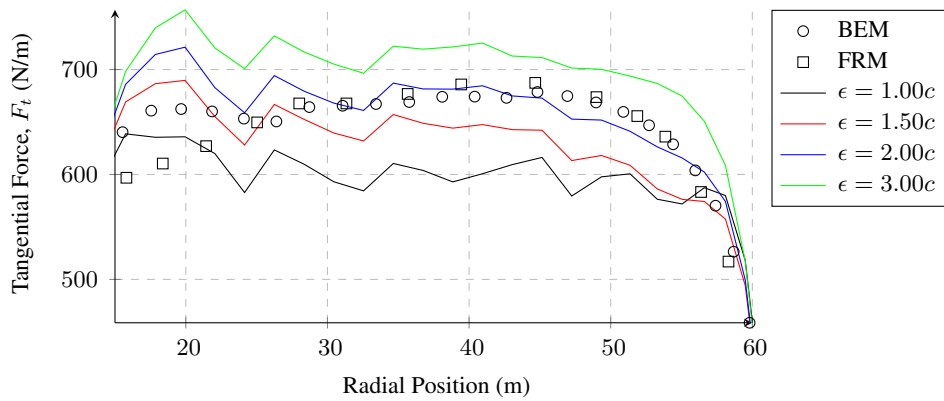


Figure 3.15: Computed F_t for different chord based ϵ values (at $\Delta_g/R = 1/16$) (FRM: [11])

For the cell size based ϵ case, 7 different multipliers between 1 – 5 are tested. As the grid is refined, angle of attack and force predictions gets lower. Similar to the chord based method, F_t is more sensitive to ϵ variations towards the tip, where tangential forces are larger. This sensitivity is more pronounced as the grid gets coarser; in the coarsest grid, the effect of variation of ϵ is almost negligible on F_t , whereas tangential force distribution varies as a whole in finest grid up to $\epsilon = 2\Delta_g$. Small projection width causes wiggles in the distribution curves, larger ϵ provides smoothing but augments over-prediction. In the coarsest grid, none of the tested multipliers gives a good α and F_t computation; an overall over-prediction is observed with large deviations in the tip region. With $\Delta_g/R = 1/32$ resolution, $\epsilon = 1.25\Delta_g$ yields the best results. On the finest grid, best performing multiplier is 2.50, showing linear proportionality with cell size. Even though, 64 cells per radius has a better agreement throughout the span, whereas some discrepancy can be seen before and

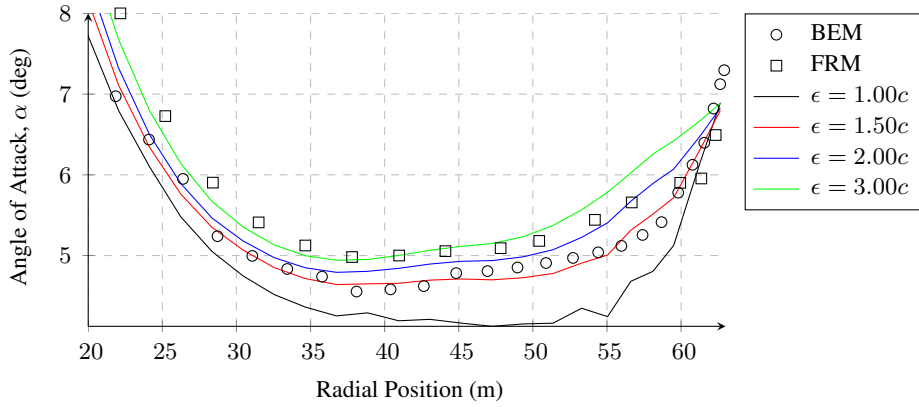


Figure 3.16: Computed α for different chord based ϵ values (at $\Delta_g/R = 1/32$) (FRM: [11])

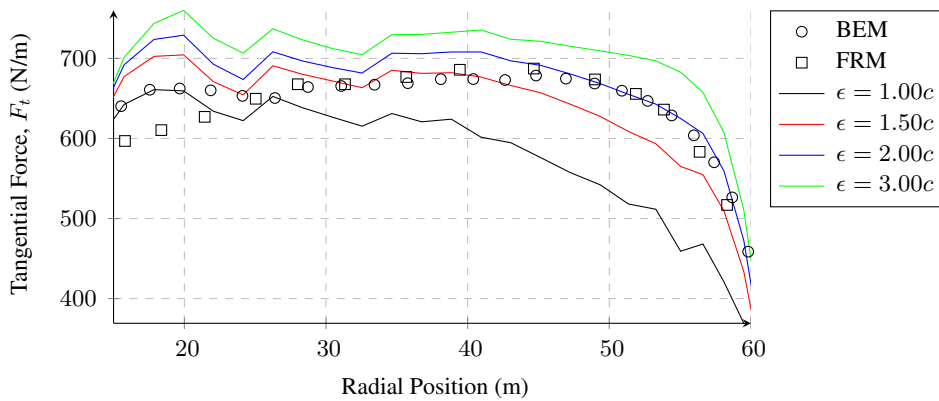


Figure 3.17: Computed F_t for different chord based ϵ values (at $\Delta_g/R = 1/32$) (FRM: [11])

after $R \approx 53m$ for $\Delta_g/R = 1/32$.

Compared to the chord based approach, cell size based ϵ method yields more consistent α and F_t distributions along blade span. For $\Delta_g/R = 1/32$ and greater values, a constant $\epsilon = 2.461m$ yields the nearest α and F_t results vis-a-vis BEM.

There is no clear indication of power coefficient convergence towards the BEM result of 0.48 for the tested parameters. It can be interpreted that rate of convergence increases as the ϵ gets larger, but experimentations with ϵ shows that this does not necessarily yield better angle of attack and force predictions; hence results which are close to 0.48 are mostly coincidental here. Chord based ϵ lacks any sort of convergent behavior on coarsest grid, some convergence can be seen as the grid is refined but the terminal value is definitely larger than 0.48. In contrary, cell size based ϵ approach exhibits a convergent trend towards BEM result with further grid refinement past

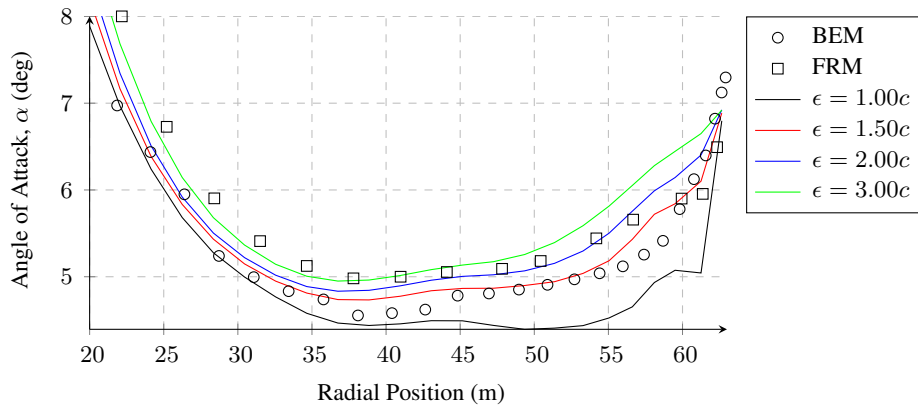


Figure 3.18: Computed α for different chord based ϵ values (at $\Delta_g/R = 1/64$) (FRM: [11])

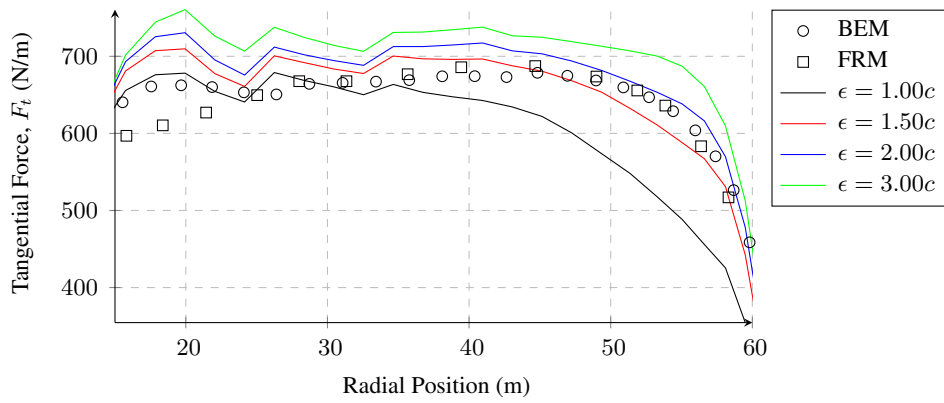


Figure 3.19: Computed α for different chord based ϵ values (at $\Delta_g/R = 1/64$) (FRM: [11])

$\Delta_g/R = 1/64$. However, this level of discretization is out of the goal of current computational power and final simulations.

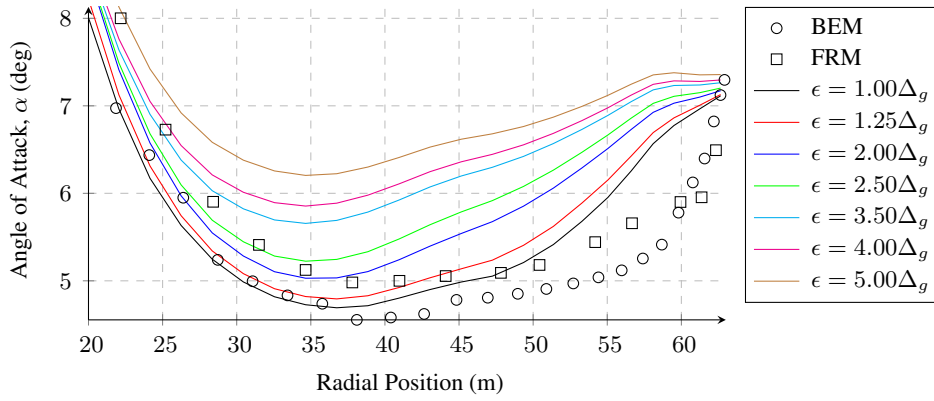


Figure 3.20: Computed α for different cell size based ϵ values (at $\Delta_g/R = 1/16$) (FRM: [11])

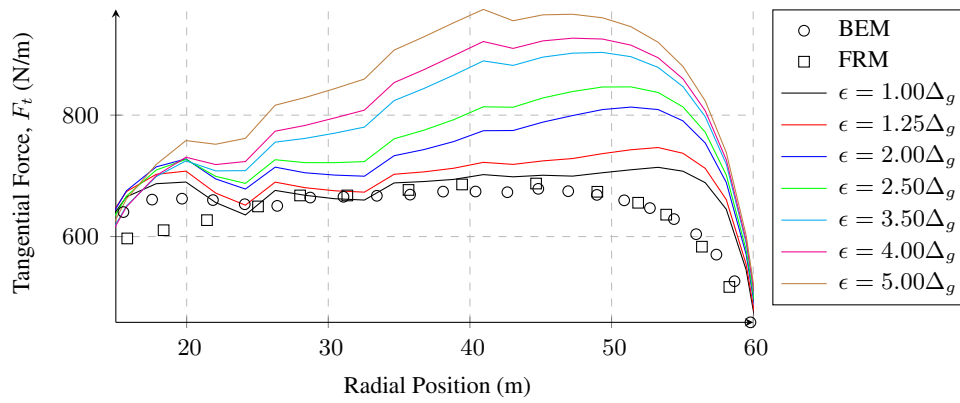


Figure 3.21: Computed α and F_t for different cell size based ϵ values (at $\Delta_g/R = 1/16$) (FRM: [11])

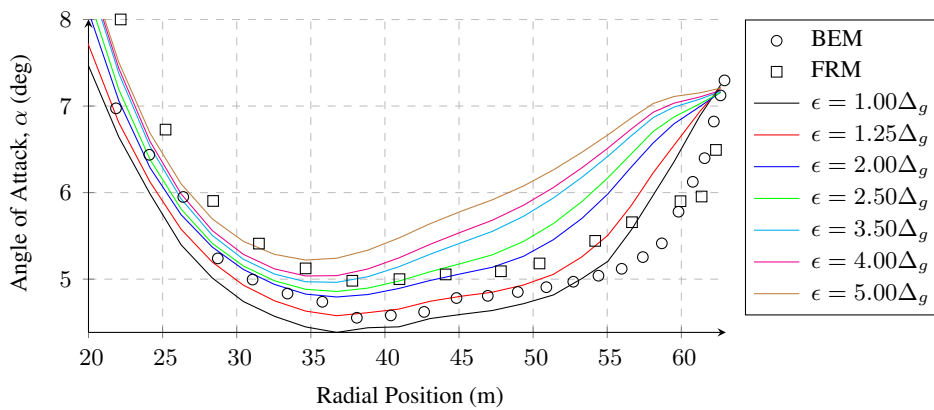


Figure 3.22: Computed α for different cell size based ϵ values (at $\Delta_g/R = 1/32$) (FRM: [11])

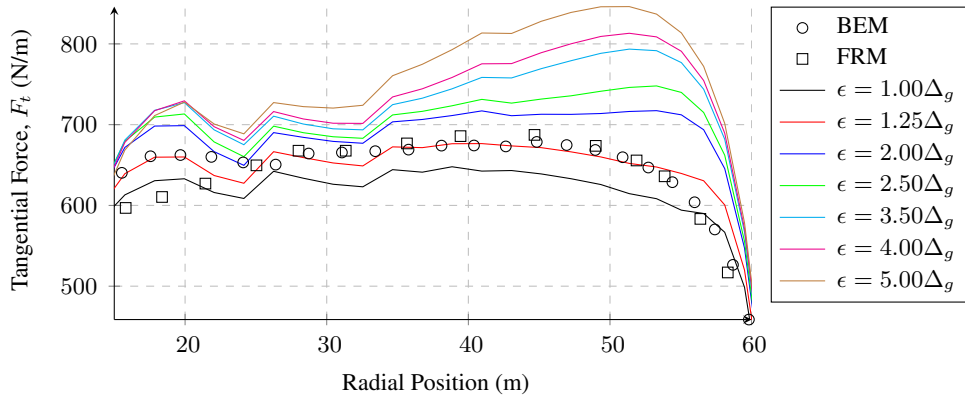


Figure 3.23: Computed α and F_t for different cell size based ϵ values (at $\Delta_g/R = 1/32$) (FRM: [11])

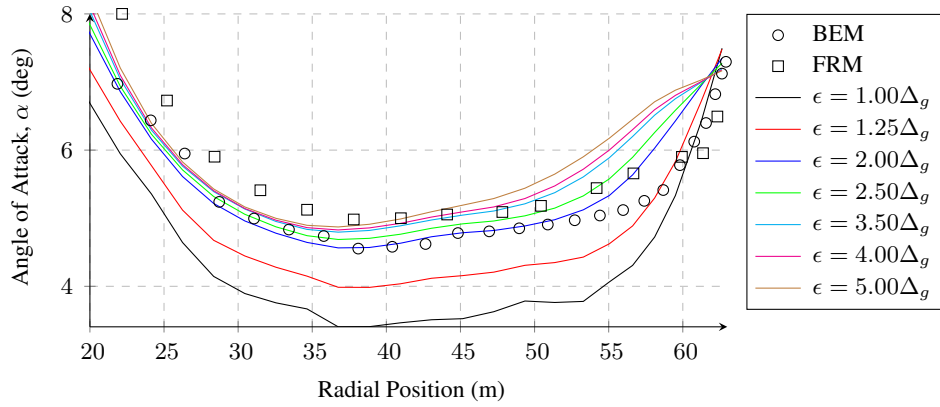


Figure 3.24: Computed α for different cell size based ϵ values (at $\Delta_g/R = 1/64$) (FRM: [11])

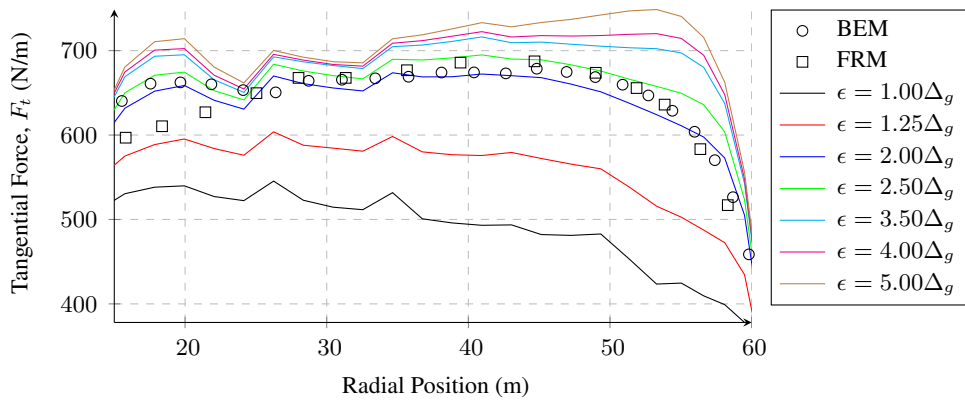


Figure 3.25: Computed α and F_t for different cell size based ϵ values (at $\Delta_g/R = 1/64$) (FRM: [11])

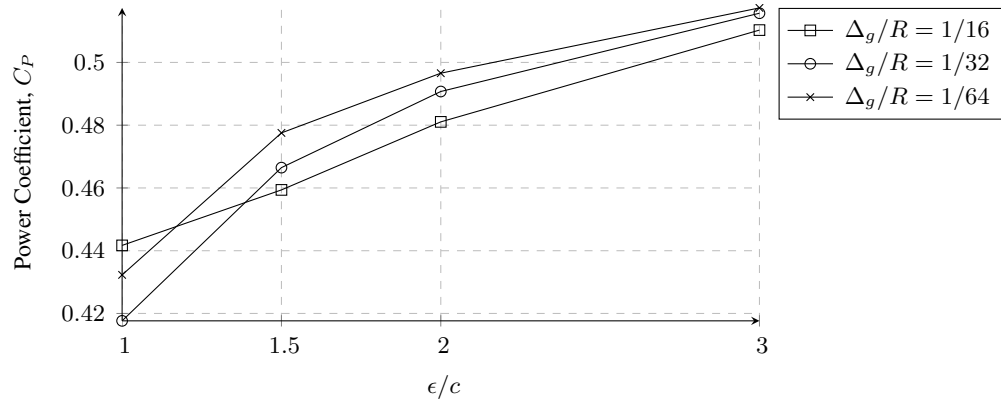


Figure 3.26: Convergence of computed C_P with chord based ϵ values for different grid resolutions

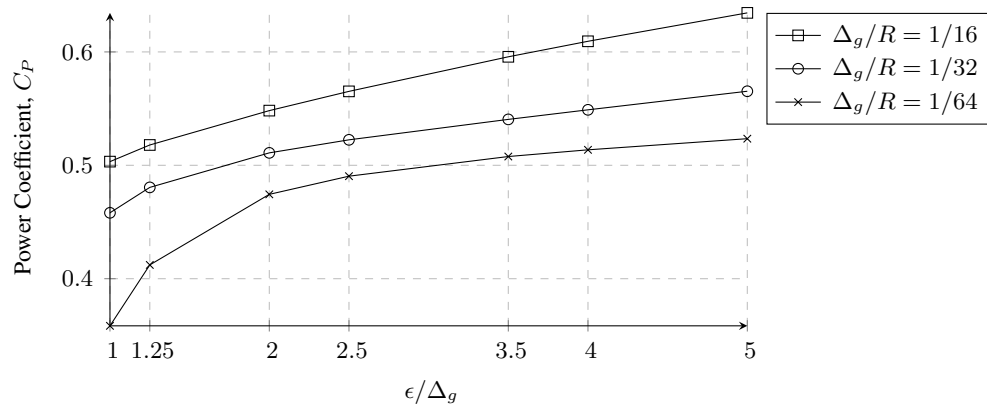


Figure 3.27: Convergence of computed C_P with cell size based ϵ values for different grid resolutions

3.1.5 Number of Actuator Points

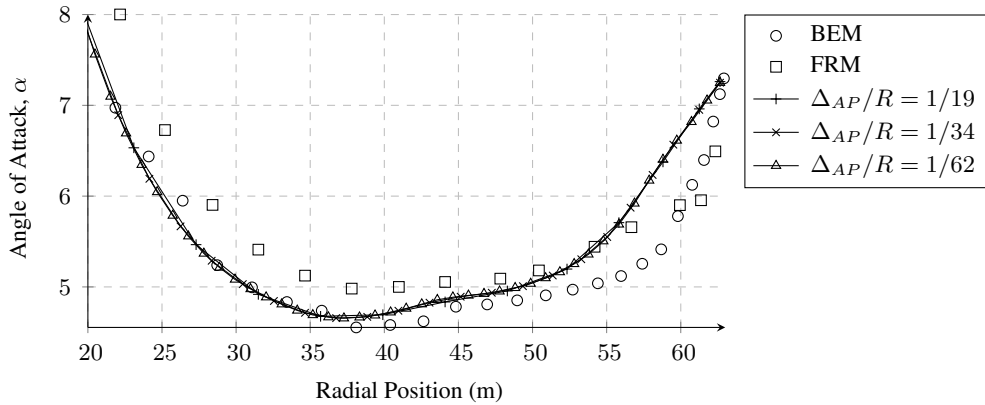


Figure 3.28: Computed α for different number of actuator points (FRM: [11])

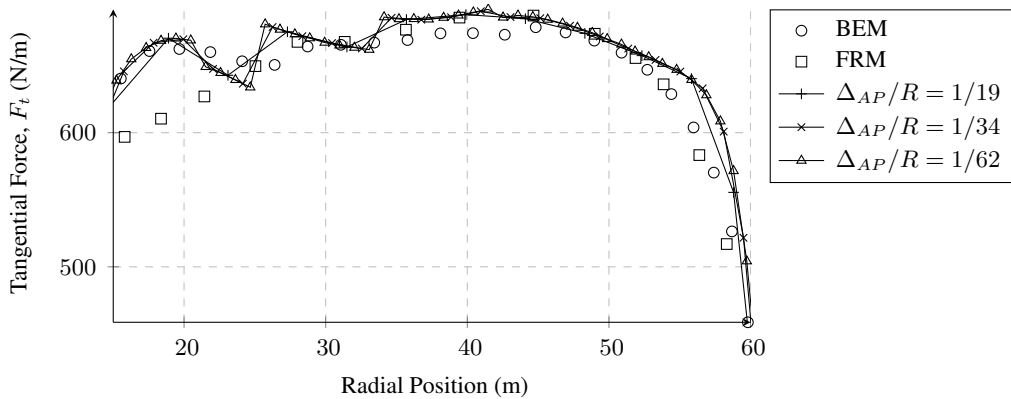


Figure 3.29: Computed F_t for different number of actuator points (FRM: [11])

Three different number of actuator points are tested on $\Delta_g/R = 1/32$ grid resolution. The least refined distribution $N_{AP}/R = 19$ consists of the data originally provided by NREL for turbine definition, whereas for $N_{AP}/R = 62$ distribution, refinement is such that none of the elements' size exceed $1.2m$. Results are almost identical, except the fact that using more actuator points provides a better resolution of α and F_t with increasing data points. As a downside, $N_{AP}/R = 62$ takes approximately 12% more computation time compared to $N_{AP}/R = 19$.

3.1.6 Results with Various Rotational Speeds

For a grid resolution of $\Delta_g/R = 1/32$, a single isolated wind turbine is simulated for different TSR values using the best performing ϵ (the projection width control

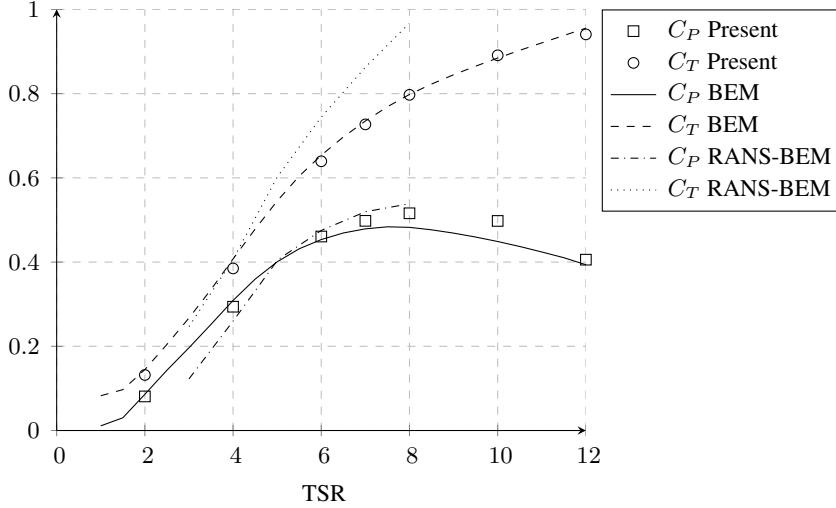


Figure 3.30: Computed power and thrust coefficients for different tip speed ratios at $U_{ref} = 11.4m/s$ (RANS-BEM: [12])

parameter) value of $1.25\Delta_g$. Since the tip speed varies with changing TSR, time step size is adjusted accordingly to satisfy $CF L_{tip} = 0.90$; i.e. Δ_t gets smaller as TSR is increased. Thrust coefficient is in excellent agreement with BEM results, whereas power coefficient has some discrepancies at higher rotational speeds ($TSR > 7$). Deviations as large as 7% show up at $TSR = 10$. Although overall angle of attack predictions are good, a clear difference is observed towards blade tip at all TSR values. As TSR gets larger, under-prediction of tangential force up to $r = 30m$ is aggravated.

One important finding in various TSR simulations is that as the rotational speed gets larger, simulation time needed for convergence increases dramatically, and similarly more computation time is needed for the same amount of simulation time. Fig. 3.32 shows an error histogram of C_P , calculated using a moving average approach:

$$E_{C_P} = \frac{|\overline{C_{P,10}} - \overline{C_{P,30}}|}{\overline{C_{P,30}}} \quad (3.1)$$

where $\overline{C_{P,n}}$ is the median of C_P in the last n seconds.

Assuming that the convergence criteria is $E_{C_P} < 10^{-3}$, a large difference in required simulation time exists between two extreme TSR values of 2 and 12: convergence is achieved at $t \approx 20s$ with $TSR=2$, whereas more than 200s of simulation time

is needed for $TSR=12$. The average number of PIMPLE iterations required for convergence at each time step is 3 and almost constant for all TSRs, which does not explain the slow-down. At the start of each simulation, the velocity field is initialized with uniform $U = 11.4m/s$ and turbines are *instantaneously* introduced into the flow domain. The convergence observed here is the flow around turbine blades adjusting itself according to the deflection caused by force field generated by blades; and forces being calculated with respect to the computed velocity field at the same time. This result is attributed to the fact that at higher rotational speeds local circumferential velocities at element centers are larger resulting in a large over-estimation during the initial steps of simulation (Fig. 3.33). Thus, it takes a longer simulation time for force-velocity coupling to be solved.

Some jumps are evident in both graphs (Fig. 3.33 and Fig. 3.32). As mentioned earlier, largest force is imposed on the actuator point itself and this force is passed on to the cell centers by interpolation. During blades' rotation, distance between actuator points and grid points constantly change in an irregular manner. These jumps are attributed to interpolation distances getting certain values for all blades at some time steps, such that power output is affected dramatically but is corrected again over time.

3.1.7 Summary

The study on an isolated rotor has shown that using $\epsilon = 1.25\Delta_g$ on a grid with $\Delta_g/R = 1/32$ resolution is the most efficient choice for wake interaction simulations. Although solution keeps converging at $\Delta_g/R = 1/64$ and further grid refinement, computational efficiency overweighs the accuracy, considering the fact that discretizing the whole region between rotors would increase the grid size eight fold. Although number of actuator points shows no impact on blade loading predictions, $\Delta_{AP}/R = 1/34$ is chosen since it provides the minimum actuator point spacing where width does not exceed the chord on each element. In terms of time step size, discrepancies are found to be within an acceptable limit of up to $CFL_{tip} = 1.80$.

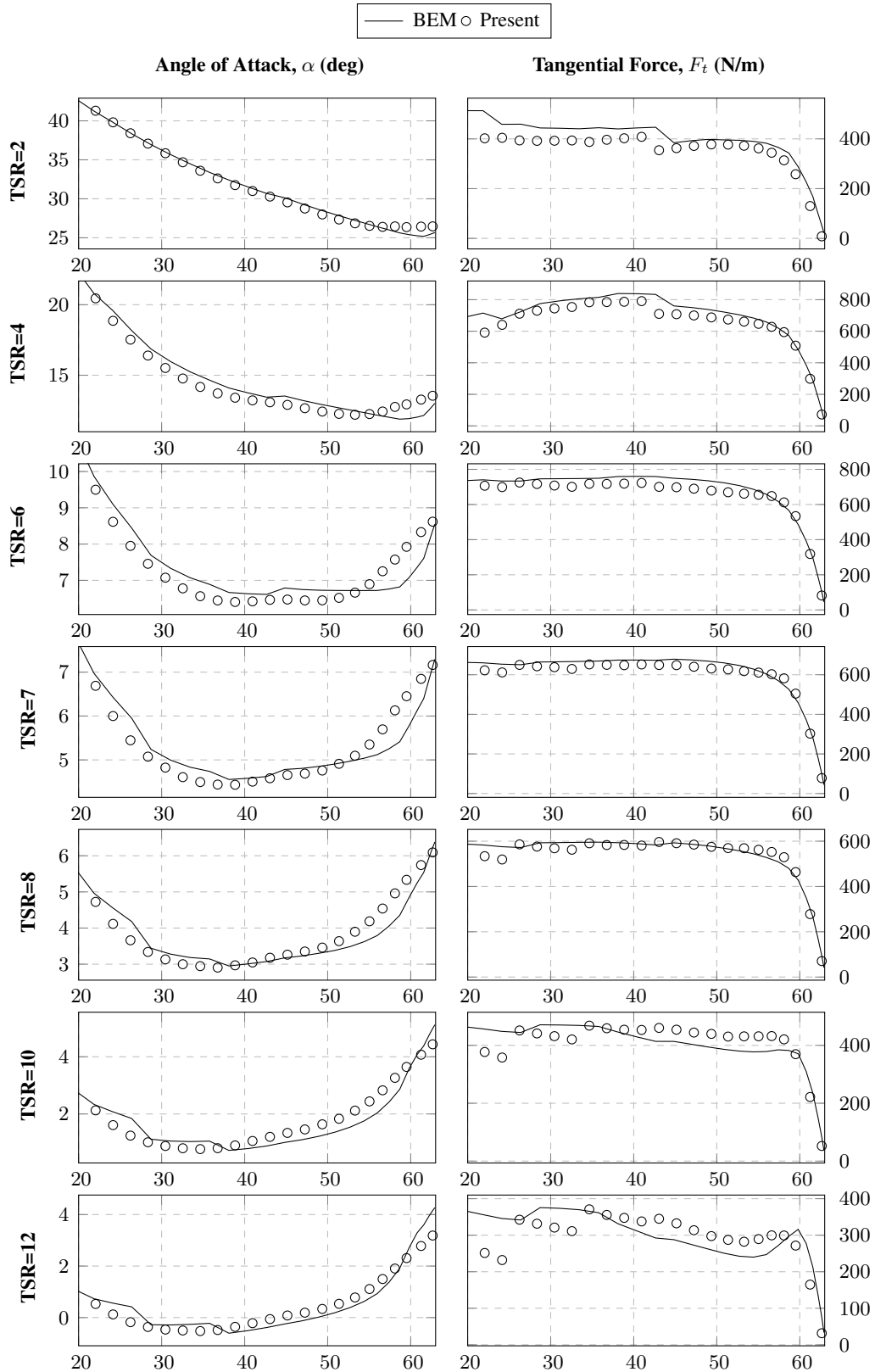


Figure 3.31: Computed α and F_t distributions for different TSR values (at $U_{ref} = 11.4\text{m/s}$, $\Delta_g/R = 1/32$). Horizontal axes represents radial position on the blade in meters.

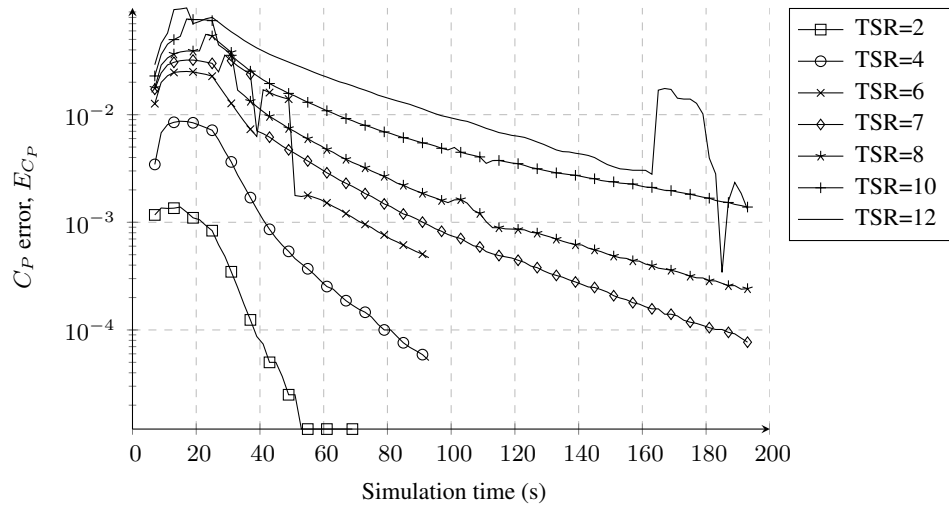


Figure 3.32: C_P error history of simulations with different TSR (smoothened out via moving average)

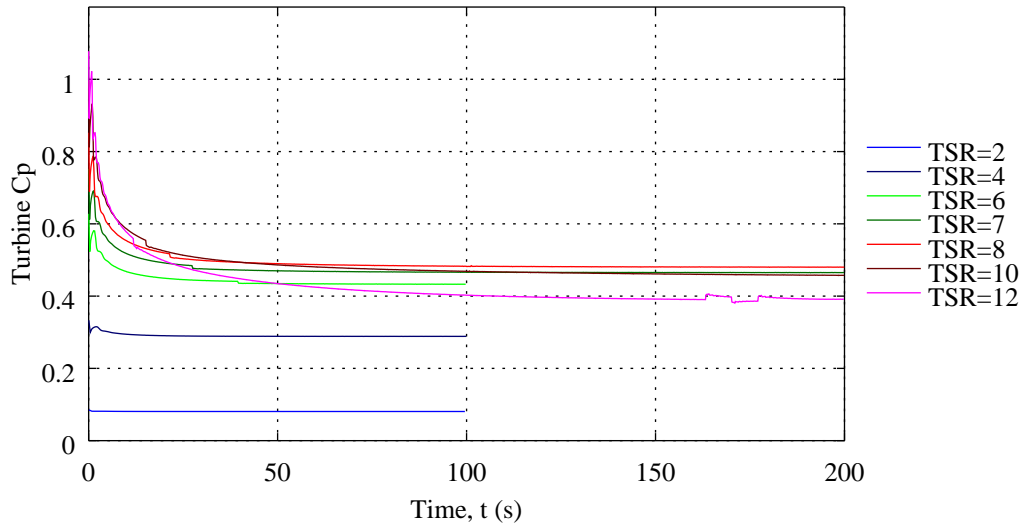


Figure 3.33: C_P convergence history of simulations for different TSR

3.2 Wake Interaction Simulations of Two Wind Turbines in Tandem

In this section, two rotors are placed in the flow domain and wake interaction between them is simulated using Actuator Line Model. Flow is examined under 3 different conditions:

1. Incoming flow is uniform where both rotors are isolated from boundary conditions,
2. Atmospheric Boundary Layer (ABL) is modeled over a flat terrain,
3. Upstream rotor is yawed under ABL flow.

In all simulations, parameters that are suggested in the previous section are used. Atmospheric turbulence is absent and the incoming flow is laminar. Reference velocity is $U_{ref} = 8.0m/s$ and tip speed ratio is $TSR = 7.3$, corresponding to rotational speed $\Omega \approx 8.9RPM$. Pitch angle is zero. Rotors are axially separated by a distance of $7D = 882m$ and rotor centers are located on the x-axis, axially aligning the wind turbines.

Field variables are printed at every $1/3^{th}$ of revolution, when a blade is closest to the zero azimuthal (vertical) position. Grid resolution is $\Delta_g/R = 1/32$ and tip Courant number is $CFL_{tip} = 1.80$, with only exception being the $\Delta_g/R = 1/16$ isolated rotors simulation where $CFL_{tip} = 0.90$ is selected to obtain equivalent time step size. Rotor region refinement level is kept constant up to the downstream rotor and $3.5D$ more. Simulation time is $t_{final} = 500s$, corresponding to approximately 74 rotor revolutions. In the following sections, WT1 and WT2 denotes upstream and downstream wind turbines, respectively.

3.2.1 Uniform Inflow Acting on Two Isolated In-line Wind Turbines

With both rotor axes aligned, flow is simulated without any yaw or tilt angle. Vortices shed from WT1 directly impinge on WT2 blades. The wake generated by WT1 covers a distance of $\approx 5D$ in the first $t = 100s$, and reaches WT2 around $t = 150s$. The laminar inflow and absence of atmospheric turbulence can be observed in the wake

structures of both turbines until wake impingement. After $t = 150s$, eddies within the wake region of WT2 becomes evident, while wake of WT1 remains undisturbed. Expansion of wake can be seen starting $\approx 2D$ before WT2.

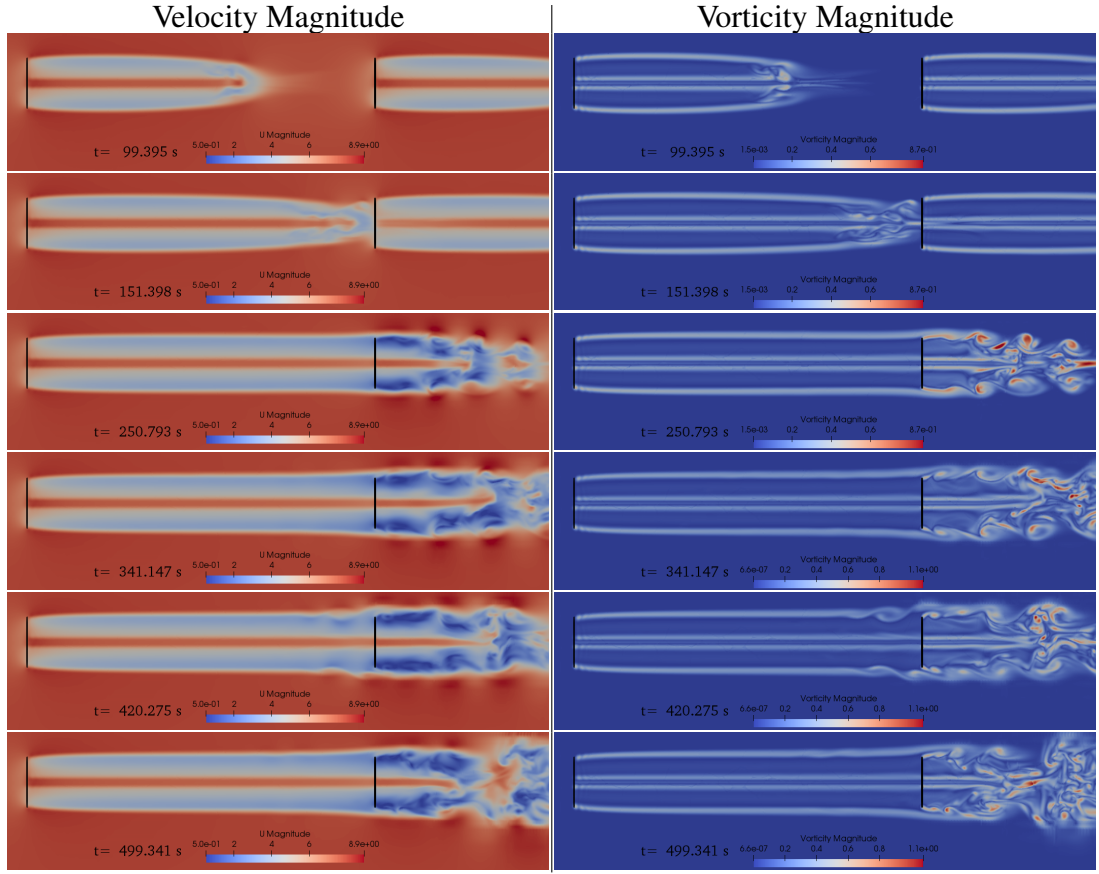


Figure 3.34: *Velocity and vorticity magnitude contours during wake development (uniform inflow, mid-z-plane section)*

Computed wake structures are in accordance with Troldborg's findings (Fig. 1.4) with and without atmospheric turbulence, where shed vortices persists without breaking down when the flow is undisturbed. One big difference is that eddies become evident after $\approx 5D$ downstream in Troldborg's solution, which is attributed to the much finer grid used ($\Delta_g/R = 1/70$). Computed vortex contours are very similar to that of Schmitz and Jha's simulations [88].

One of the conventional methods used for vorticity detection is Q -criterion, given as;

$$Q = \frac{1}{2} (|\mathbf{\Omega}|^2 - |\mathbf{S}|^2) > 0 \quad (3.2)$$

where $\mathbf{\Omega}$ and \mathbf{S} are the vorticity and strain-rate tensors, respectively. $Q = \text{constant}$

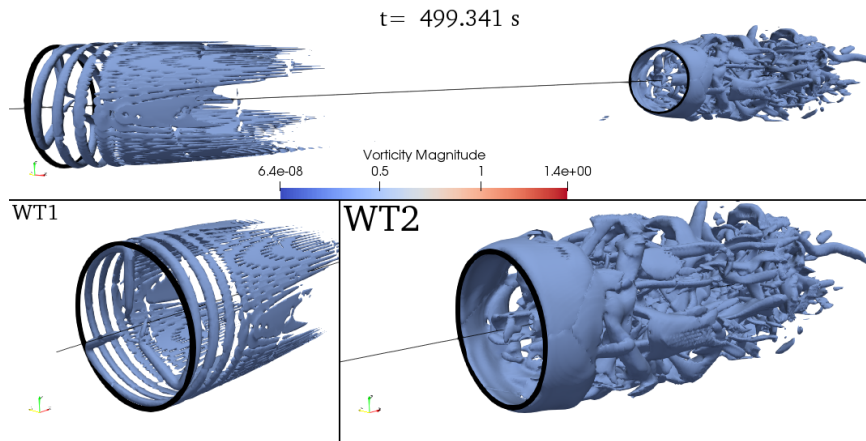


Figure 3.35: Vorticity $\zeta = 0.38$ iso-surfaces (uniform inflow case, $\Delta_g/R = 1/32$)

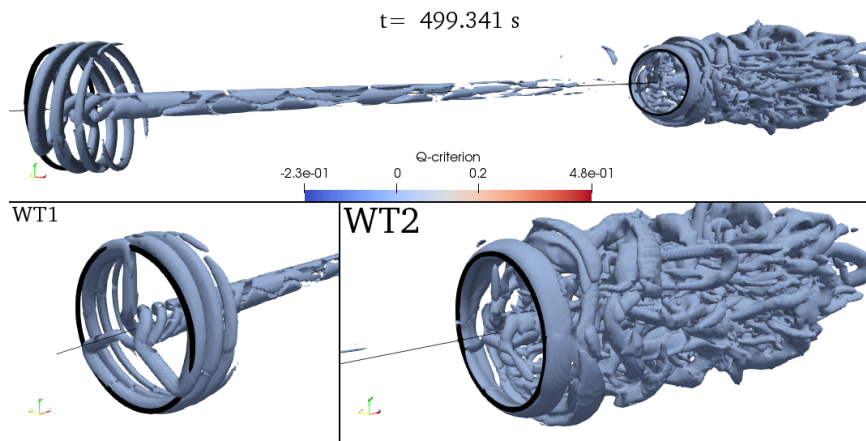


Figure 3.36: Q-criterion $Q = 0.005$ iso-surfaces (uniform inflow case, $\Delta_g/R = 1/32$)

contours for isolated wind turbines in tandem configuration are given in Fig. 3.36. Similar to vorticity contours, helical structures emanating from blade tips are distinctive. In addition, same structures originating from blade roots are visible with Q-criterion, unlike vorticity. Looking at the Q-criterion definition, this indicates that strain rate is larger relative to vorticity magnitude at blade root.

In addition to the solution with $\Delta_g/R = 1/32$ grid, a simulation with a coarser grid ($\Delta_g/R = 1/16$) is also performed in this configuration, to observe computed wake structures' dependency on grid size. Borders of vortical structures and transition between low/high velocity regions are captured with better precision in finer grid. The difference is more evident in the wake of WT2, where vorticity contours are almost axi-symmetric in the low resolution grid and eddies are more pronounced and

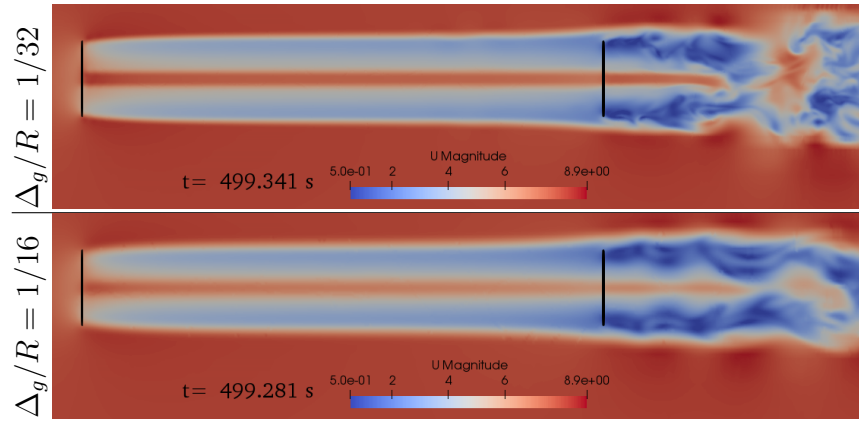


Figure 3.37: Instantaneous velocity magnitude contours on different grid resolutions (uniform flow, mid-z-plane section)

distinct on the finer grid.

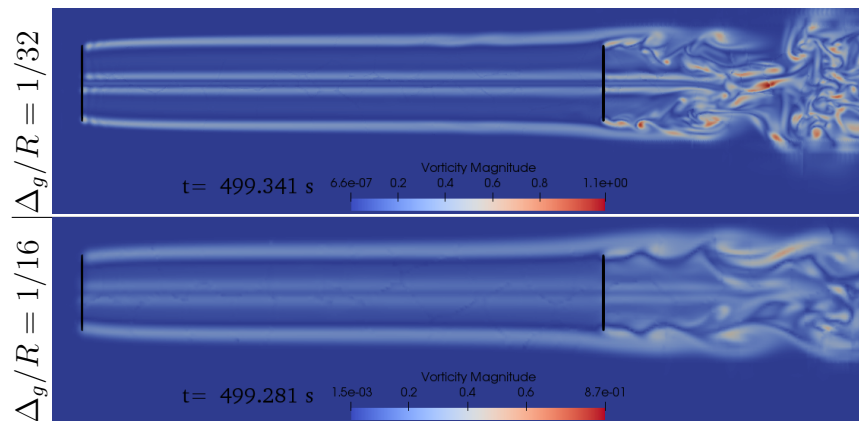


Figure 3.38: Instantaneous vorticity magnitude contours on different grid resolutions (uniform flow, mid-z-plane section)

Velocity deficit contours for both grid resolutions exhibits fairly close results up to WT2, where the largest discrepancy is observed closer to the centerline (Fig. 3.39). This similarity is related to the fact that are plotted quantities are time-averaged. Nevertheless, results become more distinct after WT2, due to the increased eddy motion and coarser grid's shortcoming in capturing it. Overall, wake recovery can not be obtained and deficit velocity profiles persist up to WT2. After WT2, due to the already generated turbulence, a dramatic increase in wake recovery is visible withing a very small distance. This shows the importance of introduction of atmospheric turbulence in the simulation of wake interactions.

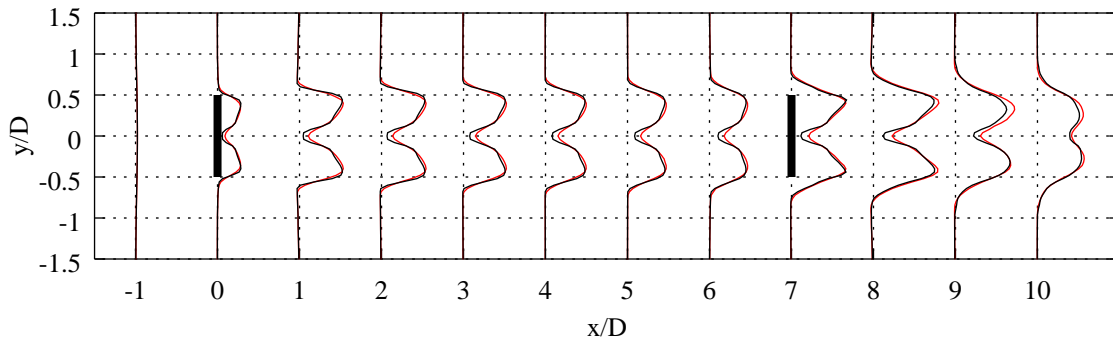


Figure 3.39: Mean axial velocity deficit ($1 - U_x/U_{ref}$) profiles along y (horizontal) axis at different x stations (isolated rotors case). (— $\Delta_g/R = 1/16$) (— $\Delta_g/R = 1/32$).

In terms of computed angle of attack and force distributions, both grid resolutions yield close results for WT2, where forces are much smaller compared to WT1 (Fig. 3.40). Largest difference is observed in WT1 results, especially the region closer to the tip. This is in accordance with the previous results, where differences are pronounced as inflow velocity magnitude and computed forces become larger.

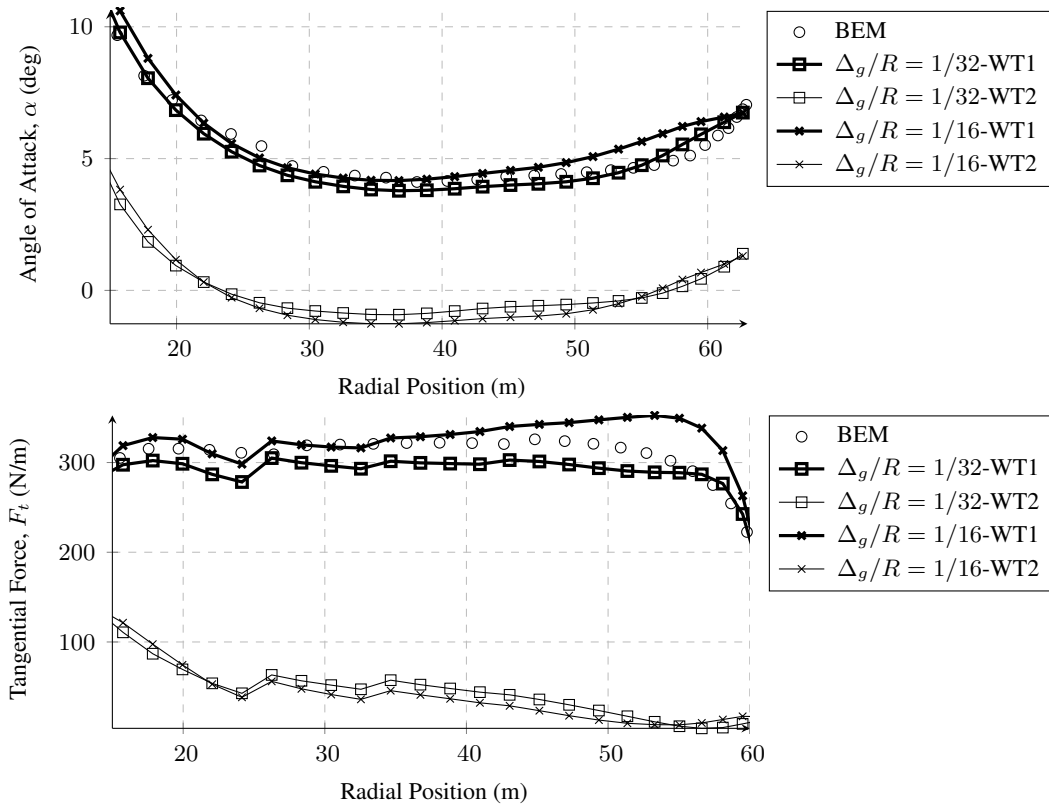


Figure 3.40: Computed α and F_t for different grid resolutions (isolated dual turbines case, averaged over last 5 revolutions).

3.2.2 Sheared Inflow Acting on Two In-line Wind Turbines on Flat Terrain

To obtain a realistic atmospheric shear flow profile and turbulence properties at the inlet, it is a common practice to run a precursor simulation without the turbines. In that approach, periodic inflow and outflow boundaries are used for the domain. Thus, a fully developed flow can be extracted from the outflow boundary of this simulation, and then applied to the inflow boundary of the actual domain of the wind farm site. This procedure requires resolution of terrain boundary layer in the precursor simulation. Because of the computational expense and the fact that a simpler ABL profile is sufficient for the scope of this study, an analytical model is used at the inlet instead of a precursor case.

At the inflow boundary, ABL profile is applied using OpenFOAM's built-in `atmBoundaryLayer` patch type, which is suggested by Hargreaves and Wright [89] based on the friction velocity. In this model, assuming z is the vertical

coordinate, axial component of velocity as a function of z , $U_x(z)$ is given by:

$$U_x(z) = \frac{U^*}{\kappa} \ln \left(\frac{z + z_0}{z_0} \right) \quad (3.3)$$

where U^* is the friction velocity. Since this model was developed for $k - \varepsilon$ turbulence model, friction velocity is related to turbulent kinetic energy and dissipation rate.

$$k = \frac{(U^*)^2}{\sqrt{C_\mu}} \quad (3.4)$$

$$\varepsilon = \frac{(U^*)^3}{\kappa(z + z_0)} \quad (3.5)$$

Above equations satisfy the conservation of k and ε . Here, z_0 is the surface roughness height, which is estimated as $0.001m$ to reflect typical offshore conditions for this case [22]. $\kappa = 0.41$ is the von Karman constant and $C_\mu = 0.09$ is turbulence viscosity coefficient. Using this analytical approach, terrain boundary layer is not resolved by any means, such that the first cell center is located in the outer layer ($y^+ > 100$).

This case differs from the previous uniform flow simulation only in terms of incoming flow profile, which varies only in the z -direction. Examining the flow in the mid- z -plane section that is passing through the rotor centers show that despite the constant free stream velocity along y -axis, structure of the wake gets deformed towards WT2 (Fig. 3.41). Wake center remains on the x -axis in uniform flow case, hence this formation is due to the eddies emanating from ground and wake-ground interaction. After the wake reaches WT2, it is deflected towards $-y$ direction. Occurrence of this deflection towards a certain direction is attributed to the rotation direction of the wind turbine, which is CW when faced from upstream side.

Velocity deficit profiles show that wake is dissipating towards lateral directions in contrary to the uniform flow case (Fig. 3.42). Higher velocity deficit is found at 1D downstream, which gets dissipated gradually and exhibits a more expanded shape with lower deficit, reaching its minimum at 6D downstream. This is attributed to the already sheared incoming flow causing an additional eddy generation as the flow advances, which contributes to break-down of the wake. This phenomena is more

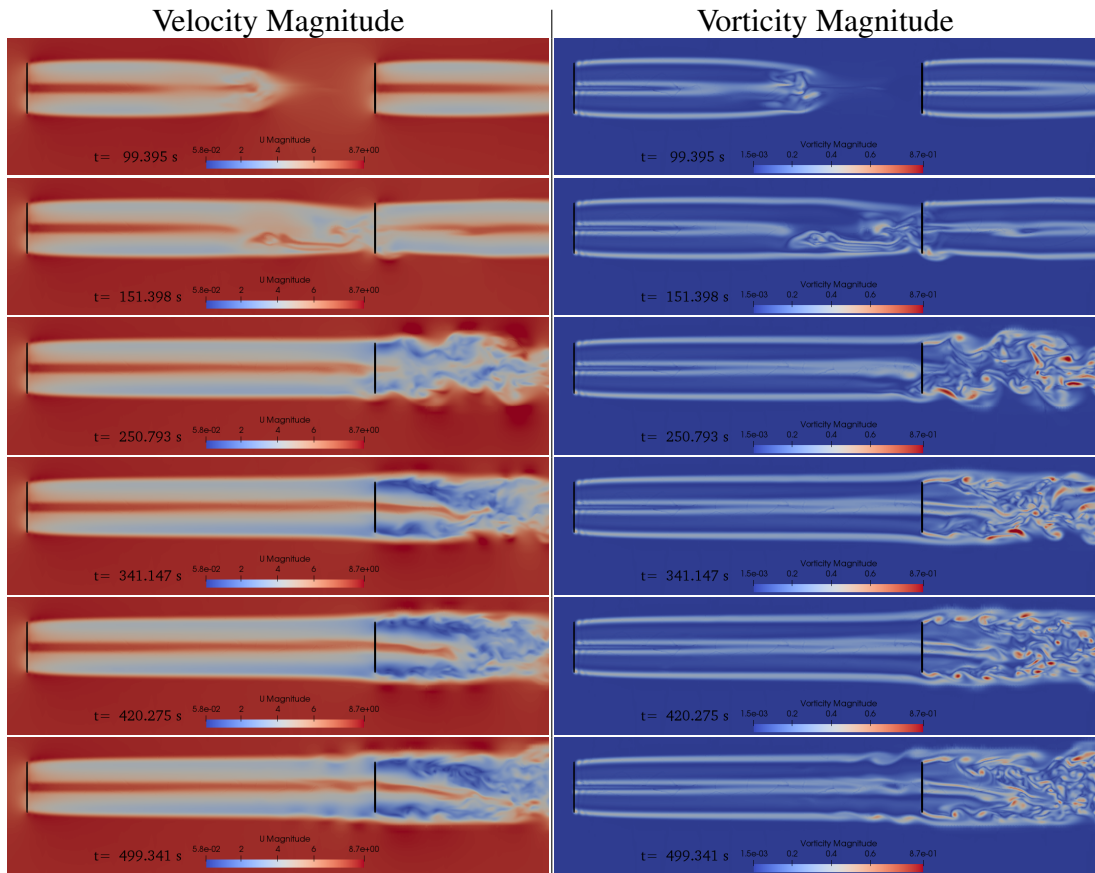


Figure 3.41: *Velocity and vorticity magnitude contours during wake development (ABL inflow, mid-z-plane section)*

evident after the WT2, where the rotor is subject to an already turbulent incoming flow and increased eddy motion causes faster wake recovery. Indeed, shape of the velocity deficit profile undergoes a dramatic change within a 2D distance between 8D and 10D.

Looking at the mid-y-plane section (side view), the initial rotor/ground interaction is evident in the form of vortex structures (Fig. 3.43). Vortices generated due to this interaction are visible up to $t \approx 340s$, where after a periodically-steady state is achieved. Center of wake is also slightly shifted upwards due to sheared flow (can be assessed relative to the black line, which represents centerline). This shift is maximum approximately at the half way to WT2, then the wake center is shifted down as it approaches WT2.

Velocity deficit profiles along z-axis depicts the atmospheric boundary layer and wake

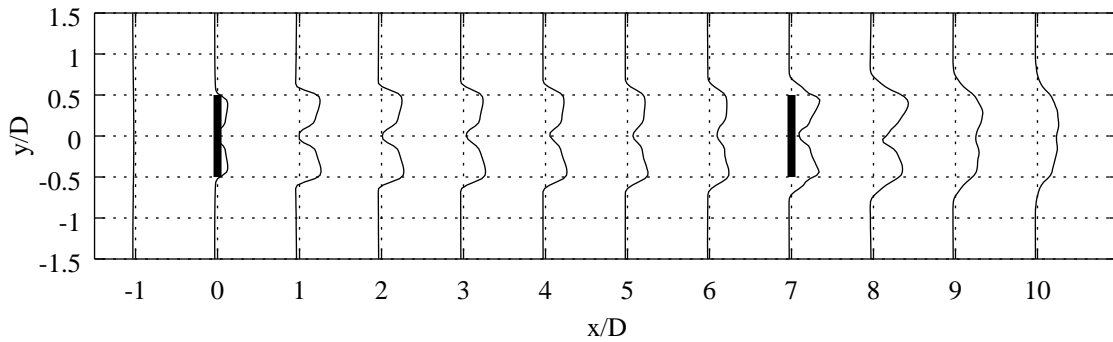


Figure 3.42: Mean axial velocity deficit ($1 - U_x/U_{ref}$) profiles along y (horizontal) axis at different x stations (ABL flow case).

recovery. Velocity deficit at the center remains zero (again, due to absence of hub definition) all the way from WT1 to WT2. As in the case of uniform inflow, this is due to the lack of atmospheric turbulence. Even so, a certain amount of wake recovery can be observed in the vertical direction due to sheared flow. After WT2, wake recovery is accelerated due to additional introduction of eddy motion with WT2's rotation.

Maximum vorticity value in the domain is increased to $4.2s^{-1}$ from $1.4s^{-1}$ compared to the uniform flow case (Fig. 3.45). High vorticity is observed in the ground vicinity, where flow is sheared the most. Helical structures that are generated by the upstream turbine are evident, but this type of pattern is lacking after WT2, similar to the uniform flow case. In the Q-criterion contours, effect of vortices generated in the ground is absent (Fig. 3.46). This indicates that shear rate magnitude is close to that of vorticity on the ground, due to the definition of Q-criterion.

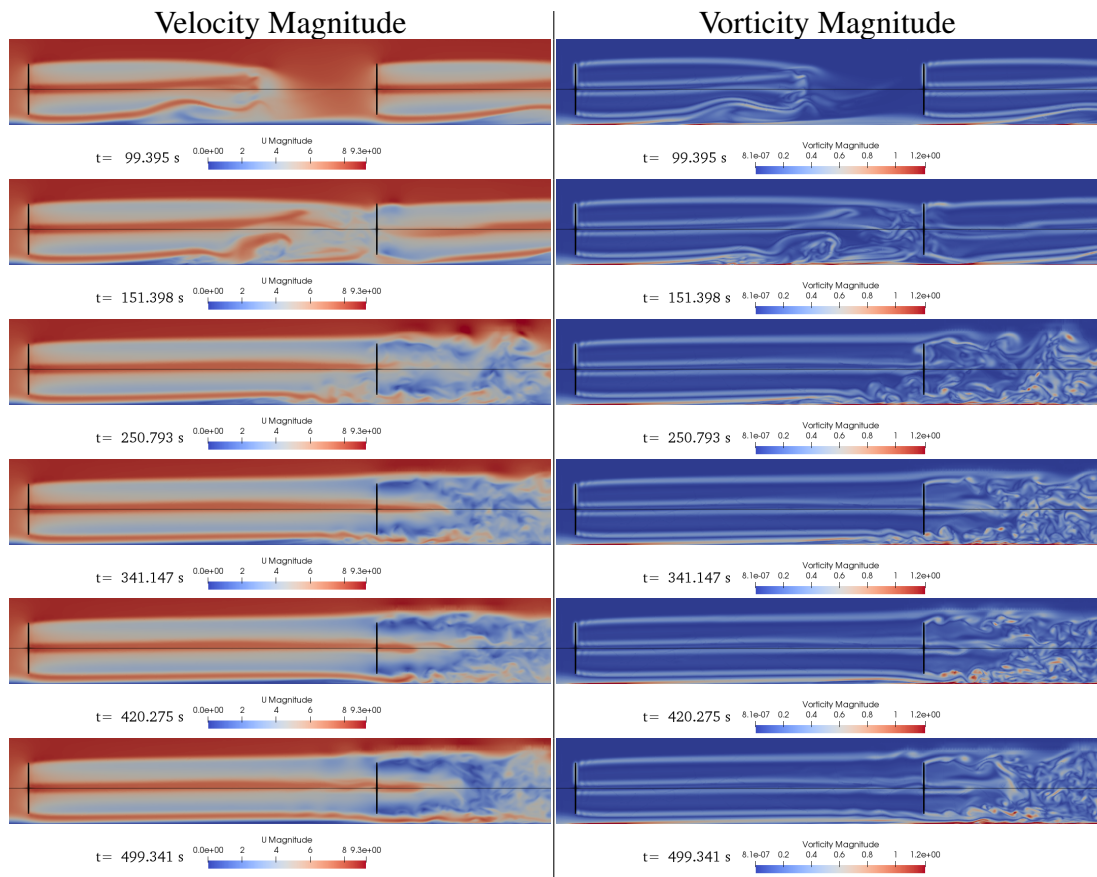


Figure 3.43: Velocity and vorticity magnitude contours during wake development (ABL inflow, mid-y-plane section)

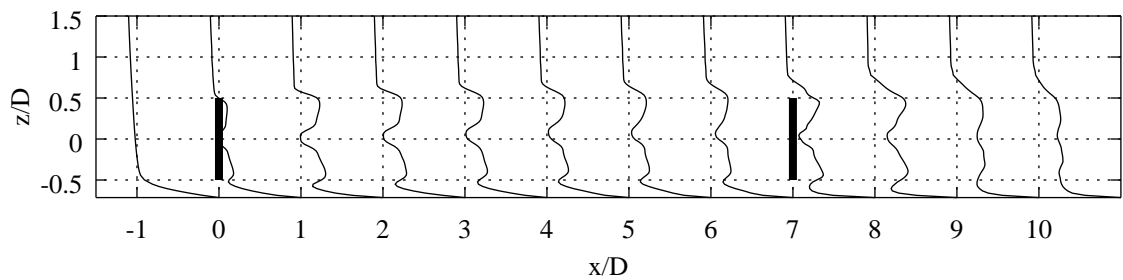


Figure 3.44: Mean axial velocity deficit ($1 - U_x/U_{ref}$) profiles along z (vertical) axis at different x stations (ABL flow case).

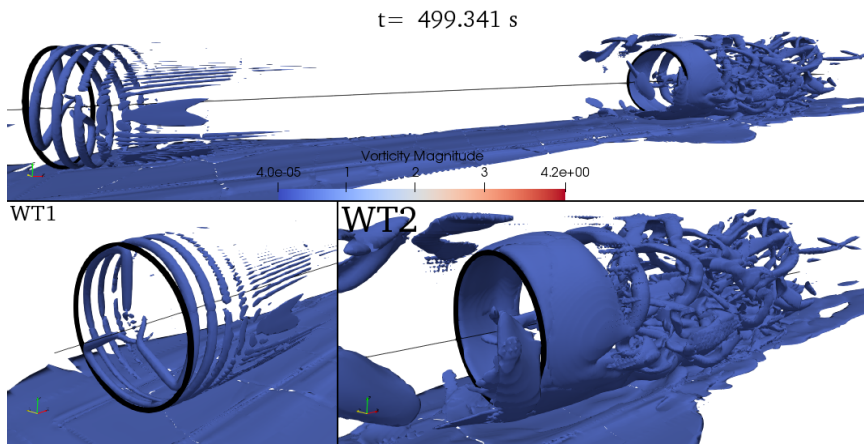


Figure 3.45: Vorticity $\zeta = 0.38$ iso-surfaces (ABL inflow case)

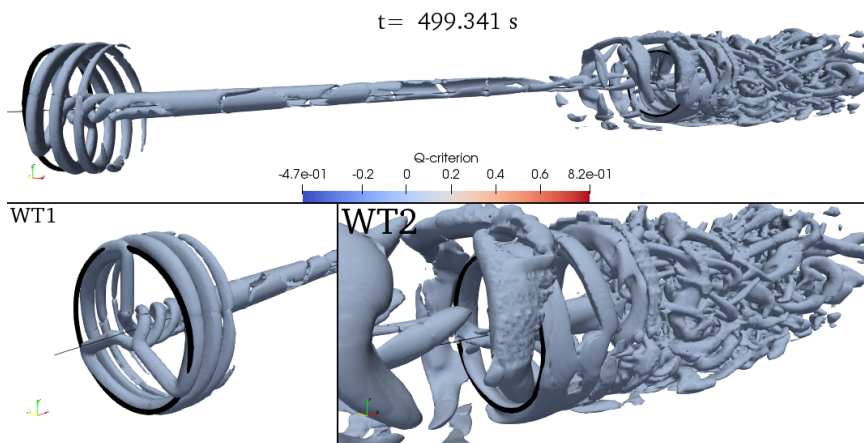


Figure 3.46: Q -criterion $Q = 0.005$ iso-surfaces (ABL inflow case)

3.2.3 Sheared Inflow Acting on Two In-line Wind Turbines on Flat Terrain with Upstream Turbine Yawed

It is a common practice to yaw or tilt upstream rotors to gain an overall increase in power production. In this case, in addition to the ABL flow presented in the previous section, WT1 is yawed $+25^\circ$ with respect to the $+z$ axis (rotor is rotated towards $-y$ direction). Wake deflection is clearly visible on the mid- z -plane section (top view) of velocity contours (Fig. 3.47). Due to the absence of hub in the turbine model, there is a lack of velocity deficit in the rotor center. Stream-wise wind speed remains high without being deflected for $\approx 2D$ on the rotor axis. Then, wake center is gradually shifted towards the $-y$ direction (same direction which the rotor is yawed towards) as it moves downstream. In contrary, tip vortices undergoes a rapid deflection. This is due to the amount of deflection being significantly larger at the higher radial positions of the rotor. After $\approx 2D$ downstream of WT1, vortices shed from the tips reach the root vortices, causing them to deflect along. Effect of wake re-direction is not felt by WT2 until $t \approx 150s$, when wake of WT1 reaches the downstream rotor.

Velocity deficit profiles along y -axis makes a quantitative assessment of wake redirection possible (Fig. 3.48). Yawing the rotor causes the center of the wake to gradually move towards the yaw direction. Wake center is shifted by $0.5D$ as it impinges on WT2. This means that half of the downstream wind turbine rotor remains unaffected by the wake throughout the operation. Wake recovery after WT2 takes place more rapidly when compared to the uniform and ABL without yaw cases presented previously. Also due to the wake redirection, velocity deficit zone is expanded into a wider region, ranging from $-1D$ to $0.5D$ at $x = 10D$.

Mid- y -plane section (side view) shows that the wake center moves towards the ground as it leaves WT1, in contrast to the non-yawed case (Fig. 3.49). It is clear that both rotational direction and yaw direction causes a certain form of wake deflection. Since the section plane is aligned along the axis despite the fact that wake center is deflected towards $-y$ direction, vortices which are shed from the $+y$ half of the rotor are cut by this plane, hence a highly unsymmetrical plot is generated. Further differences are not as apparent.

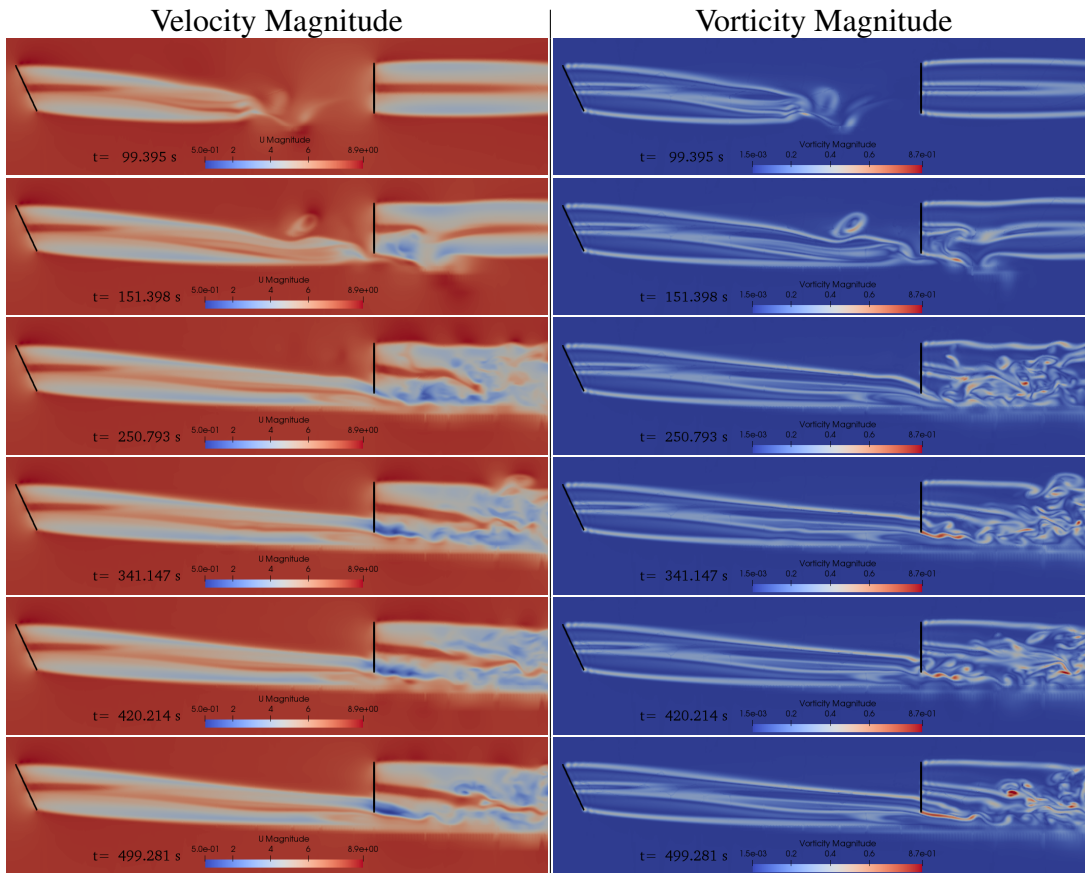


Figure 3.47: *Velocity and vorticity magnitude contours during wake development (ABL inflow, mid-z-plane section)*

Velocity deficit profiles for this case exhibits some differences from the non-yawed case, specifically on the rotor alignment axis (Fig. 3.50). Since the wake is deflected towards $-y$ direction, profiles are far from being axi-symmetric after $x = 2D$, where wake is actually out of the cut plane. The axi-symmetry is more evident after WT2, since it is not deflected, therefore so is the wake.

Vorticity and Q-criterion contours are plotted in terms of single value iso-surfaces in Fig. 3.51 and Fig. 3.52, respectively. As it is apparent, there is not significant variations from the already mentioned non-yawed case, except the $+y$ side of the WT2 generates vortex helices since upstream wake has no effect and flow is laminar in that region. Similar observation can be made from the Q-criterion contours, including the dissipation of eddies after 3 rotations downstream.

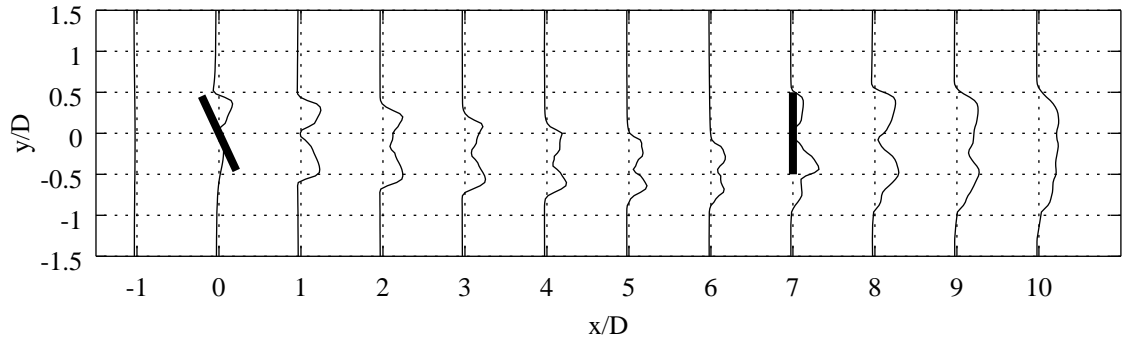


Figure 3.48: Mean axial velocity deficit ($1 - U_x/U_{ref}$) profiles along y (horizontal) axis at different x stations (ABL flow case with WT1 yawed).

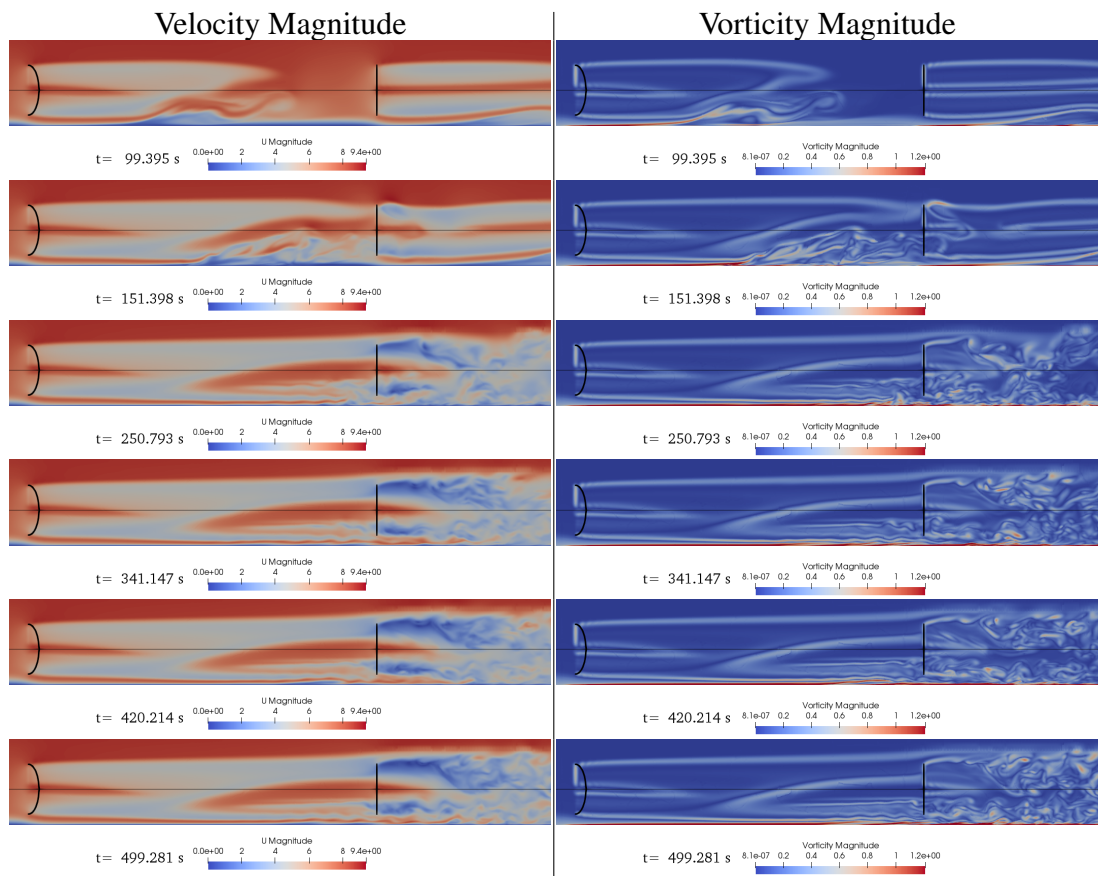


Figure 3.49: Velocity and vorticity magnitude contours during wake development (ABL inflow, mid- y -plane section)

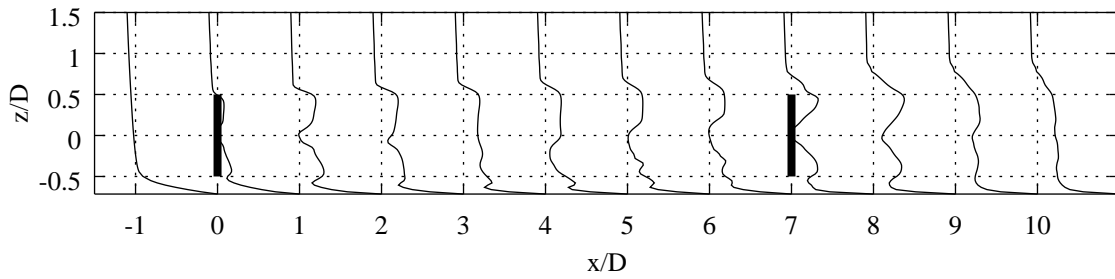


Figure 3.50: Mean axial velocity deficit ($1 - U_x/U_{ref}$) profiles along z (vertical) axis at different x stations (ABL flow case with WT1 yawed).

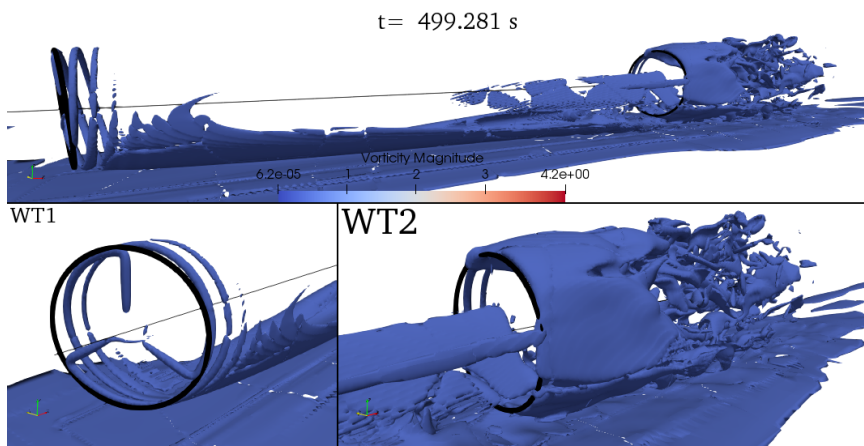


Figure 3.51: Vorticity $\zeta = 0.38$ iso-surfaces (ABL inflow case with WT1 yawed)

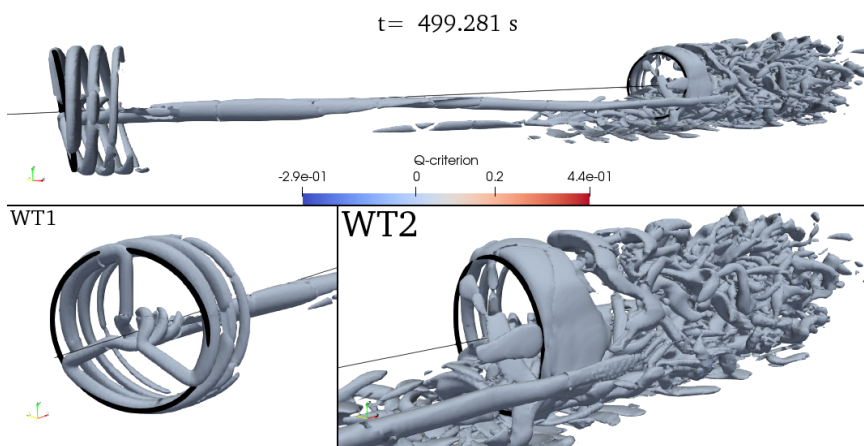


Figure 3.52: Q -criterion $Q = 0.005$ iso-surfaces (ABL inflow case with WT1 yawed)

3.2.4 Assesment of ABL and Yaw Effects

Power production is the ultimate indicator of wind turbine performance. Despite the minimal oscillations, power histogram of WT1 remains constant throughout the whole simulation for all cases, due to the lack of any disturbance. It takes about 100s of simulation time for WT1 to reach its terminal power production value (Fig. 3.53). Behavior of WT2 varies from case to case, but overall, it has dramatically larger oscillations when compared to WT1, due to irregular and turbulent incoming flow.

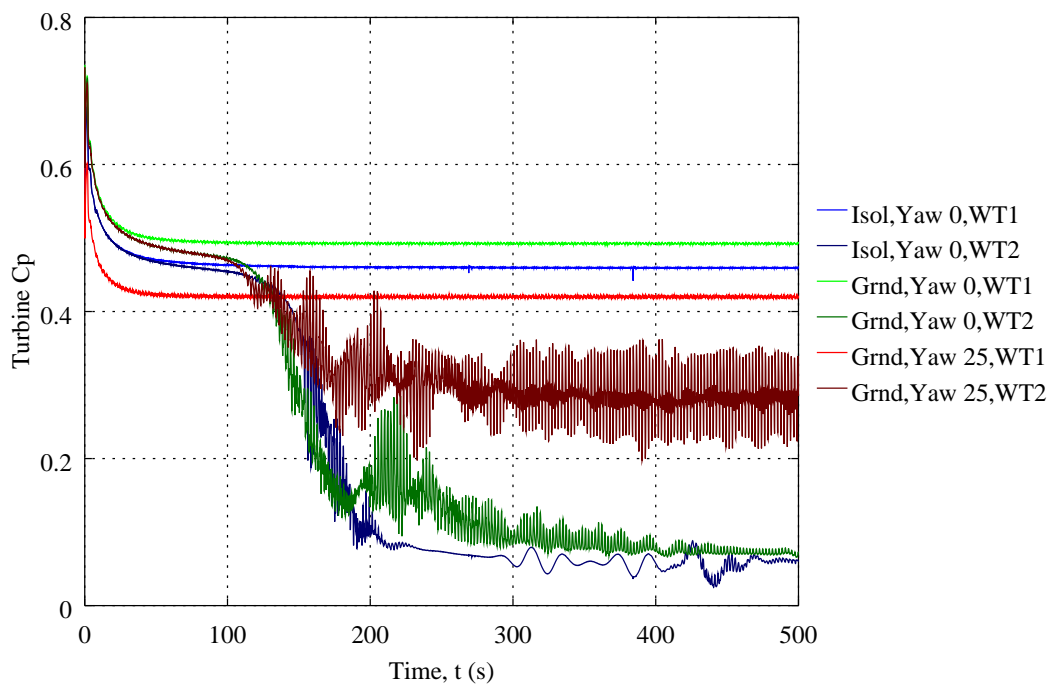


Figure 3.53: C_P convergence in different dual turbine conditions.

One interesting observation is the $\approx 7\%$ higher WT1 power production obtained in ABL flow case compared to the uniform flow case. This is due to the analytical modeling of ABL, which yields larger axial velocity magnitude in the upper-half of the rotor (Fig. 3.44). Although velocity magnitude is smaller in the lower half, it obviously has a lesser effect compared to the power gained in the upper half.

The power loss at WT2 in non-yawed simulations is 86%, which is very high than real-life expectancies (Table 3.1). A similar result has been obtained by Schmitz and Jha [88]. This drastic loss is attributed to the lack of atmospheric turbulence

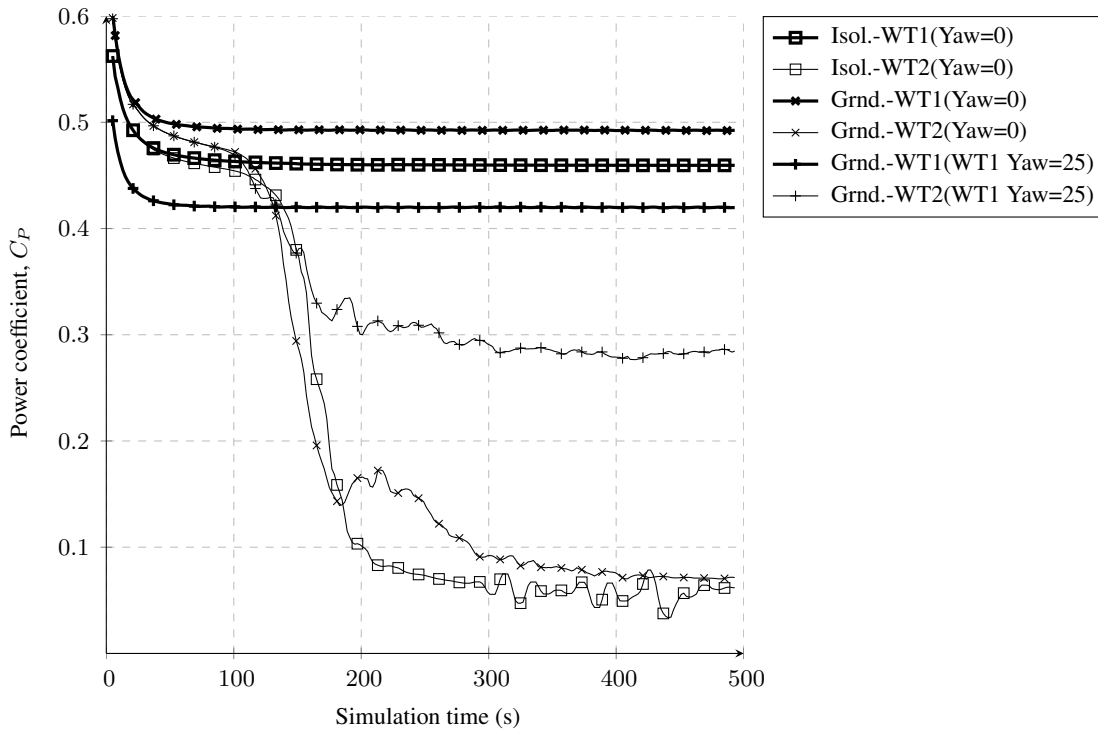


Figure 3.54: C_P convergence history of dual wind turbine simulations (smoothened out via moving average).

preventing wake recovery and velocity deficit to diffuse out. Also, WT2 is operated at the same tip speed ratio as the upstream turbine, which should not be the case in practice. Wind turbines has speed controllers which adjust angular velocity and torque based on field measurements, that is not modeled in this study.

When the upstream turbine is yawed by 25° , its power production suffers a 15% loss. However, a dramatic improvement on downstream turbine is achieved by 200%. This practice reduces the loss on WT2 from 86% to 32%, which corresponds to a 25% percent gain in overall power production. In another study with similar conditions, total power gain was predicted as 5% by Fleming et al. [90]. Again, absence of atmospheric turbulence is the main reason of the disagreement here, causing and over-estimated power loss in non-yawed flow case.

When compared to uniform flow case, power of WT1 is increased by 7% in ABL case as mentioned before, and also WT2 produces 14% more power. Overall power production increases by 8% when ABL is introduced, which is solely due to the

Table 3.1: Individual and total power output of various dual rotor configurations.

Case	$C_{P,WT1}$	$C_{P,WT2}$	WT2 Loss	$C_{P,Avg}$
Isolated	0.459	0.062	86%	0.261
ABL	0.492	0.071	86%	0.282
ABL (WT1 yawed)	0.420	0.285	32%	0.353

analytical modeling of sheared flow.

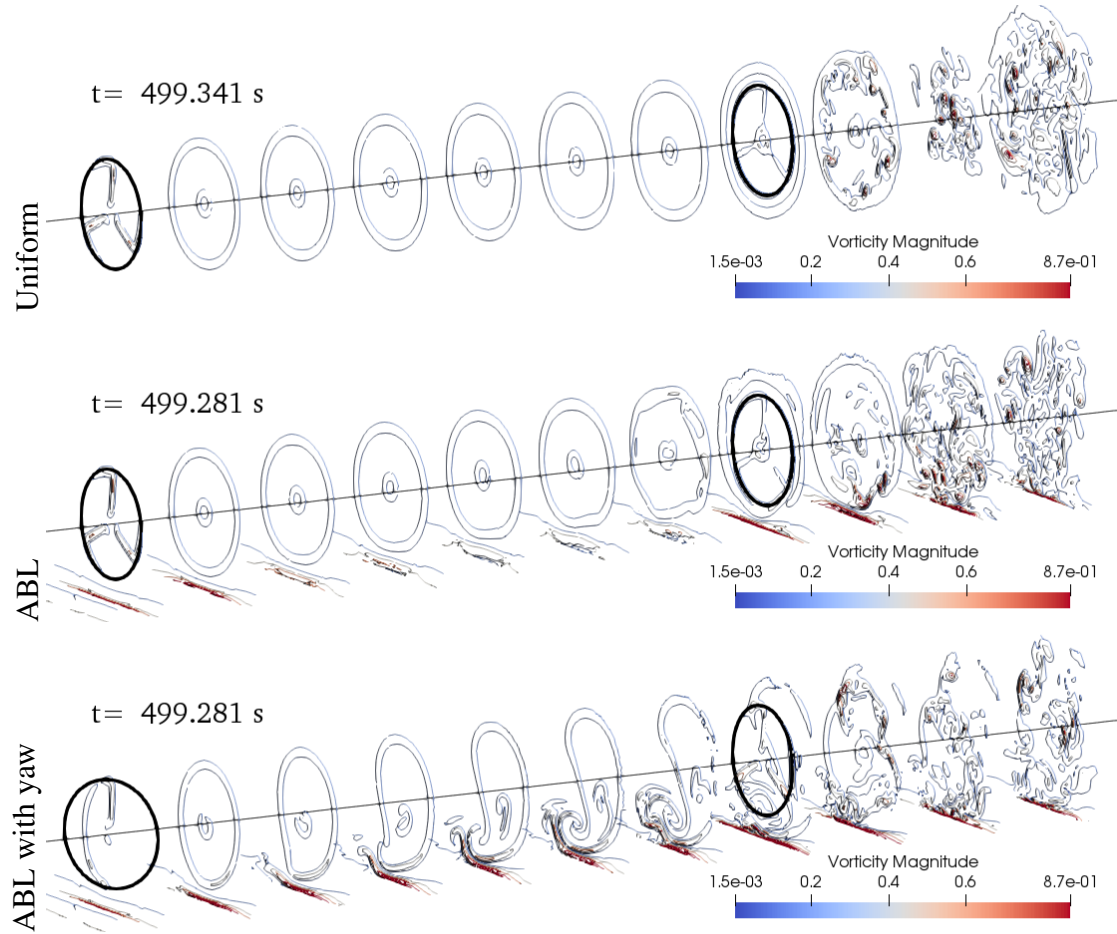


Figure 3.55: Vorticity contours at various x -stations in different dual turbine cases.

x -plane slices of vorticity contours show the advection process of vortical structures. The ground does not have any significant effect on the wake structure at uniform flow case, but quite evidently the yaw aggravates the wake breakdown starting from $x = 4D$ distance (Fig. 3.55). Introduction of the ABL does some contribution to the breakdown of vortices, especially in the ground vicinity, due to turbulence generated from the highly sheared boundary layer flow. With the upstream turbine yawed, center

of the wake is shifted towards the yaw direction.

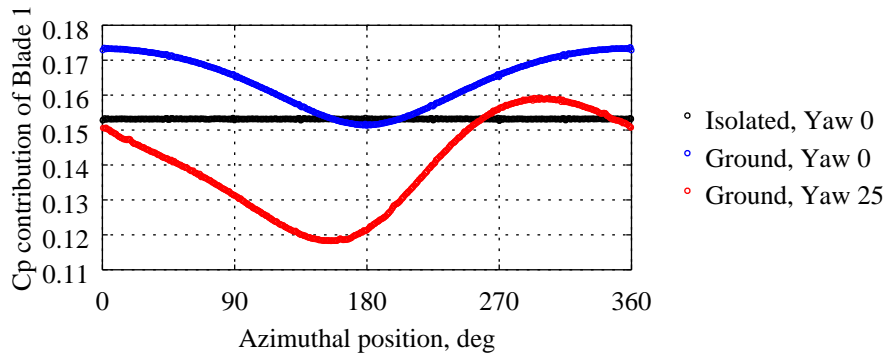


Figure 3.56: Cyclic histogram of Blade 1's power contribution to WT1 (data is collected over last 5 revolutions).

To observe a blade's contribution to the total power production as it rotates, cyclic C_P histograms for a single blade i.e. blade 1 are plotted for upstream and downstream turbines (Figures 3.56 and 3.57). Azimuthal positions at which the maximum and minimum power are generated varies significantly from case to case. As expected, it remains constant for WT1 in the uniform flow case. A slight variation is evident for WT2, since the angular position of blades for both rotors remain the same throughout the simulation. That means, after the periodically-steady state is reached, vortices shed from the upstream turbine blades are always in line with WT2 counterparts.

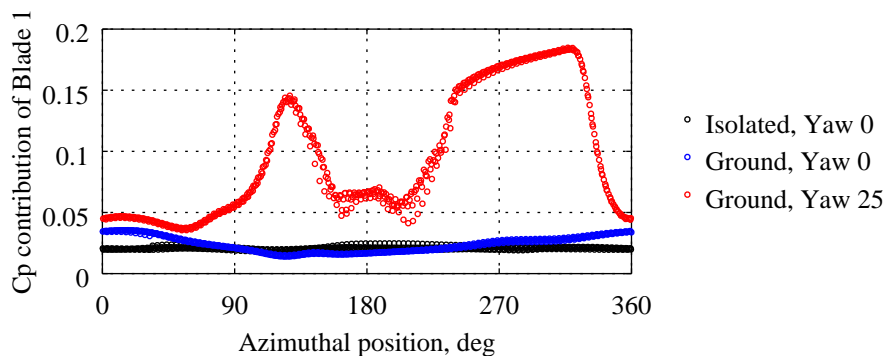


Figure 3.57: Cyclic histogram of Blade 1's power contribution to WT2 (data is collected over last 5 revolutions).

In ABL flow for WT1, power production is maximum at 0° azimuthal position, even outperforming uniform flow case due to higher axial velocity; however it drops slightly below when the blade tip is at its closest position to the ground. Maximum

and minimum power points are similar in WT2, except the minimum power point is slightly shifted towards 90° .

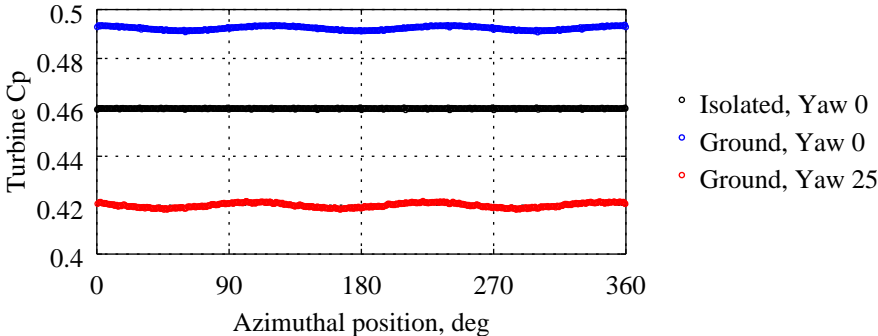


Figure 3.58: Cyclic histogram of WT1's power production (data is collected over last 5 revolutions).

Contribution of blade 1 to the power production of WT1 is reduced at all angular positions when it is yawed. The largest difference is observable at the minimum power point, which is also slightly skewed from 180° degrees. The gap reduces as blade 1 approaches its maximum point, which is approximately 300° for the yawed rotor case. Blade 1 of WT2 exhibits a cyclic but uncharacteristic trend as compared to the non-yawed case. It has a significantly higher contribution overall, with a sharp peak at 110° . An extended plateau is observed on the lateral half of the rotor which does not experience the wake ($180^\circ - 360^\circ$).

The aggregate contribution of all blades for WT1 for all study cases is given in Fig. 3.59. Apparently, the pattern is smoothed but there is an average variation. The periodicity is much more pronounced for WT2 in yawed upstream rotor case, where C_P varies between 0.22 and 0.35 3 times revolution.

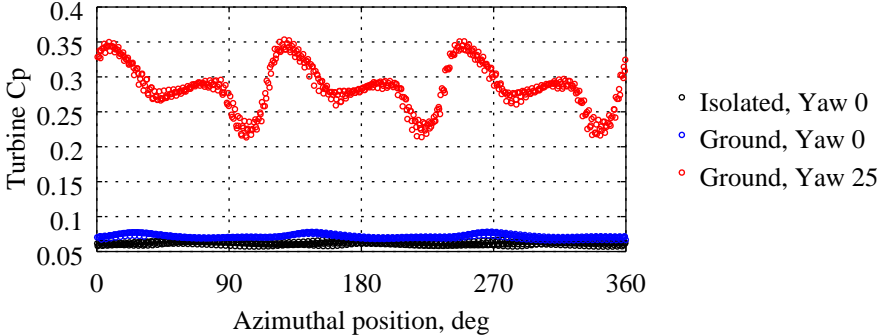


Figure 3.59: Cyclic histogram of WT2's power production (data is collected over last 5 revolutions).

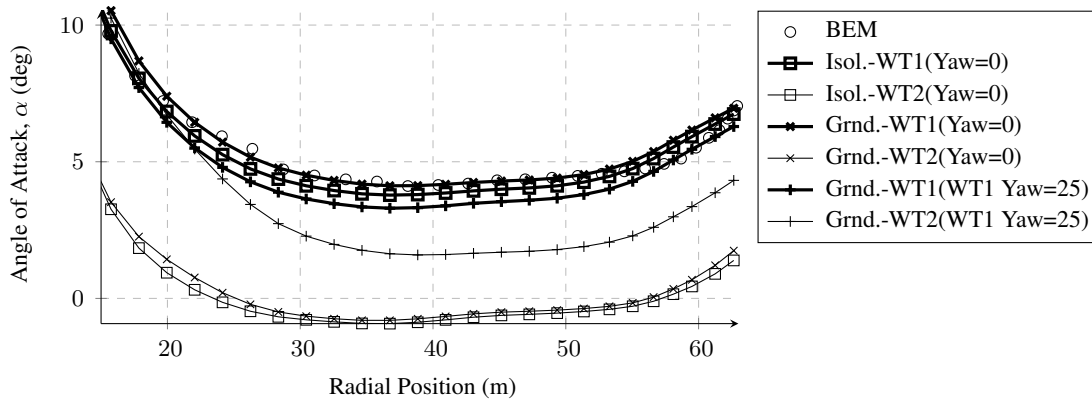


Figure 3.60: *Computed α distribution for different dual turbine cases (averaged over last 5 revolutions).*

Figures 3.60 and 3.61 compares angle of attack and tangential force distributions of blade 1 of each wind turbine in all flow scenarios, respectively. As expected, WT1 shows the best agreement with BEM results for all cases, since incoming flow is laminar. Computed α shifts throughout the span significantly for WT2, especially for non-yawed cases where wake generated by WT1 is directly experienced by WT2 blades, even dropping below 0° in the mid-span region. Since the wake affect only one half of the WT2 rotor, α distribution is closer to WT1 case in the root region, but varies in mid-to-tip regions where most of the tangential force is generated. A similar trend is observed for the tangential force distributions, because it can be considered a function of angle of attack.

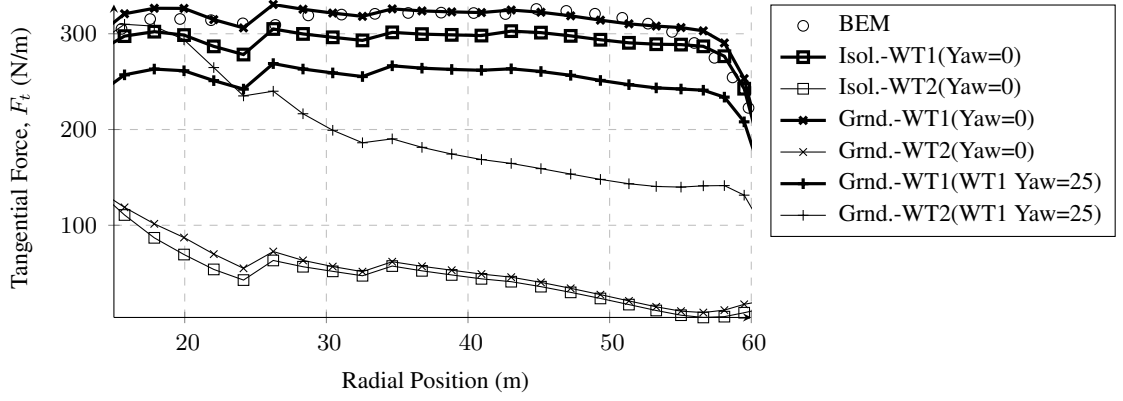


Figure 3.61: Computed F_t distribution for different dual turbine cases (averaged over last 5 revolutions).

3.3 Computational Cost and Parallelization

For all simulations, grid is decomposed by `decomposePar` module of `OpenFOAM` using `SCOTCH` [91] method. The method employs an unstructured decomposition approach which aims to minimize the number of processor boundaries and load per processor. It performs much better than hierarchical methods in domains where cells are significantly denser in certain zones. Hence, it is possible to assign more processors to the inner refinement region (Fig. 3.62) and obtain a more evenly distributed workload among each core; i.e. blue and green blocks are within the inner rotor region and others are located in the immediately coarsened wake region.

Solution time is primarily determined by three factors: time step size Δ_t , rotor refinement level Δ_g/R and how long the rotor refinement level is extended. Table 3.2 shows the clock time it takes to simulate an isolated rotor with different CFL_{tip} values. Despite the consistent decrease in clock time, there is no clear relation between the rate of speed-up and time step size. This inconsistency is attributed to some frequent interruptions caused by external factors during the simulations (i.e. power outages).

Table 3.2: Solution time of simulations with different CFL_{tip} values.

CFL_{tip}	0.45	0.90	1.80	2.70	3.60	7.20
Clock time (h)	35.17	15.47	10.53	9.06	3.17	2.15

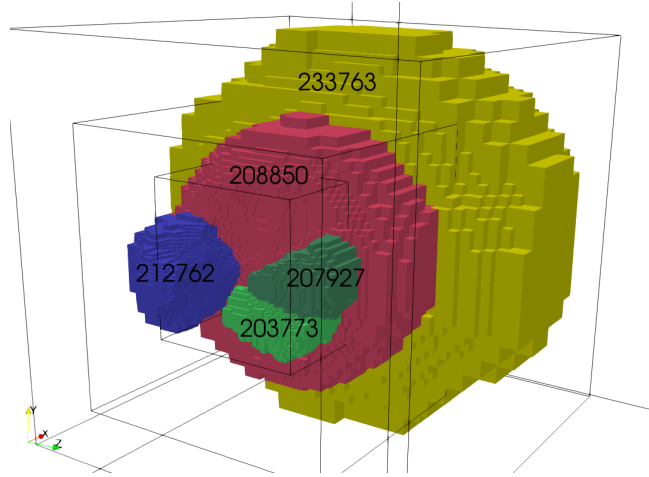


Figure 3.62: 5 of the cell blocks assigned to their respective processor cores in the decomposed domain. Numbers denote the cell count per block.

Effect of rotor region refinement level and its size can be seen on Table 3.3. Rotor region refinement is extended 1D downstream for single WT cases and all the way down to the second wind turbine and 3.5D more for dual WT cases. Grid size increases exponentially with Δ_g/R and this is dramatically felt in the solution time. Grid size and solution time remarkably increases by 5.7 and 3.9 times respectively when Δ_g/R is refined from 1/32 to 1/64 in a single rotor case, despite doubling the number of processors. Similarly, doubling the number of cells per rotor radius in a dual rotor simulation causes the solution time to increase more than 6 times. It should be noted that for the single rotor case; $t_{final} = 100s$, $U_{ref} = 11.4m/s$, $TSR = 7$ and $\Delta_t = 0.0111s$. In dual rotor simulations, $t_{final} = 500s$, $U_{ref} = 8m/s$, $TSR = 7.3$ and $\Delta_t = 0.0607s$.

Table 3.3: Solution time of simulations with different grid sizes.

Case	Δ_g/R	Grid size	N_{cores}	Clock time
Single WT	1/16	343K	32	2.0h
Single WT	1/32	821K	32	13.4h
Single WT	1/64	4.7M	64	52.4h
Dual WT	1/16	992K	64	23.8h
Dual WT	1/32	4.7M	64	5d 4h

Parallel speed-up trends of different grid sizes (single and dual rotor cases) are extrapolated from 5.3s of simulation time and plotted for the same grid resolution

at the rotor region ($\Delta_g/R = 1/32$) in Fig. 3.63. With less number of grid points, speed-up increases up to $N_{cores} = 64$ and drops sharply after $N_{cores} = 128$. Using more cores becomes feasible only if the grid size increases; speed-up per number of cores is higher in dual rotor simulations within $N_{cores} = 32 - 64$ range. It is seen that the current cluster is most efficient within the 32-128 cores range, while the optimum number of cores depends on the size of the problem.

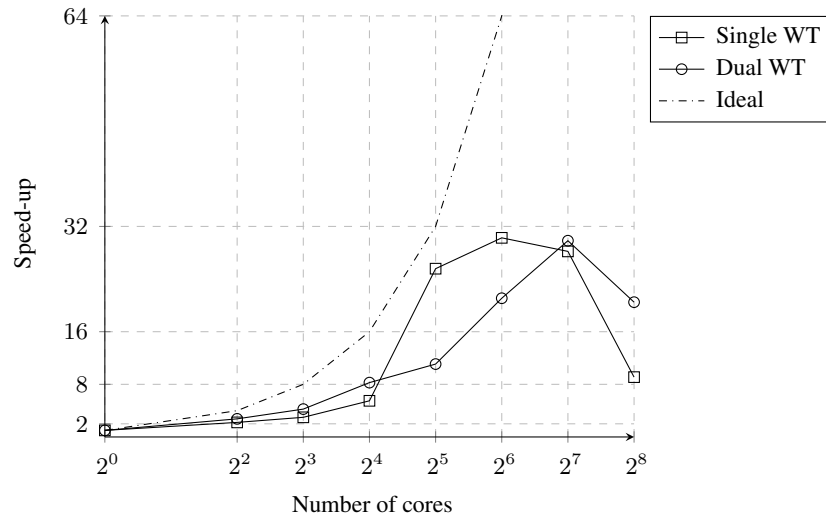


Figure 3.63: *Parallelization speed-up vs. number of cores for single and dual wind turbine simulations. (Single WT: 821K cells, Dual WT: 4.7M cells)*

Solutions are performed on the parallel computer system which is housed in High Performance Computing Laboratory of METU Center for Wind Energy (RÜZGEM). The cluster features 8 nodes with 4 AMD® Opteron™ 6276 CPUs (16 cores, clocked at 2.30 GHz) per node, totaling up to 512 cores.

CHAPTER 4

CONCLUSIONS

In this study, single and multiple NREL 5MW wind turbines were modeled using Actuator Line Model and unsteady Navier-Stokes equations were solved to simulate the flow around wind turbines. A SIMPLE/PISO algorithm based OpenFOAM solver `pimpleFoam` was used for flow solution, turbulence was modeled with LES, 2D airfoil data was obtained by integral boundary layer solver XFOIL and results are validated against BEM solutions.

Critical simulation parameters used in ALM are investigated. Velocity sampling and force projection methods arose as the main complexities in ALM. Force projection width and grid size affect the performance of ALM in a coupled way. Choosing a cell size based (or constant throughout the blade span) ϵ (the projection width control parameter) yielded better results than chord based approach. Although the model was very sensitive to grid size, it could be handled by choosing an appropriate projection width. Nonetheless, turbulent wake structures were captured better as the grid was refined further. This posed a trade-off problem in terms of computational cost, especially for large wind farm simulations. No convergent trend was observed in terms of ϵ ; larger values caused over-estimation of blade loadings and small values caused instabilities. Similarly, generally accepted $CFL_{tip} < 1$ rule could not be justified and time step size exhibited a non-convergent trend. Hence, an optimum value had to be chosen for reasonable results. Rotational speed also had an impact on loading predictions, simulation time needed for convergence has increased with TSR. Overall, ALM has yielded close results to BEM solutions in the isolated wind turbine case, given the proper simulation parameters.

Dual in-line rotor simulations were performed to assess the model's wake prediction

capabilities. It was found that atmospheric turbulence is of utmost importance in obtaining accurate wake losses, since its absence has prevented wake recovery and yielded extreme power losses in downstream turbines. ALM has performed adequately in wake re-direction scenarios.

Factors which affect computational cost the most are CFL_{tip} condition, TSR (rotational speed) and grid resolution (number of cells per rotor radius, Δ_g/R). To simulate two turbines, distance between them had to be kept at the same refinement level with the rotor regions to be able to capture wake interactions accurately. This requirement has a significant impact on grid size and computation time accordingly (5 days on 64 cores in this study). It should also be considered that the free stream direction did not change in this study. In a case where the wind direction changes with time, nearly the whole domain should be refined to capture any possible wake direction. Considering this fact, a full scale wind farm simulation will definitely need more cores and a linear extrapolation would not be adequate to estimate the computation time.

Actuator Line Model is one of the most promising models to be used in large scale wind farm simulations, due to its computational advantage and reasonable trade-off in accuracy. Biggest disadvantage of the model comes from its unsteady nature and limitations due to time step size, also its high sensitivity to certain simulation parameters. The model is in need of validation against other methods (i.e. experimental or fully-resolved CFD) on a single isolated wind turbine for fine simulation parameter adjustment to get acceptable results in a full scale wind farm simulation.

As a future work, atmospheric turbulence will be introduced via precursor solutions or synthetic turbulence implementation. Despite its disadvantages, Actuator Disk Model still offers better computational economy with the possibility of steady simulations. Hence, performance of ADM will be assessed and compared against ALM. In their recent study, Leblebici and Tuncer [92] have successfully coupled the WRF data with OpenFOAM solvers to obtain flow solutions over a wind field. The present model is planned to be coupled with WRF in a similar way for wind power predictions in a wind farm with accurate wake computations.

REFERENCES

- [1] N. Simisiroglou, S. Philippe Breton, and S. Ivanell, “Validation of the actuator disc approach using small scale model wind turbines,” *Wind Energy Science Discussions*, pp. 1–19, 04 2017.
- [2] L. Martínez Tossas, S. Leonardi, M. Churchfield, and P. Moriarty, “A comparison of actuator disk and actuator line wind turbine models and best practices for their use,” 01 2012.
- [3] N. Troldborg, J. N. Sørensen, and R. Mikkelsen, “Actuator line simulation of wake of wind turbine operating in turbulent inflow,” *Journal of Physics: Conference Series*, vol. 75, p. 012063, jul 2007.
- [4] M. Hansen, *Aerodynamics of Wind Turbines*. 01 2008.
- [5] T. Burton, D. Sharpe, N. Jenkins, and E. Bossanyi, *The Wind Energy Handbook*, vol. 1. 01 2001.
- [6] E. Branlard, *The Blade Element Momentum (BEM) Method*, pp. 181–211. Cham: Springer International Publishing, 2017.
- [7] P. Moriarty and A. Hansen, “Aerodyn theory manual,” Tech. Rep. NREL/TP-500-36881, National Renewable Energy Laboratory, 2005.
- [8] F. Bianchi, H. De Battista, and R. J. Mantz, *Wind Turbine Control Systems: Principles, Modelling and Gain Scheduling Design*. 01 2007.
- [9] P. Benard, A. Viré, V. Moureau, G. Lartigue, L. Beaudet, P. Deglaire, and L. Bricteux, “Large-eddy simulation of wind turbines wakes including geometrical effects,” *Computers and Fluids*, vol. 173, pp. 133 – 139, 2018.
- [10] L. A. Martínez-Tossas, M. J. Churchfield, and C. Meneveau, “Optimal smoothing length scale for actuator line models of wind turbine blades based on gaussian body force distribution,” *Wind Energy*, vol. 20, no. 6, pp. 1083–1096, 2017.

- [11] B. Dose, H. Rahimi, I. Herráez, B. Stoevesandt, and J. Peinke, “Fluid-structure coupled computations of the nrel 5 mw wind turbine by means of cfd,” *Renewable Energy*, vol. 129, 05 2018.
- [12] S. Burmester, S. Gueydon, and M. Make, “Determination of scaled wind turbine rotor characteristics from three dimensional rans calculations,” *Journal of Physics: Conference Series*, vol. 753, 09 2016.
- [13] *EIA projects 48% increase in world energy consumption by 2040*. <https://www.eia.gov/todayinenergy/detail.php?id=26212>, Last accessed 14 September 2019.
- [14] *Renewable Energy - Thematic Research*. <https://www.globaldata.com/store/report/gdpe-tr-s007--renewable-energy-thematic-research/>, Last accessed 14 September 2019.
- [15] *Onshore Wind Power Now as Affordable as Any Other Source, Solar to Halve by 2020*. <http://www.irena.org/newsroom/pressreleases/2018/Jan/Onshore-Wind-Power-Now-as-Affordable-as-Any-Other-Source>, Last accessed 14 September 2019.
- [16] *2015 Cost of Wind Energy Review*. <https://www.nrel.gov/docs/fy17osti/66861.pdf>, Last accessed 14 September 2019.
- [17] S. Frandsen and M. Thøgersen, “Integrated fatigue loading for wind turbines in wind farms by combining ambient turbulence and wakes,” *Wind Engineering*, vol. 23, pp. 327–339, 1999.
- [18] M. Schramm, H. Rahimi, B. Stoevesandt, and K. Tangager, “The influence of eroded blades on wind turbine performance using numerical simulations,” *Energies*, vol. 10, p. 1420, Sep 2017.
- [19] J. G. Holierhoek, “5 - aeroelastic design of wind turbine blades,” in *Advances in Wind Turbine Blade Design and Materials* (P. Brøndsted and R. P. Nijssen, eds.), Woodhead Publishing Series in Energy, pp. 151 – 173, Woodhead Publishing, 2013.

- [20] R. Barthelmie, S. T Frandsen, O. Rathmann, K. Hansen, E. Politis, J. Prospathopoulos, J. G Schepers, K. Rados, D. Cabezon, W. Schlez, A. Neubert, and M. Heath, “Flow and wakes in large wind farms: Final report for upwind wp8,” 01 2011.
- [21] S. K. Wessel, “Power optimization of wind farms by curtailment of upwind turbines,” Master’s thesis, Technical University of Denmark, Department of Applied Mathematics and Computer Science, Richard Petersens Plads, Building 324, DK-2800 Kgs. Lyngby, Denmark, compute@compute.dtu.dk, 2015.
- [22] P. M. O. Gebraad, F. W. Teeuwisse, J. W. van Wingerden, P. A. Fleming, S. D. Ruben, J. R. Marden, and L. Y. Pao, “Wind plant power optimization through yaw control using a parametric model for wake effects—a cfd simulation study,” *Wind Energy*, vol. 19, no. 1, pp. 95–114, 2016.
- [23] R. Storm, “Wake control using rotor tilting: Optimizing wind farm energy production through vertical wake deflection,” Master’s thesis, Delft University of Technology, 2018.
- [24] L. Vermeer, J. Sørensen, and A. Crespo, “Wind turbine wake aerodynamics,” *Progress in Aerospace Sciences*, vol. 39, no. 6, pp. 467 – 510, 2003.
- [25] J. Ainslie, “Calculating the flowfield in the wake of wind turbines,” *Journal of Wind Engineering and Industrial Aerodynamics*, vol. 27, no. 1, pp. 213 – 224, 1988.
- [26] J. Cheng, W. Lubitz, and B. White, “Wind-tunnel prediction of wind power production in complex terrain,” *Collection of ASME Wind Energy Symposium Technical Papers AIAA Aerospace Sciences Meeting and Exhibit*, 01 2004.
- [27] M. Bastankhah and F. Porté-Agel, “A new miniature wind turbine for wind tunnel experiments. part ii: Wake structure and flow dynamics,” *Energies*, vol. 10, p. 923, 07 2017.
- [28] N. Jensen, *A note on wind generator interaction*. Risø National Laboratory, 1983.

- [29] I. Katic, J. Højstrup, and N. Jensen, “A simple model for cluster efficiency,” in *EWEC’86. Proceedings. Vol. 1* (W. Palz and E. Sesto, eds.), pp. 407–410, A. Raguzzi, 1987. Jensen 2.
- [30] T. Ishihara and Y. Fujino, “Development of a new wake model based on a wind tunnel experiment,” 01 2004.
- [31] A. Mittal, L. Taylor, K. Sreenivas, and A. Arabshahi, “Investigation of two analytical wake models using data from wind farms,” vol. 6, 11 2011.
- [32] S. Frandsen, R. Barthelmie, S. Pryor, O. Rathmann, S. Larsen, J. Højstrup, and M. Thøgersen, “Analytical modelling of wind speed deficit in large offshore wind farms,” *Wind Energy*, vol. 9, no. 1, pp. 39–53, 2006.
- [33] N. Charhouni, M. Sallaou, and A. Arbaoui, “Qualification of three analytical wake models,” *Journal of Mechanics Engineering and Automation*, vol. 6, 04 2016.
- [34] S. Voutsinas, “On the analysis of wake effects in wind parks,” *WIND ENGINEERING*, vol. 14, pp. 204–219, 01 1990.
- [35] P. Lissaman, “Wind turbine airfoils and rotor wakes,” *Wind Turbine Technology, ASME Press, New York*, pp. 283–323, 1994.
- [36] P. A. Taylor, “On wake decay and row spacing for WECS farms,” in *3rd International Symposium on Wind Energy Systems* (W. T. Downey, ed.), pp. 451–468, 1980.
- [37] A. Crespo, F. Manuel, D. Moreno, E. Fraga, and J. Hernández, “Numerical analysis of wind turbine wakes,” 1985.
- [38] P. M. Sforza, P. Sheerin, and M. Smorto, “Three-dimensional wakes of simulated wind turbines,” *Aiaa Journal - AIAA J*, vol. 19, pp. 1101–1107, 09 1981.
- [39] R. E. Froude, “On the part played in propulsion by difference in pressure,” *Transactions of the Institution of Naval Architects*, pp. 390–423, 1889.
- [40] A. Betz, “Das maximum der theoretisch möglichen ausnützung des windes durch windmotoren,” *Zeitschrift für das gesamte Turbinenwesen*, 1920.

- [41] H. Glauert, *Airplane Propellers*, pp. 169–360. Berlin, Heidelberg: Springer Berlin Heidelberg, 1935.
- [42] O. Yemenici, N. Sezer Uzol, and O. Uzol, “Investigation of rotor-rotor interactions for two helicopters in forward flight using free-vortex wake methodology,” 06 2010.
- [43] R. Franco, Q. Valverde, F. Canziani, and R. Yupa Villanueva, “Verification of the aerodynamic design of the wind turbine propeller of 3kw trough cfd software,” 02 2019.
- [44] N. Sezer Uzol and L. Long, “3-d time-accurate cfd simulations of wind turbine rotor flow fields,” *American Institute of Aeronautics and Astronautics*, vol. 394, 01 2006.
- [45] Y. Song and J. Perot, “Cfd simulation of the nrel phase vi rotor,” *Wind Engineering*, vol. 39, 04 2014.
- [46] L. Lavaroni, S. Watson, M. Cook, and M. R Dubal, “A comparison of actuator disc and bem models in cfd simulations for the prediction of offshore wake losses,” *Journal of Physics: Conference Series*, vol. 524, p. 012148, 06 2014.
- [47] A. Jimenez, A. Crespo, E. Migoya, and J. Garcia, “Advances in large-eddy simulation of a wind turbine wake,” *Journal of Physics: Conference Series*, vol. 75, p. 012041, jul 2007.
- [48] R. Mikkelsen, J. Sørensen, and W. Shen, “Modelling and analysis of the flow field around a coned rotor,” *Wind Energy*, vol. Vol. 4, pp. pp. 1–15, 2001.
- [49] F. Porté-Agel, H. Lu, and Y.-T. Wu, “A large-eddy simulation framework for wind energy applications,” 2010.
- [50] J. Norkaer Sorensen and W. Z. Shen, “Numerical modeling of wind turbine wakes,” *Journal of Fluids Engineering*, vol. 124, p. 393, 01 2002.
- [51] P.-A. Krogstad and P. Egil Eriksen, ““blind test” calculations of the performance and wake development for a model wind turbine,” *Renewable Energy*, vol. 50, p. 325–333, 02 2013.

- [52] L. SaeTRAN, P.-A. Krogstad, and M. Adaramola, "Performance and wake development behind two in-line and offset model wind turbines – "blind test" experiments and calculations," *Journal of Physics Conference Series*, vol. 524, p. 12, 06 2014.
- [53] M. Tabib, A. Rasheed, and T. Kvamsdal, "LES and RANS simulation of onshore bessaker wind farm: analysing terrain and wake effects on wind farm performance," *Journal of Physics: Conference Series*, vol. 625, p. 012032, jun 2015.
- [54] M. Tzimas and J. Prospathopoulos, "Wind turbine rotor simulation using the actuator disk and actuator line methods," *Journal of Physics: Conference Series*, vol. 753, p. 032056, sep 2016.
- [55] P. Bachant, A. Goude, and M. Wosnik, "Actuator line modeling of vertical-axis turbines," 04 2018.
- [56] P. Jha, M. J. Churchfield, P. Moriarty, and S. Schmitz, "Guidelines for volume force distributions within actuator line modeling of wind turbines on large-eddy simulation-type grids," *Journal of Solar Energy Engineering*, vol. 136, p. 031003, 08 2014.
- [57] Z. Yu, X. Zheng, and Q. Ma, "Study on actuator line modeling of two nrel 5-mw wind turbine wakes," *Applied Sciences*, vol. 8, p. 434, 03 2018.
- [58] N. Troldborg, *Actuator Line Modeling of Wind Turbine Wakes*. PhD thesis, Technical University of Denmark, 1 2009.
- [59] M. Draper and G. Usera, "Evaluation of the actuator line model with coarse resolutions," *Journal of Physics: Conference Series*, vol. 625, 06 2015.
- [60] L. A. Martínez-Tossas and C. Meneveau, "Filtered lifting line theory and application to the actuator line model," *Journal of Fluid Mechanics*, vol. 863, p. 269–292, 2019.
- [61] R. Merabet and E. Laurendeau, "Parametric study on the velocity sampling techniques for the actuator line method in 2d," in *AIAA Scitech 2019 Forum*.

- [62] L. Martínez Tossas, M. J. Churchfield, and S. Leonardi, “Large eddy simulations of the flow past wind turbines: actuator line and disk modeling: Les of the flow past wind turbines: actuator line and disk modeling,” *Wind Energy*, vol. 18, 04 2014.
- [63] P. Fleming, P. Gebraad, S. Lee, J. W. Wingerden, K. Johnson, M. Churchfield, J. Michalakes, P. Spalart, and P. Moriarty, “Evaluating techniques for redirecting turbine wake using sowfa,” *Renewable Energy*, vol. 70, pp. 211–218, 10 2014.
- [64] L. A. Martínez-Tossas, M. J. Churchfield, and C. Meneveau, “Large eddy simulation of wind turbine wakes: detailed comparisons of two codes focusing on effects of numerics and subgrid modeling,” *Journal of Physics: Conference Series*, vol. 625, p. 012024, jun 2015.
- [65] M. J. Churchfield, S. J. Schreck, L. A. Martinez, C. Meneveau, and P. R. Spalart, *An Advanced Actuator Line Method for Wind Energy Applications and Beyond*. 2017.
- [66] J. Nathan, C. Masson, and L. Dufresne, “Analysis of the swepted actuator line method,” vol. 5, 05 2014.
- [67] A. Matiz and O. Lopez Mejia, “Full downwind turbine simulations using actuator line method,” *Modelling and Simulation in Engineering*, vol. 2018, pp. 1–10, 05 2018.
- [68] R. K. Rai, H. Gopalan, J. Sitaraman, J. D. Mirocha, and W. Miller, “A code-independent generalized actuator line model for wind farm aerodynamics over simple and complex terrain,” *Environmental Modelling and Software*, vol. 94, pp. 172–185, 08 2017.
- [69] M. Bühler, P. Weihing, L. Klein, T. Lutz, and E. Krämer, “Actuator line method simulations for the analysis of wind turbine wakes acting on helicopters,” *Journal of Physics: Conference Series*, vol. 1037, p. 062004, 06 2018.
- [70] D. D. Apsley, T. Stallard, and P. Stansby, “Actuator-line cfd modelling of tidal-stream turbines in arrays,” *Journal of Ocean Engineering and Marine Energy*, 10 2018.

- [71] J. N Sørensen, R. Mikkelsen, D. S Henningson, S. Ivanell, S. Sarmast, and S. Andersen, “Simulation of wind turbine wakes using the actuator line technique,” *Philosophical transactions. Series A, Mathematical, physical, and engineering sciences*, vol. 373, 02 2015.
- [72] A. Wimshurst and R. Willden, “Validation of an actuator line method for tidal turbine rotors,” 06 2016.
- [73] H. G. Weller, G. Tabor, H. Jasak, and C. Fureby, “A tensorial approach to computational continuum mechanics using object-oriented techniques,” *COMPUTERS IN PHYSICS, VOL. 12, NO. 6*, NOV/DEC 1998.
- [74] P. Bachant, A. Goude, M. Wosnik, and D. Araya, *turbinesFoam: v0.1.0, Actuator line modeling extension library for OpenFOAM*. DOI: 10.5281/zenodo.1482561, 2016. <https://zenodo.org/record/1482561>, Last accessed 14 September 2019.
- [75] M. Drela, “XFOIL: An analysis and design system for low reynolds number airfoils,” in *Lecture Notes in Engineering*, pp. 1–12, Springer Berlin Heidelberg, 1989.
- [76] D. Marten, J. Wendler, G. Pechlivanoglou, C. N. Nayeri, and C. O. Paschereit, “Qblade an open source tool for design and simulation of horizontal and vertical axis wind turbines,” *IJETAE 3 special issue pp. 264–269 2013*, 2013.
- [77] J. Jonkman, S. Butterfield, W. Musial, and G. Scott, “Definition of a 5-mw reference wind turbine for offshore system development,” Tech. Rep. NREL/TP-500-38060, National Renewable Energy Laboratory, 2009.
- [78] L. Prandtl and A. Betz, pp. 88–92. Göttingen: Goettinger Nachrichten, 1927.
- [79] H. Glauert, *The Elements of Aerofoil and Airscrew Theory*. Cambridge Science Classics, Cambridge University Press, 1926.
- [80] R. E. Wilson and P. B. S. Lissaman, “Applied aerodynamics of wind power machine,” *NASA STI/Recon Technical Report N*, pp. 22669–, 07 1974.
- [81] O. de Vries, “Fluid dynamic aspects of wind energy conversion,” *AGARD-AG-243*, p. 148, 07 1979.

- [82] W. Z. Shen, R. Mikkelsen, J. N. Sørensen, and C. Bak, “Tip loss corrections for wind turbine computations,” *Wind Energy*, vol. 8, no. 4, pp. 457–475, 2005.
- [83] C. Yan and C. L. Archer, “Assessing compressibility effects on the performance of large horizontal-axis wind turbines,” *Applied Energy*, vol. 212, pp. 33 – 45, 2018.
- [84] J. Smagorinsky, “General circulation experiments with the primitive equations,” *Mon. Weather Rev.*, vol. 91, 01 1963.
- [85] I. E. Barton, “Comparison of simple and piso type algorithms for transient flows,” *Int. J. Numer. Meth. Fluids*, 26: 459-483, 1998.
- [86] W. Z. Shen, M. Hansen, and J. Norkaer Sorensen, “Determination of angle of attack (aoa) for rotating blades,” *Wind energy, proceedings of the euromech colloquium*, 01 2007.
- [87] K. Sreenivas, A. Mittal, L. Taylor, and L. Hereth, “Improvements to the actuator line modeling for wind turbines,” 01 2015.
- [88] S. Schmitz and P. Jha, “Modeling the wakes of wind turbines and rotorcraft using the actuator-line method in an openfoam -les solver,” 05 2013.
- [89] D. Hargreaves and N. Wright, “On the use of the k- model in commercial cfd software to model the neutral atmospheric boundary layer,” *Journal of Wind Engineering and Industrial Aerodynamics*, vol. 95, pp. 355–369, 05 2007.
- [90] P. Fleming, J. Annoni, M. Churchfield, L. Martínez Tossas, K. Gruchalla, M. Lawson, and P. Moriarty, “From wake steering to flow control,” *Wind Energy Science Discussions*, pp. 1–17, 11 2017.
- [91] *Software package and libraries for sequential and parallel graph partitioning, static mapping and clustering, sequential mesh and hypergraph partitioning, and sequential and parallel sparse matrix block ordering.* <http://www.labri.fr/perso/pelegrin/scotch/>, Last accessed 14 September 2019.
- [92] E. Leblebici and I. Tuncer, “Wind power estimations using openfoam coupled with wrf,” 09 2015.